IntechOpen

Actuators

Edited by Constantin Volosencu

ACTUATORS

Edited by **Constantin Volosencu**

Actuators
http://dx.doi.org/10.5772/intechopen.71518
Edited by Constantin Volosencu

Contributors

Kazuo Shimizu, Marius Blajan, Yanjie Wang, Takushi Sugino, Alexandru Forrai, Mei Zhang, Ze-Tao Li, Boutaib Dahhou, Michel Cabassud, Rodica Voicu, Przemysław Wiewiórski, Jerzy Kaleta, Rafał Mech, Junichi Danjo, Sonoko Danjo, Hideyuki Sawada, Keiji Uchida, Yu Nakamura

Notice

Statements and opinions expressed in the chapters are these of the individual contributors and not necessarily those of the editors or publisher. No responsibility is accepted for the accuracy of information contained in the published chapters. The publisher assumes no responsibility for any damage or injury to persons or property arising out of the use of any materials, instructions, methods or ideas contained in the book.

First published in London, United Kingdom, 2018 by IntechOpen
eBook (PDF) Published by IntechOpen, 2019
IntechOpen is the global imprint of INTECHOPEN LIMITED, registered in England and Wales, registration number: 11086078, The Shard, 25th floor, 32 London Bridge Street
London, SE19SG – United Kingdom
Printed in Croatia

British Library Cataloguing-in-Publication Data
A catalogue record for this book is available from the British Library

Additional hard and PDF copies can be obtained from orders@intechopen.com

Actuators
Edited by Constantin Volosencu

p. cm.

Print ISBN 978-1-78923-428-2

Online ISBN 978-1-78923-429-9

eBook (PDF) ISBN 978-1-83881-583-7

Meet the editor

Constantin Volosencu is a professor at "Politehnica" University from Timisoara, Department of Automation. He is the author of 10 books and 4 book chapters, editor of 4 books, author of over 150 scientific papers published in journals and conference proceedings, author of 27 patents and manager of research grants. He is a member of editorial boards of international journals, a former plenary speaker, a member in scientific committees and the chair at international conferences. He has researches in the field of control systems, electrical drives, power ultrasounds, fuzzy logic, neural networks, fault detection and diagnosis, sensor networks and distributed parameter systems. He developed electrical equipment for machine tools, spooling machines, high-power ultrasound processes and others, with homologation of 18 prototypes and 12 zero manufacturing series.

Contents

Preface

The book promotes new research results in the field of modern actuators and their applications. In the last years, a huge variety of ideas and results have been published in journals and conferences. Some of them have been developed for industrial production. Smart materials and microtechnologies stay as the base of the new actuators and their applications. The book comprehends new coverage of dielectric barrier discharge plasma actuators, polymeric microgripper based on the cascaded V-shaped electrothermal actuators, ionic polymer actuators, wideband actuators and energy harvesters, electromagnetic actuators, and shape memory alloy actuators.

The authors have published worked examples and case studies as a result from their researches in the field. The readers get new solutions and answers to questions related to the emerging actuation principles, fabrication, modeling, simulation, control, fault detection, implementation, and their applications.

In a brief description, the book has four sections: "Design, Fabrication and Simulation of Actuators," "Modeling, System Identification, and Control of Actuators," "Medical Applications of Actuators," and "Fault Detection of Actuators."

The book presents in seven chapters cases that illustrate the research results in the above domains. The chapters were edited and published following a rigorous selection process, out of more than double the number of publication proposals.

The first section includes the following chapters: a study carried out to investigate experimentally and by numerical simulations a microscale plasma actuator; the design, fabrication, numerical simulations, and experimental investigations of a polymeric microgripper designed using the cascaded V-shaped electrothermal actuators; a review of the development of ionic polymer actuator with introduction of two kinds of typical polymer actuators —ionic polymer-metal composites and bucky gel actuator—with their basic principle; and fabrication process and typical applications and a methodology of designing and testing wideband actuators and energy harvesters, treated as one mechanical resonator, with a discussion on shock harvester, resonant harvester and energy transmission system.

The second section is dedicated to a chapter on modeling, system identification and control of electromagnetic actuators, with main focus on the actuators used in magnetic levitation, in fuel injection systems and in variable valve timing.

The third section presents a study focused on quantifying the decline in tactile sensation associated with diabetic neuropathy, and developed a measurement device that used a thin-shaped memory alloy wire as the actuator.

The fourth section includes a chapter presenting a two-level fault diagnosis and root cause analysis scheme for a class of interconnected invertible dynamic systems, which aims at detecting and identifying actuator fault and the causes.

The editor thanks the authors for their excellent contributions in the field and understanding during the process of editing. Also, the editor thanks all the editorial personnel involved in this book publication. The publishing provided a set of editorial standards, which ensured the quality of the scientific level of relevance of accepted chapters.

Prof. Constantin Volosencu
"Politehnica" University from Timisoara
Romania

Section 1

Design, Fabrication and Simulation

Chapter 1

Dielectric Barrier Discharge Microplasma Actuator for Flow Control

Kazuo Shimizu and Marius Blajan

Additional information is available at the end of the chapter

http://dx.doi.org/10.5772/intechopen.75802

Abstract

Dielectric barrier discharge (DBD) plasma actuators are a technology which could replace conventional actuators due to their simple construction, lack of moving parts, and fast response. This type of actuator modifies the airflow due to electrohydrodynamic (EHD) force. The EHD phenomenon occurs due to the momentum transfer from charged species accelerated by an electric field to neutral molecules by collision. This chapter presents a study carried out to investigate experimentally and by numerical simulations a micro-scale plasma actuator. A microplasma requires a low discharge voltage to generate about 1 kV at atmospheric pressure. A multi-electrode microplasma actuator was used which allowed the electrodes to be energized at different potentials or waveforms, thus changing the direction of the flow. The modification of the flow at various time intervals was tracked by a high-speed camera. The numerical simulation was carried out using the Suzen-Huang model and the Navier-Stokes equations.

Keywords: dielectric barrier discharge, microplasma, electrohydrodynamic flow, flow control, plasma actuator

1. Introduction

Active flow control is necessary in various industrial processes to improve system efficiency or to reduce environmental load [1]. In order to achieve flow control, mechanical actuators were developed and used. A new device for flow control was developed by Roth et al. in the 1990s [2]. A dielectric barrier discharge (DBD) was used and it was called a *plasma actuator*. The nonthermal plasma actuator operates at atmospheric pressure and compared with conventional types of actuators for flow control, has several advantages besides its simple construction, such as no moving parts and fast response [3, 4]. Plasma actuators for flow control were

investigated in applications for separation flow control [5–8] and noise reduction [8, 9]. The plasma actuator has an operating principle based on the electrohydrodynamic (EHD) phenomenon occurring due to the momentum transfer from ions accelerated by an electric field to neutral molecules by collision. Dielectric barrier discharge (DBD) and corona discharge are among the most common types of plasma actuators. A single DBD plasma actuator can induce a flow up to 7 m/s, and with a multiple DBD plasma actuator design, the value of induced flow can reach 11 m/s [10]. Various applications of flow control require different types of plasma actuators. For high-speed flow control, an induced flow speed of more than 7 m/s is necessary; thus instead of using a single DBD plasma actuator, the corona discharge could be used [11–15]. In the case of turbulent boundary-layer control for skin-friction drag reduction, millimeter-size discharge gap DBD plasma actuators were energized at peak-to-peak voltages of about 7 kV [16–19]. Research studies regarding the applications of plasma actuators involve turbulent boundary-layer separation control, steady airfoil leading-edge separation control, oscillating airfoils dynamic stall control, and circular cylinder wake control. According to various researchers, high values of the induced flow are desired. High values of the flow are obtained conventionally by energizing the plasma actuators at tens of kilovolts which are difficult to insulate and for which a large sized power supply is necessary. An effective actuation effect requires also a higher EHD force density that can be achieved using a micrometer order discharge gap plasma actuator, which lowers the discharge voltage and consequently requires lower power. Micro-sized plasma actuators were used for separation flow control and drag reduction [20–22]. A microplasma actuator was developed for flow control [23]. Similar electrode configurations were described in [24–28] but the required discharge voltages are more than 2 kV. Microplasma is a type of dielectric barrier discharge nonthermal plasma and its driven voltage is around only 1 kV. This technology could be used as a replacement of conventional technologies for surface treatment of polymers, indoor air treatment, biomedical applications, or flow control [29–32].

Measurements of microplasma actuators are difficult due to their micrometer size discharge gaps; thus, we have developed a numerical simulation of the induced flow based on the Suzen-Huang [33, 34] and Orlov [35] models. Due to the light emission from microplasma, observation and measurement of flow is difficult. Numerical simulations of the plasma actuator are carried out using the plasma fluid model and particle in cell model [36–39]. A simplified phenomenological model which does not model the species transport equations but can replicate the effects of the actuator in the air is the Suzen-Huang model [40]. Results close to the experimental data were obtained by various researchers who developed numerical simulations based on this model. It is less computationally expensive than solving the species transport equations [40, 41].

The microplasma actuator developed in our laboratory is thin and flexible and can be attached to any surface. To energize the actuator, small-sized power supplies are necessary; thus, a potential use for this actuator could be on drones. The electronic switching adds a greater flexibility in order to obtain flows in various directions. In comparison with macro-plasma actuators where the power supplies are bulky, the small-sized power supply necessary for a microplasma actuator adds little weight to the drone; also, less electrical insulation is necessary.

2. Microplasma actuator

A microplasma actuator was developed for flow control. Due to its small size, the experimental results were difficult to obtain near the active electrodes; thus, a numerical simulation was developed in order to simulate the flow and add additional information about the flow. The experimental and numerical simulation results showed the capability of the microplasma actuator to control the flow.

2.1. Experimental study of microplasma actuator

2.1.1. Characteristics of microplasma actuator

A schematic of the typical construction of a plasma actuator and the induced air flow is shown in **Figure 1**. A pulse or alternating high voltage is applied to the two electrodes with a dielectric layer in between; thus, a plasma is generated at the surface of the electrodes [42]. An electrohydrodynamic (EHD) phenomenon occurs because ions are accelerated by the electric field and furthermore collide with neutral molecules; thus, a momentum transfer occurs and air flow is generated [21, 43].

A microplasma actuator that can be driven by a lower voltage of less than 2 kVpp was developed and investigated. Owing to their low discharge voltage, the applied high voltage could be controlled easily using semiconductor switches. The structure of the microplasma actuator is shown in **Figure 2** [44]. A dielectric layer consisted of a polymer film of 25-μm thickness sandwiched in between a high voltage electrode and a grounded electrode. Voltages less than 2 kVpp are enough to generate a microplasma due to the thickness of the 25-μm discharge gap. A pulse high voltage power supply was used to energize the actuator with the schematic shown in **Figure 3**. Four field-effect transistors (FETs) are used with a DC high voltage power supply. The microplasma actuator is energized by a positive pulse voltage while FETs 1 and 4 are in the ON state and by negative pulse voltage while FETs 2 and 3 are in the ON state, respectively.

Figure 4 shows the experimental setup used to visualize and investigate the air flow induced by the microplasma actuator. The microplasma actuator was set on a Z stage. A high voltage probe (Tektronix, P6105A) connected to an oscilloscope (Tektronix, TDS 3014) was used to

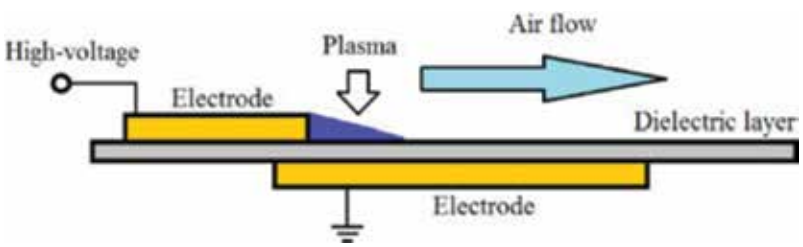

Figure 1. Typical construction of a plasma actuator. High voltage is applied to the electrodes with a thin dielectric layer in between.

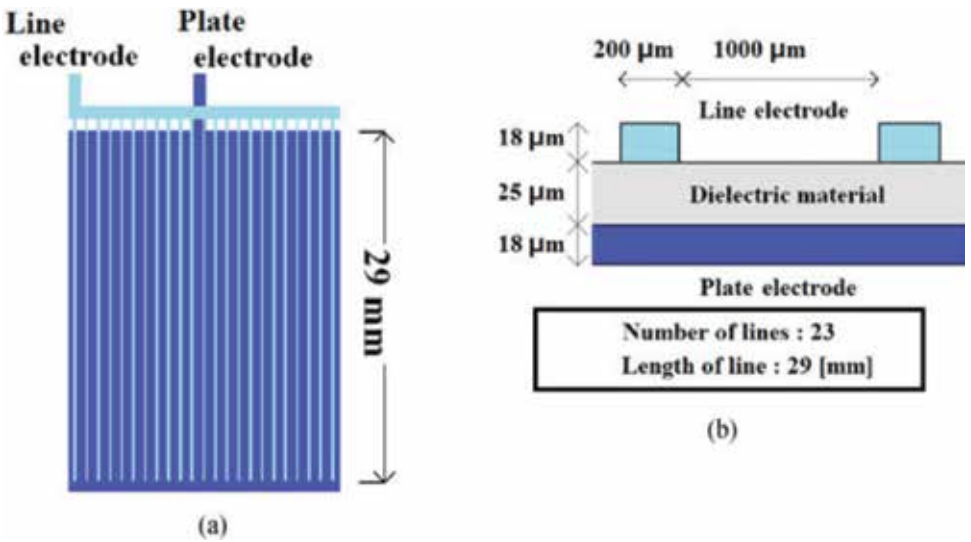

Figure 2. Geometry of the microplasma actuator. The four high voltage energized electrodes can be driven independently. (a) Top-view. (b) Cross-sectional view.

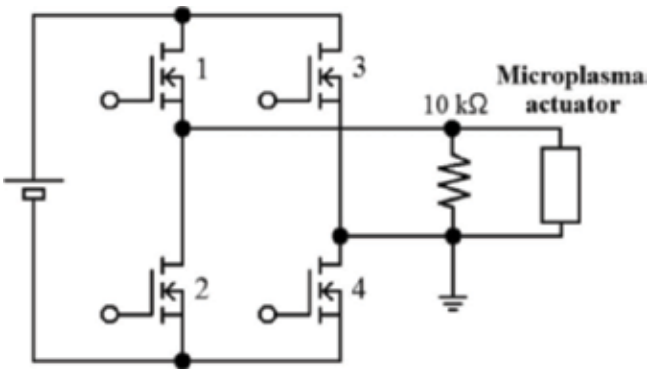

Figure 3. Schematic of pulsed high voltage source with semiconductor switches.

measure the discharge voltage. For the discharge current measurement, a current probe (Tektronix, P6021) connected to the oscilloscope was used. By multiplying the values of the voltage and current waveform measured with an oscilloscope, the discharge power was obtained for the pulse voltage. Furthermore, in order to calculate the discharge energy, the obtained discharge power waveform was integrated. Particle tracking velocimetry (PTV) was used as the method to measure the induced air flow by the microplasma actuator [45]. The microplasma actuator was placed inside an acrylic box and incense smoke with particles 0.3 μm in diameter [46] was inserted inside the box. For the measurement of the incense smoke particles, a laser particle counter (Kanomax, Model 3886) was used. For the flow measurements, a laser was used (Nd:YVO_4 532-nm) to irradiate the particles. The flow of tracer particles was recorded by a high-speed camera (Red Lake, Motionscope M3) having

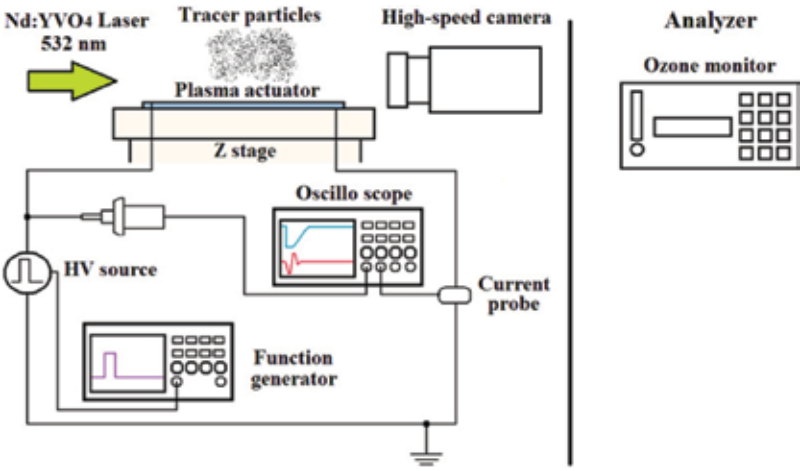

Figure 4. Experimental setup for visualization and measurement of the air flow induced by the microplasma actuator.

1280 × 1024-pixel resolution and 4000 Hz recording frequency. The area captured by the camera was 34 × 11 mm^2. The results were analyzed by the PTV method having a resolution of 1 mm in the x-axis and 0.5 mm in the y-axis. For the PTV method, steady state images of two continuous frames were used.

The Stokes number was calculated in order to estimate the ability of the incense smoke to follow the flow field [47], and the value was in the order of 10^{-5}; this is an acceptable flow tracing accuracy with error less than 1% [46]. Ozone concentration due to the microplasma was measured by an ozone monitor (Seki Electronics, SOZ-3300). The measurements were carried out by placing the microplasma actuator inside a glass tube which was connected to the ozone monitor at a distance of 90 cm.

The microplasma actuator could be energized by bipolar pulse as shown in **Figure 5** with T period and also positive and negative pulses as shown in **Figure 6(a)** and **(b)**. For both positive and negative pulses at a frequency of 2 kHz, the pulse width was 4 μs. The calculated energy consumption by integrating the discharge power waveform shown in **Figure 6** for a single pulse is shown in **Figure 7**. In order to have microplasma discharge, a voltage higher than 0.5 kV was necessary. The values of energy were almost the same for positive and negative pulses respectively; thus, at 1.4 kV, the calculated value of energy was about 800 μJ for both positive and negative pulses. This corresponds to an average power of 1.6 W.

Energy consumption was measured for a discharge voltage of 1.4 kV at various pulse frequencies for both polarities as shown in **Figure 8**. At 1 Hz, the energy consumption was about 650 μJ. With the increase of frequency, the single pulse energy consumption increased. This could be explained by the charges in plasma that due to the electric field were moved and trapped at the surface of the dielectric. These surface charges [48, 49], when the next opposite polarity is applied, will increase the electric field strength; furthermore, higher energy consumption for a single pulse was obtained with the increase of frequency. Due to recombination or diffusion, the surface charge will decrease in time.

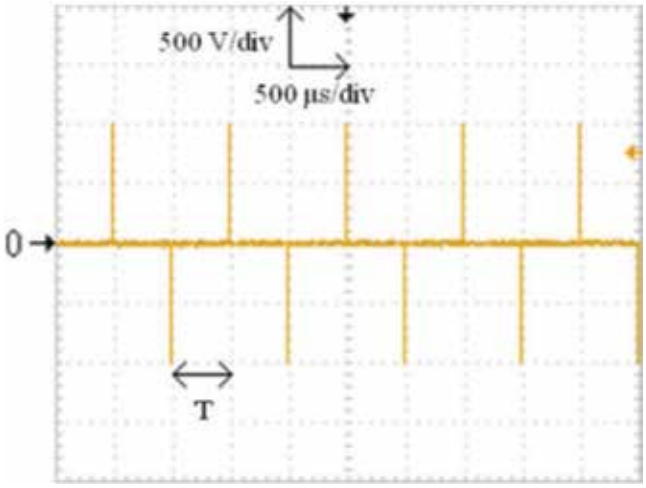

Figure 5. Waveform of pulsed high voltage applied to the microplasma actuator.

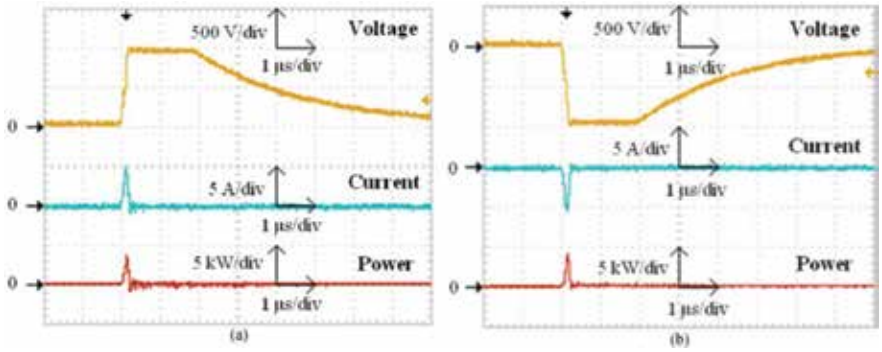

Figure 6. Waveforms of discharge voltage and corresponding discharge current and power. (a) Positive pulse. (b) Negative pulse.

Ozone (O_3) is harmful to humans due to its high oxidation ability, which is next to fluorine. The World Health Organization Air Quality Guidelines for Europe in its second edition imposed a value of 0.05 ppm as an 8-hours daily average concentration for ozone. The microplasma actuator generates ozone and the concentration of generated ozone was measured by energizing the actuator while it was rolled and inserted into an 8 mm diameter glass tube. An 1.5 L/min airflow was set inside the tube while the actuator was energized. The microplasma actuator was energized by a bipolar pulse with a frequency of 2 kHz. In **Figure 9** the characteristics of ozone concentration versus power consumption is shown. The microplasma actuator has an ozone yield of about 28 g/kWh, which is lower than what other researchers reported [50, 51]. Besides the fact that ozone causes damages to tissues, a higher concentration of ozone can cause the degradation of electrodes [52]. Thus, a low ozone yield is necessary for flow control applications [53].

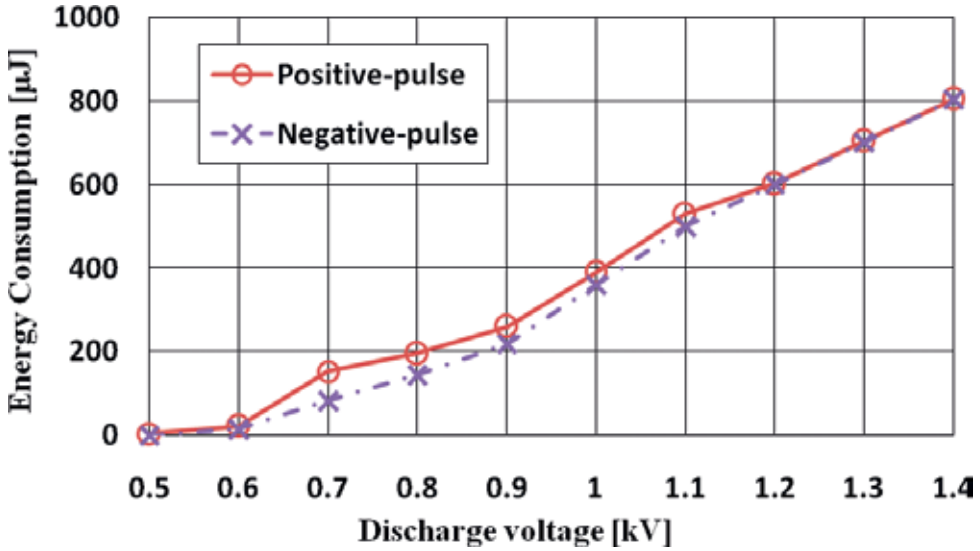

Figure 7. Energy consumption of single pulse versus discharge voltage for a pulse frequency of 2000 Hz.

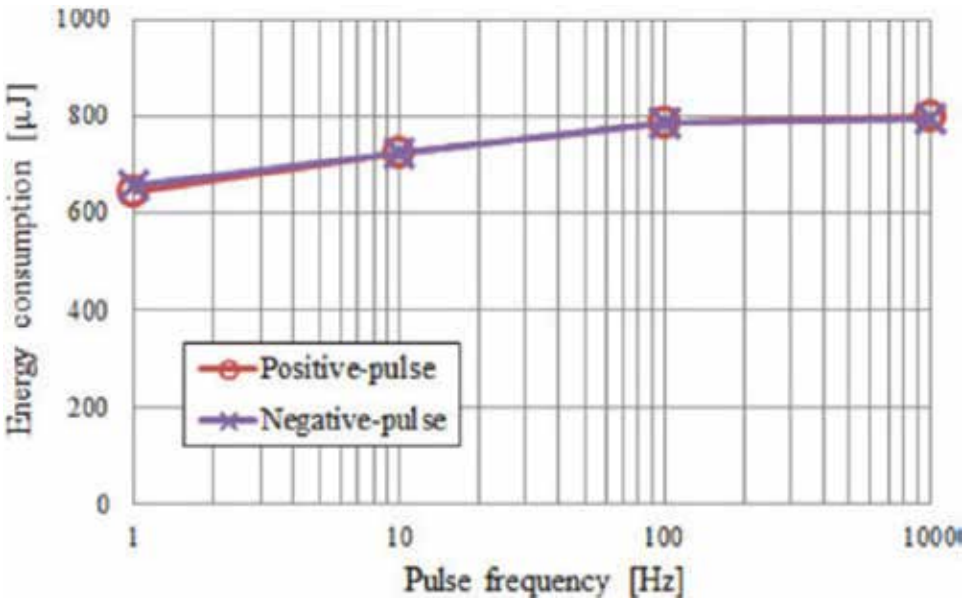

Figure 8. Energy consumption of a single pulse versus pulse frequency for a discharge voltage of 1.4 kV.

2.1.2. Flow control with microplasma actuator

The micro-scale plasma actuator, besides the requirement of low discharge voltage, has the advantage of easy integration due to its small size. A microplasma actuator similar to the one

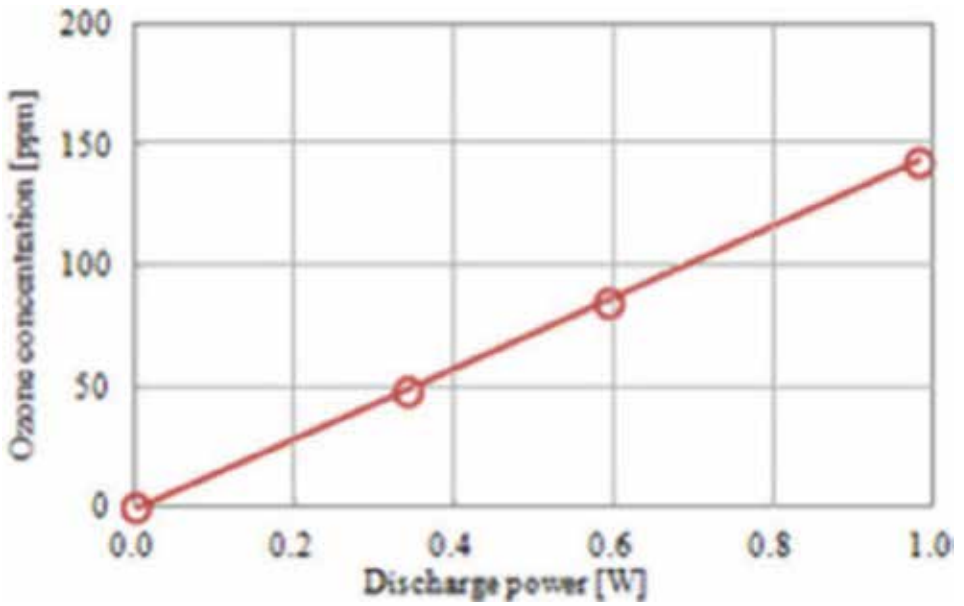

Figure 9. Ozone concentration measured while driving the microplasma actuator at 1.5 L/min. air flow.

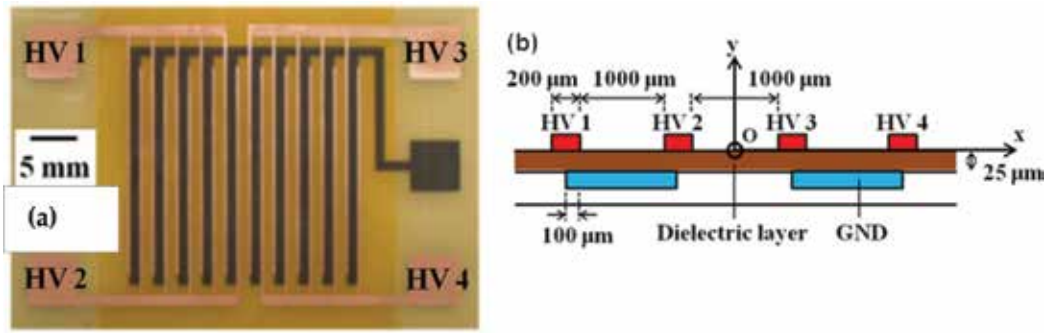

Figure 10. Microplasma actuator. Schematic image. Top-view showing (a) 20 strip-like electrodes and (b) cross-sectional view.

shown in **Figure 2** was developed. The schematic of a DBD microplasma actuator is shown in **Figure 10** [32, 41]. It consists of 20 strip-like electrodes with a 200 μm width and 16 μm thickness (top-side electrode) which are placed above a plate-like electrode (bottom-side electrode) with a dielectric layer of 25 μm thicknesses in between. Electrodes were made of copper and the dielectric layer was made of resin film. The gap is in micrometer order; thus, if only 1.4 kV is applied, the value of the obtained electric field is high (~10^7–10^8 V/m). This can be considered a low voltage and thus is easier to control and insulate and furthermore requires smaller sized power supplies. The resin film is a flexible polymer material that makes the microplasma actuator suitable for bending and attaching to various shapes, thus making the actuator suitable for flow control applications.

The flow was visualized using particle tracking velocimetry (PTV) [45]. Sub-micron size incense smoke was used as tracer particle and a Nd YVO4 532 nm laser was utilized to visualize the flow as shown in **Figure 4**. The phenomena induced by the microplasma actuator, was measured using a high-speed camera.

In the left part of the actuator ($x < 0$), the strips which were energized were marked as HV1 while the other strips were at floating potential as shown in **Figure 10**. The energized electrodes in the right part of the actuator ($x > 0$) were marked as HV4 while the other strips were at floating potential. The electrodes below the dielectric layer were grounded. The duty ratio of the actuator is defined as D by subtracting from 100% the duty ratio of the voltage applied to the HV4 electrodes. The duty ratios of HV1 and HV4 have a sum of 100%.

A duty ratio of $D = 80\%$ represents a duty ratio of 20% for the HV4 electrodes and a duty ratio of 80% for the HV1 electrodes.

The waveform of the applied voltage with $D = 20\%$ is shown in **Figure 11**. The peak of the AC applied voltage was 1.4 kV at a 20 kHz frequency. The burst frequency for the applied voltage was 4 kHz.

In the initial stages of the discharge, vortexes appeared near the active electrodes as shown in **Figure 12** at 2.5 and 5 ms, respectively. The duty ratio was $D = 20\%$; thus, the vortexes near the HV1 electrodes are rotating counter-clockwise and the vortexes near the HV4 electrodes are rotating clockwise. The flow velocity is higher for the HV1 electrodes since the duty ratio is 20% (HV1 electrodes are energized for a shorter time compared with HV4 electrodes). Gradually, the vortexes join together and leftward flow is established up to 50 ms.

2.2. Numerical simulation study of microplasma actuator

We have developed a numerical simulation code based on the Suzen model [33, 34]. According to the model, the EHD force is:

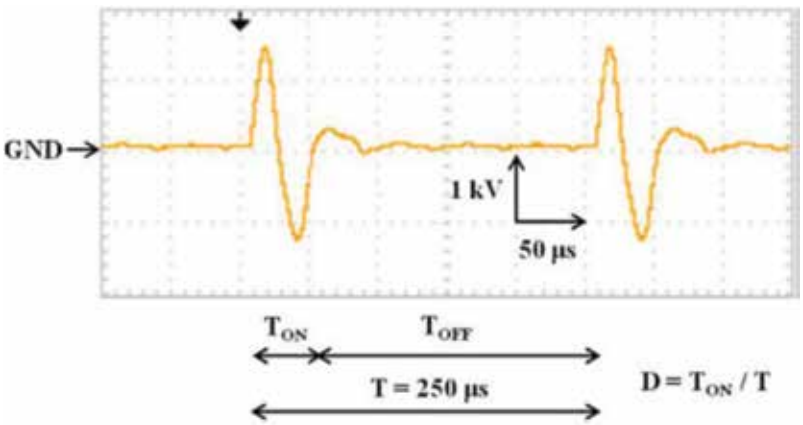

Figure 11. Waveform of applied voltage. The duty ratio is the ratio between the time in which the voltage is on and the sum of the time on plus time off.

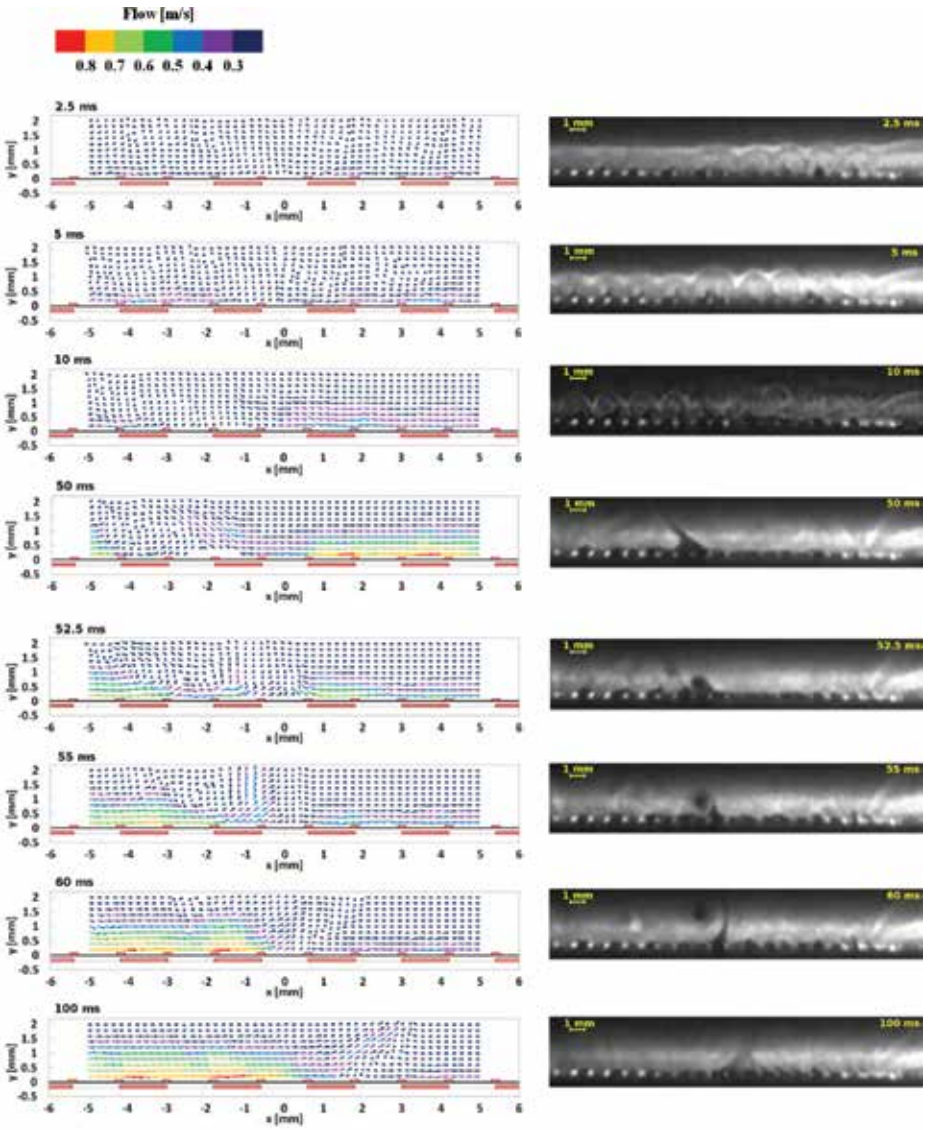

Figure 12. PTV results for four active electrodes (left side) and images of the flow for the entire actuator (right side). $D = 20\%$ up to 50 ms and $D = 70\%$ for more than 50 ms.

$$\vec{f} = \rho_c \cdot \vec{E}\,, \tag{1}$$

where f represents the body force per unit volume, ρ_c represents the net charge density, and E represents the intensity of the electric field. In this model, magnetic forces were considered. Furthermore, the electric field:

$$\vec{E} = -\nabla V \tag{2}$$

where V represents the potential. Gauss' law is written as:

$$\nabla\left(\varepsilon \cdot \vec{E}\right) = \rho_c \tag{3}$$

and furthermore:

$$\nabla(\varepsilon \cdot \nabla V) = -\rho_c \tag{4}$$

where ε represents the permittivity that was calculated as the product of relative permittivity ε_r and the permittivity of free space ε_0. Using the potential V and the Debye length $\lambda_{D,}$ the charge density is expressed as [33, 34]:

$$\frac{\rho_c}{\varepsilon_0} = \left(\frac{-1}{\lambda_D^2}\right) V. \tag{5}$$

Using Eqs. (1) and (5), the body force is calculated. In the Suzen model, it is assumed that the gas particles are weakly ionized; thus, the potential V can be decoupled in a potential due to the external electric field Ø and a potential due to the net charge density φ [33, 34]:

$$V = \phi + \varphi \tag{6}$$

Two independent equations can be written as:

$$\nabla\left(\varepsilon_r \cdot \nabla\phi\right) = 0 \tag{7}$$

$$\nabla(\varepsilon_r \cdot \nabla\varphi) = \frac{-\rho_c}{\varepsilon_0}. \tag{8}$$

If we consider:

$$\frac{\rho_c}{\varepsilon_0} = \left(\frac{-1}{\lambda_D^2}\right)\varphi \tag{9}$$

We can write Eq. (8) as:

$$\nabla(\varepsilon_r \cdot \nabla\rho_c) = \frac{\rho_c}{\lambda_D^2} \tag{10}$$

Furthermore, the body force is calculated by

$$\vec{f} = \rho_c \cdot \vec{E} = \rho_c(-\nabla\varphi) \tag{11}$$

The permittivity between the dielectric and air was considered as the harmonic mean between dielectric permittivity taken as $\varepsilon_{rd} = 4$ and air permittivity $\varepsilon_{rair} = 1$; thus, the electric field was conserved [33]. Neumann boundary conditions were used for Eq. (7) as outer boundary conditions:

$$\frac{\partial \varphi}{\partial n} = 0 \tag{12}$$

Dirichlet boundary conditions were used for Eq. (10) as the outer boundary conditions:

$$\rho_c = 0. \tag{13}$$

In the numerical simulation code, in the dielectric, the values of u and v were 0. Using Eq. (10), the charge distribution over the encapsulated electrode was calculated considering the covered electrodes as the source charge. A value of $\rho c = 0.00751$ C/m^3 was used for the source charge. The same values as Suzen [34] were used for the Debye length with $\lambda_D = 0.00017$ m for air and $\lambda_D = \infty$ for the dielectric. Good agreement with experimental data was obtained for these values. After solving Eq. (11), the value of the body force was inserted in the Navier-Stokes equations:

$$\frac{\partial u}{\partial t} + u\frac{\partial u}{\partial x} + v\frac{\partial u}{\partial y} = \frac{-1}{\rho}\frac{\partial p}{\partial x} + \upsilon\left(\frac{\partial^2 u}{\partial x^2} + \frac{\partial^2 u}{\partial y^2}\right) + Fx \tag{14}$$

$$\frac{\partial v}{\partial t} + u\frac{\partial v}{\partial x} + v\frac{\partial v}{\partial y} = \frac{-1}{\rho}\frac{\partial p}{\partial y} + \upsilon\left(\frac{\partial^2 v}{\partial x^2} + \frac{\partial^2 v}{\partial y^2}\right) + Fy \tag{15}$$

$$\frac{\partial^2 p}{\partial x^2} + \frac{\partial^2 p}{\partial y^2} = -\rho\left(\frac{\partial u}{\partial x}\frac{\partial u}{\partial x} + 2\frac{\partial u}{\partial y}\frac{\partial v}{\partial x} + \frac{\partial v}{\partial y}\frac{\partial v}{\partial y}\right) \tag{16}$$

where u and v represent the components of the flow velocity on the x-axis and y-axis, ρ is the fluid density, p is the pressure, and υ is the kinematic viscosity. The dynamic viscosity μ is written as:

$$\mu = \varrho\, \upsilon \tag{17}$$

We have used for the air density, $\rho = 1.177$ kg/m^3 and for the kinematic viscosity, $\upsilon = 1.57 \times 10^{-5}$ m^2/s; thus, the calculated dynamic viscosity $\mu = 1.8 \times 10^{-5}$ kg/ms. The computational geometry is shown in **Figure 13**. The dimensions of the grid were 14 × 14 mm with 561 × 561 grid points. For solving Eqs. (7) and (10), the convergence parameter was 10^{-8}. A projection method in primitive variables on a collocated mesh was used for solving the Navier-Stokes equations.

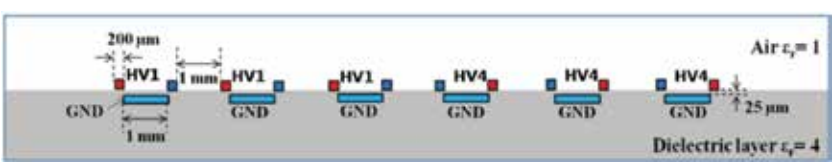

Figure 13. Computational geometry. Upper electrodes HV1 and HV4 were energized and the encapsulated electrodes were grounded.

The microplasma actuator shown in the experimental part had 20 strip-like exposed electrodes. These conditions while keeping a high mesh density necessary for accurate results will also increase the simulation time; thus, we chose for the numerical simulation, 12 exposed electrodes and 6 covered electrodes as shown in **Figure 13**. The energized electrodes were labeled HV1 (3 electrodes) and HV4 (3 electrodes). In the experimental part, the electrodes were energized at an AC waveform having an amplitude of 1.4 kV and a frequency of 20 kHz. The signal was modulated at 4 kHz with duty ratios of 20, 30, 70, and 80%. Considering that the effective value of 1.4 kV peak is 1 kV, we chose for computational reasons for the simulation that the applied voltage is a positive pulse signal with a peak value of 1 kV. Duty ratios for the positive pulse were 20, 30, 70, and 80% as shown in **Figure 14**.

Eqs. (7), (10), and (11) were solved to obtain the potential of the external electric field Ø, the potential of the net charge density φ, and the body force. These were calculated before solving the Navier-Stokes, as shown in **Figure 15**. Near the active electrodes HV1 and HV4, high values of the body force were calculated. For developing the numerical simulation code, the Julia programming language was used [54]. The same duty ratios were used as in the experimental part: first case when electrodes HV1 were energized at 20% duty ratio and HV4 electrodes were energized at 80%; thus, the actuator duty ratio D = 20%, and second case where HV1 electrodes were energized at 70% duty ratio and HV4 electrodes were energized

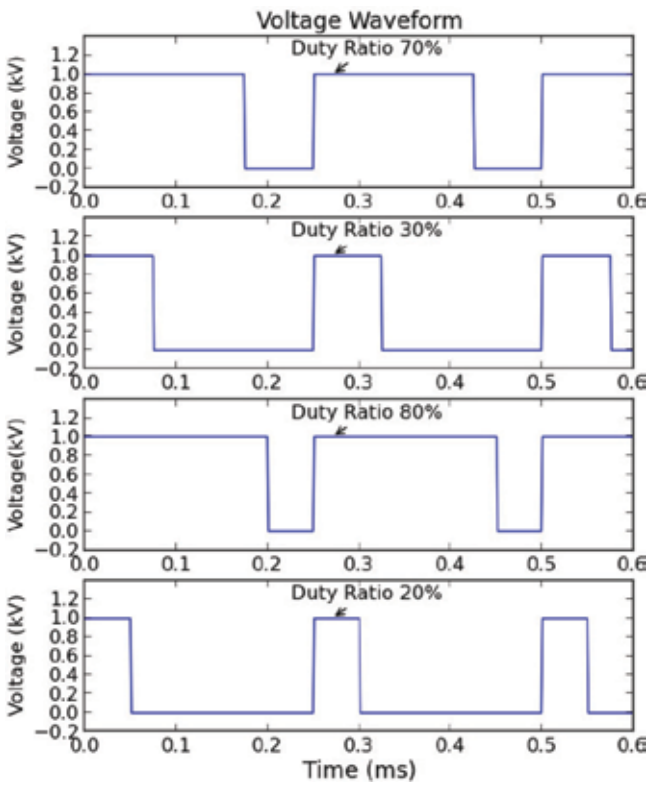

Figure 14. Simulation voltage waveforms. Positive pulse with duty ratio of 70, 30, 80, and 20%.

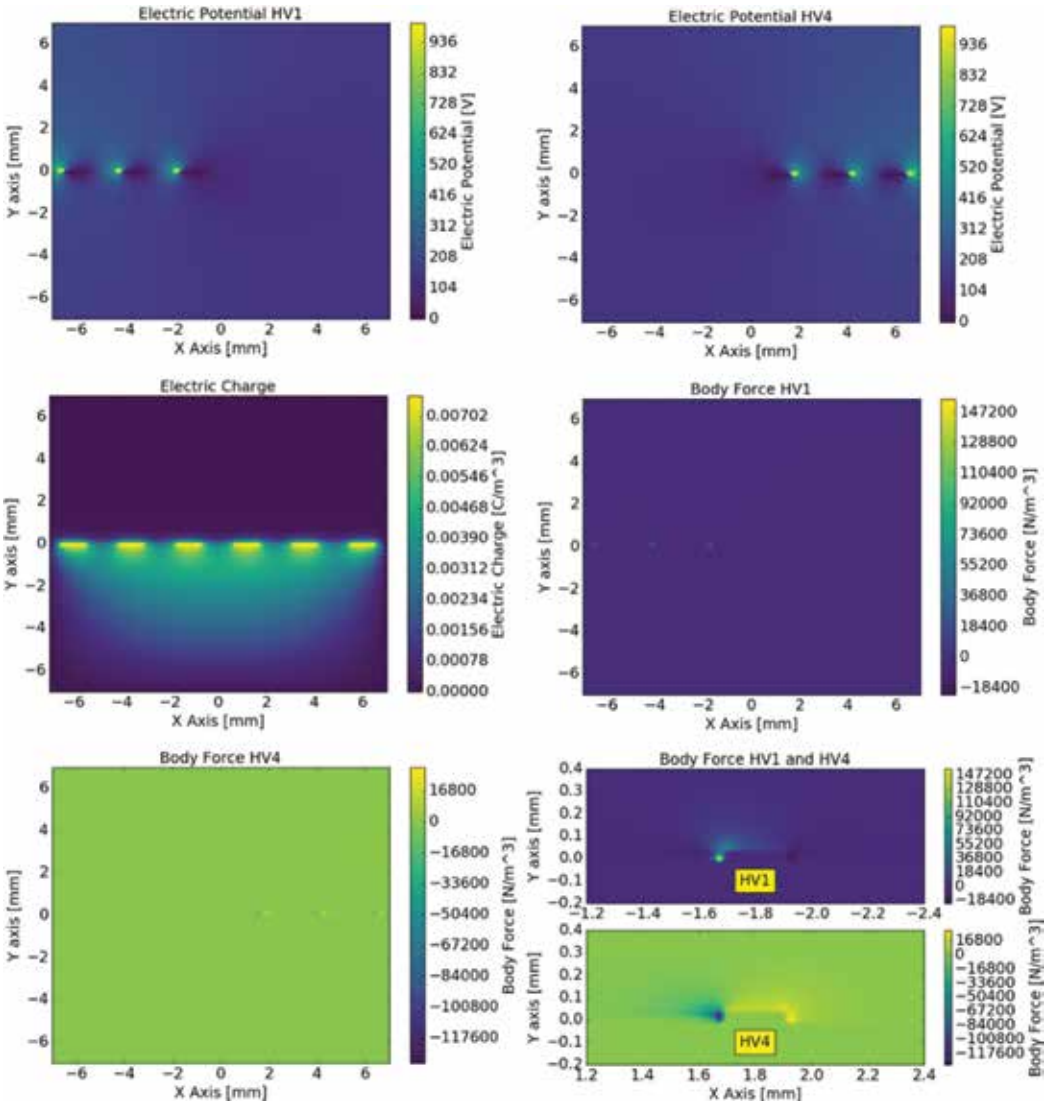

Figure 15. Calculated electric potential, charge density, and body force: Electrodes HV1 and HV4 = 1000 V; covered electrode = 0 V. Higher values of body force were obtained near the active exposed electrodes (shown in HV1 and HV4 enlarged).

at 30%; thus, actuator duty ratio D = 70%. The results for D = 20% are shown in **Figure 16**. Vortexes appeared in the initial stages of the phenomena up to 5 ms. As was observed also in the experimental results, the vortexes appeared above the covered electrodes and had a counter-clockwise direction near the HV1 electrodes and clockwise direction near the HV4 electrodes. With the lapse of time at t = 10 ms, the vortexes moved up; thus, at 15 ms, it can be observed that the vortexes start to join together and create a flow directed diagonal to the left. At 50 ms, the flow is in a steady state with an extended diagonal flow toward the left as

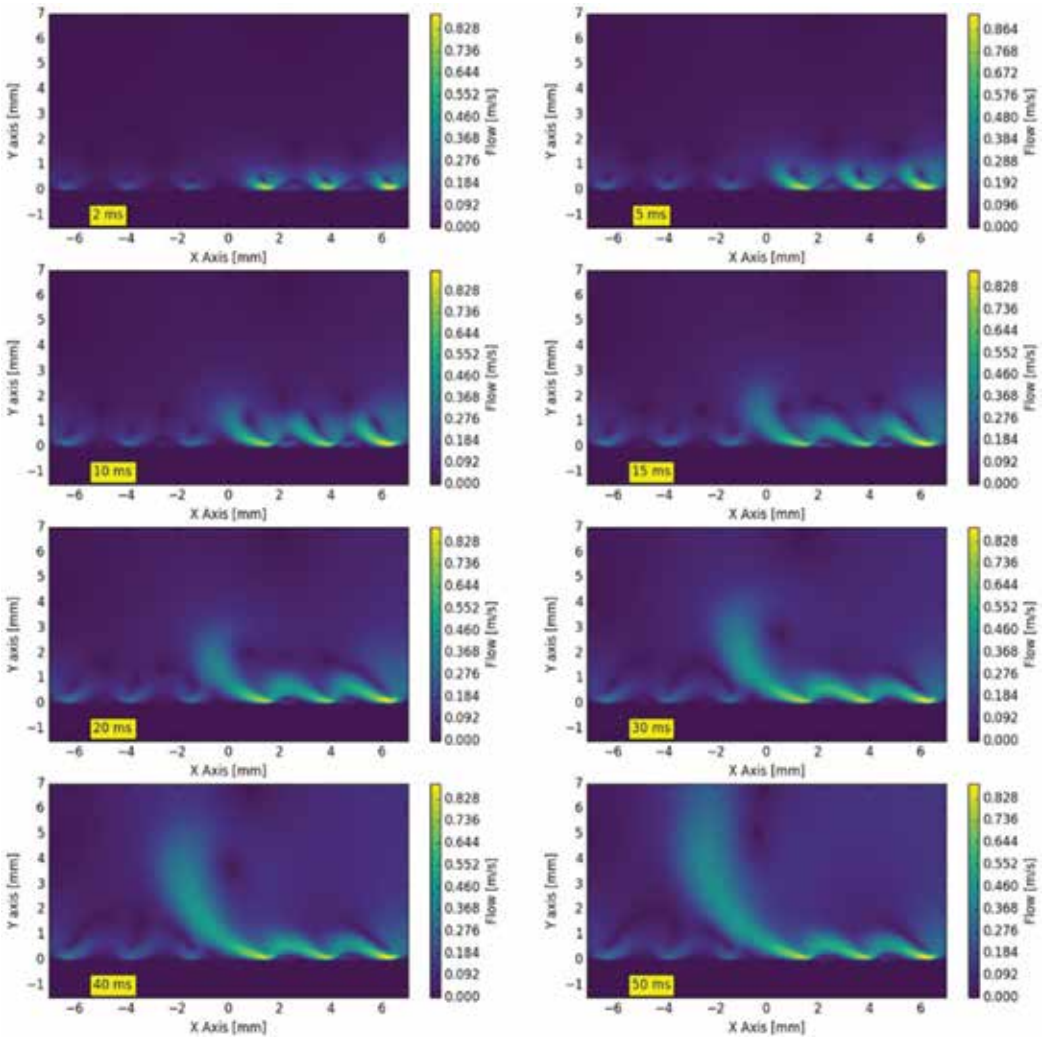

Figure 16. Flow: Flow for duty ratio D = 20%: Initial vortexes appeared (2 ms); vortexes increase in size (10 ms); leftward flow steady state (50 ms).

observed in the experimental results. The maximum calculated value of the flow of 0.83 m/s was near the active electrodes and the value of the flow in the diagonal direction was 0.45 m/s. The PTV measured value of the diagonal flow was 0.43 m/s, which is in agreement with numerical simulations. The duty ratio of the actuator after 50 ms was D = 70%.

In **Figure 17** are shown the simulation results for D = 70%. The electrodes HV1 are energized for a longer time compared with HV4 electrodes; thus, the flow near the HV1 electrodes is faster. The direction of the diagonal flow obtained up to 50 ms is changing gradually, from leftward to rightward as measured by the PTV method. Vortexes are observed near the HV1 electrodes up to 55 ms. A complete tilt toward the right part is observed at 80 ms. At 120 ms, it can be considered that a steady state was achieved.

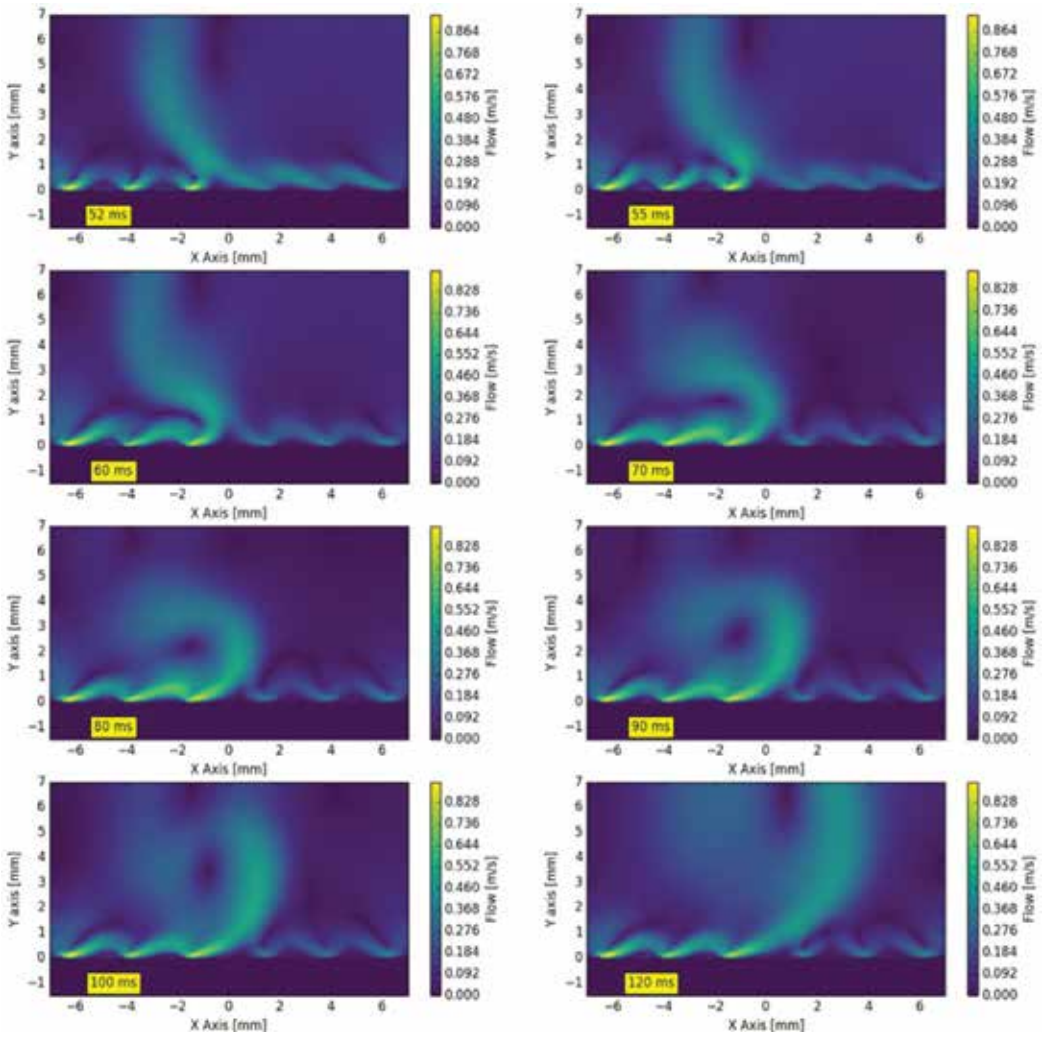

Figure 17. Flow for duty ratio D = 70%: After 50 ms, the leftward diagonal flow is changing gradually to rightward diagonal flow.

The maximum values of the flow of 0.82 m/s were calculated near the HV1 electrodes. For the diagonal flow, the value was 0.43 m/s. The value obtained by PTV method was 0.42 m/s for the diagonal flow. In the case of experimental results, due to the microplasma light emission near the active electrodes, the flow could not be measured properly; thus, the simulation gave us valuable insight into the microplasma actuator phenomena. The leftward diagonal flow obtained at D = 20% has a smaller angle with the horizontal axis compared with the rightward diagonal flow at D = 70%.

3. Conclusions

A microplasma actuator is a device with no moving parts that has advantages over conventional actuators. It can be energized at voltages of about 1 kV, and thus requires a smaller size power supply and less electrical insulation compared with macro-plasma actuators. Moreover, due to the use of pulse voltage to energize the actuator, the energy consumption is low.

The use of a microplasma actuator for flow control showed the capability of the actuator to induce flow and also to change the direction of the flow. By using devices with field-effect transistor (FET) switches to energize the actuator, the flow direction was changed from diagonal leftward to diagonal rightward when the duty ratio of applied voltage was changed. This could be useful if the actuator were to be attached to small drones. The characteristics of the flow were investigated both experimentally and using numerical simulations. A numerical simulation code was developed based on the Suzen-Huang model, which calculates the body force from the potential of the external electric field and the potential of the charge density of the plasma, and implements the body force in Navier-Stokes equations. The experimental results confirmed the validity of the developed code.

Acknowledgements

The authors would like to thank Professor Hitoki Yoneda from the University of Electro-Communications, Tokyo, Professor Damon Chandler, Mr. Yoshinori Mizuno, Mr. Akihiko Ito and Mr. Daisuke Nonaka from Shizuoka University, Hamamatsu, for the fruitful discussions.

Author details

Kazuo Shimizu* and Marius Blajan

*Address all correspondence to: shimizu@cjr.shizuoka.ac.jp

Shizuoka University, Hamamatsu, Japan

References

[1] Gadelhak M. Flow Control. Cambridge: Cambridge University Press; 2000

[2] Roth JR, Din X. Optimization of the aerodynamic plasma actuator as an electrohydrodynamic (EHD) electrical device. In: Proceedings of the 44th AIAA Aerospace Sciences Meeting Exhibit; January 9–12, 2006. DOI: 10.2514/6.2006-1203

[3] Singh KP, Roy S. Impedance matching for an asymmetric dielectric barrier discharge plasma actuator. Journal of Applied Physics. 2008;**103**:013305

[4] Neumann M, Friedrich C, Kriegseis J, Grundmann S, Czarske J. Determination of the phase-resolved volume force produced by a dielectric barrier discharge plasma actuator. Journal of Physics D: Applied Physics. 2013;**46**:042001

[5] Jacob JD, Ramakumar K, Anthony R, Rivir RB. Control of laminar and turbulent shear flows using plasma actuators. In: Proceedings of the 4th International Symposium Turbulence Shear Flow Phenomena; June 27–29, 2005

[6] Im S, Do H, Cappelli MA. Dielectric barrier discharge control of a turbulent boundary layer in a supersonic flow. Applied Physics Letters. 2010;**97**:041503

[7] Goksel B et al. Pulsed plasma actuators for separation flow control. In: Proceedings of the Conference Turbulence Interactions; 2006. DOI: 10.13140/RG.2.1.2275.5925

[8] Thomas FO, Kozlov A, Corke TC. Plasma actuators for bluff body flow control. Journal of AIAA. 2008;**46**(8):1921-1931

[9] Li Y, Zhang X, Huang X. The use of plasma actuators for bluff body broadband noise control. Experiments Fluids. 2010;**49**:367-377

[10] Benard N, Moreau E. Electrical and mechanical characteristics of surface AC dielectric barrier discharge plasma actuators applied to airflow control. Experiments in Fluids. 2014; **55**:1846. DOI: 10.1007/s00348-014-1846-x

[11] Zhao L, Adamiak K. Electrohydrodynamic flow produced by electric corona discharge (numerical and experimental studies, and applications). In: Proceedings of the 2009 Electrostatics Joint Conference, Boston, P2.13; June 16–18, 2009

[12] Colas DF, Ferret A, Pai DZ, Lacoste DA, Laux CO. Ionic wind generation by a wire-cylinder-plate corona discharge in air at atmospheric pressure. Journal of Applied Physics. 2010;**108**:103306

[13] Robinson M. Movement of air in the electric wind of the corona discharge. Transactions of the American Institute of Electrical Engineers. 1961;**80**:143-150

[14] June MS, Kribs J, Lyons KM. Measuring efficiency of positive and negative ionic wind devices for comparison to fans and blowers. Journal of Electrostatics. 2011;**69**:345-350

[15] Kim C, Park D, Noh KC, Hwang J. Velocity and energy conversion efficiency characteristics of ionic wind generator in a multistage configuration. Journal of Electrostatics. 2010; **68**:36-41

[16] Touchard G. Plasma actuators for aeronautics applications – state of art review. IJPEST. 2008;**2**(1):1-25

[17] Whalley RD, Choi K-S. The starting vortex in quiescent air induced by dielectric-barrier-discharge plasma. Journal of Fluid Mechanics. 2013;**703**:192203

[18] Whalley RD, Choi K-S. Turbulent boundary-layer control with plasma spanwise travelling waves. Experiments in Fluids. 2014;**55**:1796

[19] Choi K-S, Jukes T, Whaley R. Turbulent boundary-layer control with plasma actuators. Philosophical Transactions of the Royal Society A. 2011;**369**:1443-1458

[20] Wang C-C, Roy S. Microscale plasma actuators for improved thrust density. Journal of Applied Physics. 2009;**106**:013310

[21] Wang C-C, Roy S. Energy and force prediction for a nanosecond pulsed dielectric barrier discharge actuator. Journal of Applied Physics. 2012;**111**:103302

[22] Shyy W, Jayaraman B, Andersson A. Modeling of glow discharge-induced fluid dynamics. Journal of Applied Physics. 2002;**92**(11):6434-6443

[23] Shimizu K, Mizuno Y, Blajan M. Basic study on force induction using dielectric barrier microplasma array. Japanese Journal of Applied Physics. 2015;**54**:01AA07

[24] Santhanakrishnan A, Jacob J. On plasma synthetic jet actuators. In: 44th AIAA Aerospace Science Meeting and Exhibit, Reno; January 9–12, 2006. p. 685

[25] Bolitho M, Jacob J. Active vortex generators using jet vectoring plasma actuators. SAE International Journal of Aerospace. 2008;**1**(1):610-618

[26] Bénard N, Jolibois J, Moreau E, Sosa R, Artana G, Touchard G. Aerodynamic plasma actuators: A directional micro-jet device. Thin Solid Films. 2008;**516**:6660-6667

[27] Neretti G, Cristofolini A, Borghi CA. Experimental investigation on a vectorized aerodynamic dielectric barrier discharge plasma actuator array. Journal of Applied Physics. 2014; **115**:163304

[28] Shimizu K, Kuwabara T, Blajan M. Study on decomposition of indoor air contaminants by pulsed atmospheric microplasma. Sensors. 2012;**12**(11):14525-14536

[29] Blajan M, Shimizu K. Temporal evolution of dielectric barrier discharge microplasma. Applied Physics Letters. 2012;**101**:104101

[30] Shimizu K, Blajan M, Tatematsu S. Basic study of remote disinfection and sterilization effect by using atmospheric microplasma. IEEE Transactions on Industry Applications. 2012;**48**:1182-1188

[31] Blajan M, Umeda A, Muramatsu S, Shimizu K. Emission spectroscopy of pulsed powered microplasma for surface treatment of PEN film. IEEE Transactions on Industry Applications. 2011;**47**:1100-1108

[32] Mizuno Y, Blajan M, Yoneda H, Shimizu K. Active fluid control by multi-electrode microplasma actuator. Journal of Institute of Electrostatics Japan. 2015;**39**:15 [in Japanese]

[33] Suzen YB, Huang PG, Jacob JD, Ashpis DE. Numerical simulations of plasma based flow control applications. In: 35th Fluid Dynamics Conference and Exhibit; June 6–9, 2005; Toronto. AIAA. pp. 2005-4633

[34] Suzen YB, Huang PG, Ashpis DE. Numerical simulations of flow separation control in low-pressure turbines using plasma actuators. In: 45th AIAA Aerospace Sciences Meeting and Exhibit; January 8–11, 2007; Reno. AIAA; 2007. p. 937

[35] Orlov DM. Modelling and simulation of single dielectric barrier discharge plasma actuator. PhD thesis, University of Notre Dame; 2006

[36] Unfer T, Boeuf JP. Modeling of a nanosecond surface discharge actuator. Journal of Physics D: Applied Physics. 2009;**42**:194017

[37] Likhanskii AV, Shneider MN, Macheret SO, Miles RB. Modeling of dielectric barrier discharge plasma actuator in air. Journal of Applied Physics. 2008;**103**:053305

[38] Nishida H, Abe T. Numerical analysis for plasma dynamics in SDBD plasma actuator. In: 41st Plasma Dynamics and Lasers Conference; June 28–July 1, 2010

[39] Bai J, Sun J, Zhang Q, Wang D. PIC simulation of RF hydrogen discharges in a transverse magnetic field. Current Applied Physics. 2011;**11**:S140-S144

[40] Mahfoze O, Laizet S. Skin-friction drag reduction in a channel flow with streamwise-aligned plasma actuators. International Journal of Heat and Fluid Flow. 2017;**66**:83-94

[41] Blajan M, Mizuno Y, Ito A, Shimizu K. Microplasma actuator for EHD induced flow. IEEE Transaction on Industry Applications. 2017;**53**(3):2409-2415

[42] Moreau E, Sosa R, Artana G. Electric wind produced by surface plasma actuators: A new dielectric barrier discharge based on a threeelectrode geometry. Journal of Applied Physics. 2008;**41**:115204

[43] Dawson R, Little J. Characterization of nanosecond pulse driven dielectric barrier discharge plasma actuators for aerodynamic flow control. Journal of Applied Physics. 2013; **113**:103302

[44] Shimizu K, Mizuno Y, Blajan M, Yoneda H. Characteristics of an atmospheric nonthermal microplasma actuator. IEEE Transaction on Industry Applications. 2017;**53**(2):1452-1458

[45] Fu S, Biwole PH, Mathis C. Particle tracking velocimetry for indoor airflow field: A review. Building and Environment. 2015;**87**:34-44

[46] Pescini E, Giorgi MGD, Francioso L, Sciolti A, Ficarella A. Effect of amicro dielectric barrier discharge plasma actuator on quiescent flow. Science, Measurement and Technology. 2014;**8**(3):135-142

[47] Yoon SY, Ross JW, Mench MM, Sharp KV. Gas-phase particle image velocimetry (PIV) for application to the design of fuel cell reactant flow channels. Journal of Power Sources. 2006;**160**:1017-1025

[48] Celestin S, Bonaventura Z, Guaitella O, Rousseau A, Bourdon A. Influence of surface charges on the structure of a dielectric barrier discharge in air at atmospheric pressure: Experiment and modeling. European Physical Journal Applied Physics. 2009;**47**(2):22810

[49] Bronold FX, Fehske H, Heinisch RL, Marbach J. Wall charge and potential from a microscopic point of view. Contributions to Plasma Physics. 2012;**52**:356-863

[50] Pietscha GJ, Gibalovb VI. Dielectric barrier discharges and ozone synthesis. Pure and Applied Chemistry. 1998;**70**(6):1169-1174

[51] Buntat Z, Smith IR, Razali NAM. Ozone generation by pulsed streamer discharge in air. Applied Physics Research. 2009;**2**:1

[52] Tanaka M, Ogawa S, Wada N, Yoshiyasu H, Yagi S. Influence of rust on electrodes of oxygen-fed ozonizer to ozone generation. IEEJ Transactions on Fundamentals and Materials. 2006;**125**(10):817-822

[53] Kawamoto H, Koboyashi T. Ozone generation in plasma actuator. Japan Society of Mechanical Engineers Series B. 2009;**75**(759):2345-2347

[54] 2018. [Online]. Available: http://julialang.org

Chapter 2

An SU-8 Microgripper Based on the Cascaded V-Shaped Electrothermal Actuators: Design, Fabrication, Simulation and Experimental Investigations

Rodica-Cristina Voicu

Additional information is available at the end of the chapter

http://dx.doi.org/10.5772/intechopen.75544

Abstract

This chapter presents the design, fabrication, numerical simulations and experimental investigations of a polymeric microgripper designed using the cascaded V-shaped electro-thermal actuators. The microgripper has a total length around 1 mm and a total thickness of only 20 μm. The microgripper was simulated using electro-thermo-mechanical finite element method (FEM) in order to check the performance of the gripper. As structural material of the microgripper, the SU-8 biocompatible polymer was used during the fabrication process. A fabrication process was implemented to realize the microgripper using a symmetrically sandwich structure. The metallic micro-heaters were encapsulated in the polymeric actuation structure of the microgrippers to reduce the undesirable out-of-plane displacement of the gripper tips and the mechanical stress, to improve the thermal efficiency, and for obtaining the electrical isolation of the structure. Experimental testing has been performed to determine the openings and the temperatures of the microgripper tips as function of electrical current. A displacement of the tips of more than 50 μm can be obtained at an electrical current of around 26–28 mA. A comparison between the simulation results and the measurements were also presented.

Keywords: actuator, electro-thermal, microgripper, SU-8, simulation, polymer

1. Introduction

Microgrippers used as end-effectors are essential tools for holding and manipulating fragile objects. A variety of applications for the microgripper structures was reported. These tools are suitable for handling, positioning, pick and place and biological micro-manipulations such as

cells, blood vessels and tissues, for applications in micro-assembly of Microelectromechanical Systems (MEMS) and MOEMS components (lenses, fibers) and in micro-robotics.

Different actuators were investigated due to the significant role in the MEMS configuration. The actuation methods include mainly the electrostatic, electromagnetic, piezoelectric and electrothermal principles. Each actuation approaches have their proper disadvantages and benefits in agreement with the designed purpose. The actuators are usually integrated with MEMS for the necessary need of energy conversion, motion generation and force production [1–3]. The V-shaped actuators are widely used for grippers, micro-valves, micro-pumps and other devices. V-shaped electrothermal actuators have the advantages of generating a large force (up to several 100 mN), the simple structure design, a lower dive voltage and a large deformation. Que et al. [2] developed single and cascaded V-shaped electrothermal actuators and present the experimental results. Shen and Chen [3] present an analytical model for cascaded V-shaped actuators bringing a complete description of the mechanical performance. Usually, materials such as silicon, polysilicon or aluminum are used as the structural material of such actuators.

A variety of microgrippers have been studied using the SU-8 based electrothermal actuators designed on different configurations such as, U-shape or V-shape. This is proving the interest in the bio-micro-manipulation domain [1, 4–23]. SU-8 is a highly crosslinked epoxy-type photo-patternable polymer which has been used extensively as the preferred polymer material for fabrication of biocompatible structures. The SU-8 polymer has a relatively large coefficient of thermal expansion (CTE) of 52 ppm, good mechanical strength with a modulus of elasticity of around 4.02 GPa and good thermal stability with a glass transition temperature of 210°C [15], which make it a good polymer material for fabrication of electrothermal actuators. The polymer V-shaped actuators are preferred for the better performance in aqueous medium [4].

Different processing technologies were investigated and realized in order to fabricate reliable microgripper with reduces out-of-plane displacement [17–22]. Usually two or three material layers are utilized to compose a sandwich structure.

In this chapter, we report a complete work regarding the design, numerical simulation results, fabrication process and the experimental investigations of an SU-8 polymeric microgripper. The design is based on the cascaded V-shaped electrothermal actuators. The SU-8 microgripper can be used for micro-robotics and bio-manipulation and assembly applications. The microgripper was numerically investigated using the coupled electro-thermo-mechanical simulations based on finite element method (FEM) and using the Coventorware 2014 software in order to confirm the performance of the microgripper. To fabricate the microgripper, a sandwich structure actuator with three layers was used. Two kings of fabrication processes were presented in order to improve the structure functionality. As structural material of the microgripper, the SU-8 biocompatible polymer was used during the fabrication process. The metallic micro-heaters were encapsulated in the polymeric actuation structures of the microgrippers to reduce the undesirable out-of-plane displacement of the gripper tips, the mechanical stress and to improve the thermal efficiency and the electrical isolation of the structure. Experimental testing and characterizations have been performed to determine the openings and the temperatures of the microgripper tips as function of electrical current. A comparison between the simulation results and the measurements were also presented.

2. Design

The SU-8 microgripper was designed in a previous work using the principle of the cascaded V-shaped electrothermal actuators [22]. The gripper was designed with two initial opening of 50 μm and 100 μm, respectively (**Figure 1**). When the gripper structure is electro-thermally actuated the arms and the jaws will close and will be able to handgrip a micro-object. The total length of the gripper arms used to grasp an object is of 920 μm. The arms were designed with a width of 20 μm [22]. A metallic micro-heater is implanted between two SU-8 layers. The heater lines have a width of 10 μm and were designed first, to be fabricated using Cr/Au/Cr materials and second, to be fabricated using only the gold. Usually, a chromium thin layer or other adhesion layers are used to improve the connection between the gold metal and the polymer. On the other hand, it was reported that the deposition of the SU-8 polymer over the gold metal do not need an adhesion layer [23].

The optimized design consists of symmetrically disposed of three material layers. A metallic layer for the heater is implanted between two SU-8 based structure layers having the same thickness, as described previously [18–22]. The thicknesses of the Cr/Au/Cr films were 10 nm/300 nm/10 nm. The thickness of the gold layer is 100–300 nm. For each SU-8 layer we obtained a thickness of 9 μm. The details of the fabrication process where using the Cr/Au/Cr films have been reported also previously in [21] and when using only gold in [24] but for other gripper designs.

The proposed microgripper in this work was designed symmetrically with encapsulated metallic micro-heaters in the structural material of the grippers, the SU-8 polymer, in order to reduce the undesirable out-of-plane displacement of the gripper, to obtain the electrical isolation of the heaters and to reduce the mechanical stress that can occur in the structure [22].

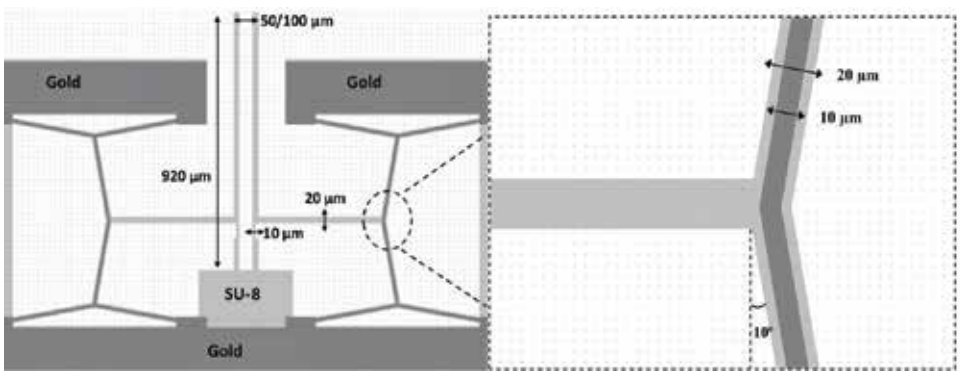

Figure 1. Schematic design of the SU-8 microgripper [22].

3. Finite element simulation

In order to check the performance of the microgripper, finite element simulations were performed. The microgripper with the initial opening of 50 μm was numerically investigated.

Coupled electro-thermo-mechanical simulations were completed using the MemMech simulator from the Coventorware 2014 software tool. A simplified 3D microgripper model (**Figure 2**) was meshed using hexahedral elements (Extruded bricks). The number of volume elements was optimized choosing the proper size of the mesh elements using the Split and Merge algorithm. The thicknesses of the SU-8 layers and the gold layer are 18 μm and 300 nm, respectively.

The materials properties and the surface boundary conditions were set for the simulations (**Table 1**). The initial temperature of the whole structure and the temperature of the environment were considered to be $T_0 = 27°C$, with respect to the Coventorware settings requirements for such kind of analyses. The radiation losses from the device are negligible in comparison with the heat loss by convection to the surrounding media [4], since the maximum temperature reached in the microgripper, in order to operate, is lower than 800°C. The air convection coefficient was set to 250 W/m^2 K [4].

The Young's modulus of the SU-8 was measured with the nanoindentation technique and was set in simulations for a value of 4.6 GPa (**Figure 3**). The indentation tests have been carried out using A G200 Nano Indenter from Agilent Technologies (Keysight Technologies).

The thermal coefficient of expansion was fixed at 52 (ppm/°C) and the thermal conductivity at 2 X 10^5 pW/μmK. For the gold layer we used a Young's modulus of 77 GPa reported for thin films.

The TCR, temperature coefficient of resistance, was measured for the Cr/Au/Cr thin films and obtained the value 0.001569/°C. This value is significantly smaller than the value of 0.0034–0.0037/°C used for the bulk gold material. For the thin gold film the TCR was measured at 0.00314/°C.

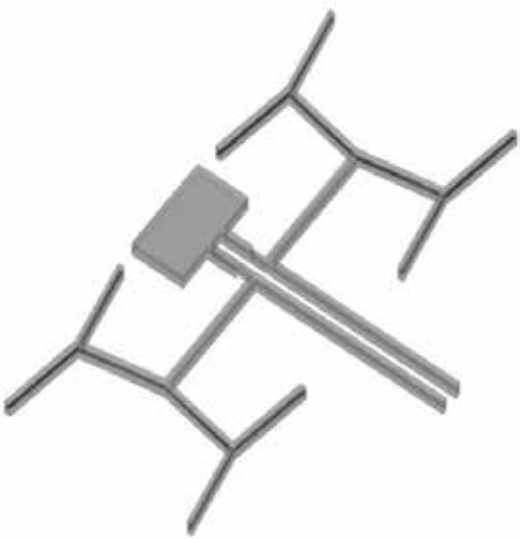

Figure 2. The simplified 3D model of the microgripper with encapsulated heaters in SU-8 polymer: The layers sandwich structure used in FEM simulations (Coventorware 2014) [22].

Property	SU-8	Au
Young's Modulus (E) [GPa]	4.6	77
Poisson ratio (ν)	0.22	0.35
TCE Coeff. of Thermal Expansion (α) [1/K]	52×10^{-6}	14.1×10^{-6} (300 K)
Thermal Conductivity (λ) [pW/(μm·K)]	0.2×10^{6}	297×10^{6}
Softening point [°C]	210	
SpecificHeat(pJ/kgK)	1.2×10^{15}	12.87×10^{15}
TCR [/°C]	—	0.001569
Electric Cond. [pS/μm]		Conf. Eq. (1) and (2)

Table 1. The materials properties used in simulations.

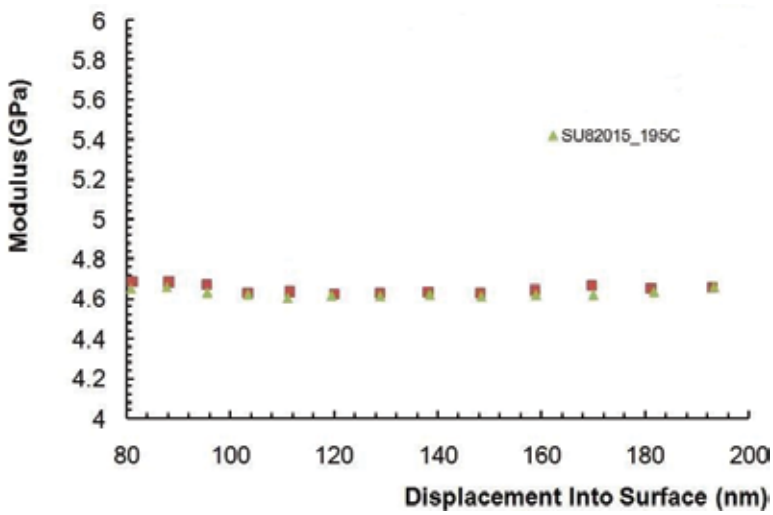

Figure 3. Young's modulus vs displacement into surface of SU-8 layer.

Electrical conductivity of the gold layer was set as function of the temperature using the Eqs. (1) and (2):

$$\rho(T) = \rho_0 \left[1 + \varepsilon \left(T - T_0\right)\right] \tag{1}$$

$$\sigma(T) = 1/\rho(T) \tag{2}$$

where $\rho(T)$ is the resistivity as function of the temperature, ρ_0 is the resistivity at T_0, ε is the TCR of the gold and σ is the electrical conductivity.

The simulation results regarding the temperatures distribution reached in the microgripper when it is actuated were visually compared with the thermal measurements realized using an IR camera SC5000 from FLIR system (**Figure 4**). The thermal measurements show that the distribution of the temperatures in the microgripper has a similar map with the simulation results. The temperature values at the tips remains near initial temperature of the environment.

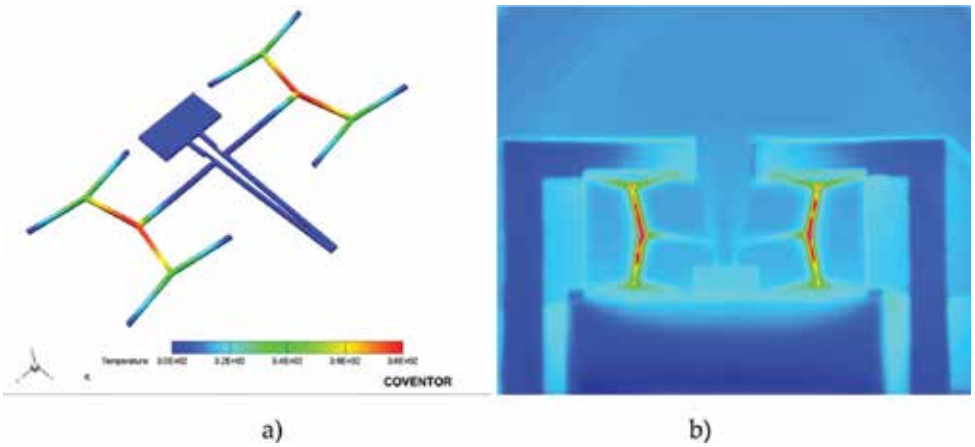

Figure 4. Simulations and thermal measurements results: (a) FEM coupled electro-thermo-mechanical simulations results of the temperatures distribution in the microgripper at 22 mA (Coventorware 2014 simulation) [22]; (b) the radiation distribution in the microgripper (IR thermography measurements).

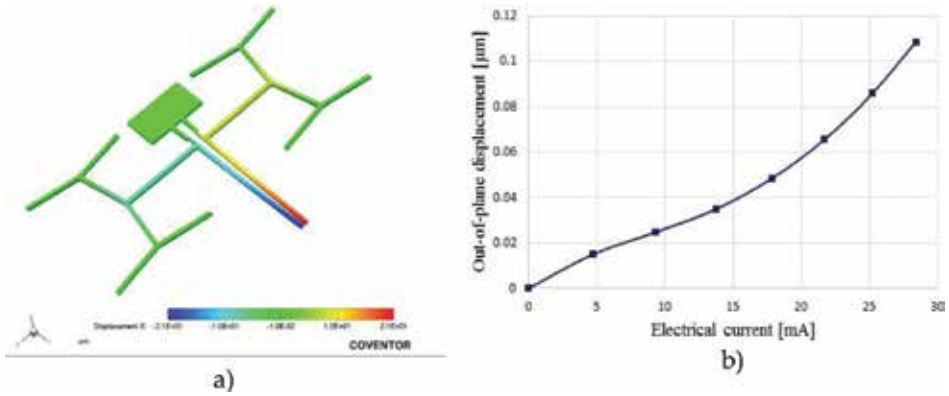

Figure 5. FEM coupled electro-thermo-mechanical simulations results: (a) the in-plane deflections at 22 mA [22]; (b) the out-of-plane displacements of the tips vs. electrical current (Coventorware 2014 simulation).

The simulated in-plane and the out-of-plane deflections of the microgripper tips were presented in order to evaluate the opening and the displacements of the gripper arms (**Figure 5**). The simulation results demonstrate that the tips deflect no more than 0.12 μm in the out-of-plane direction (**Figure 5(b)**).

The simulation results show that the gripper can work up to a temperature of 165°C for a complete closing tips. The gripper can continue to work up to 205°C in order to obtain a higher displacement or a higher pressure on the griped micro-object. The results indicate that the polymeric micromanipulators can work at low operation temperatures of the tips and with high in plane displacement. A displacement of 25 μm for each microgripper polymeric arm was obtained at a temperature value of 165°C and for a current value of 25 mA. At the tips the temperatures remain of 30–35°C close to the settings performed for the initial temperature of the media. The capable manipulating size range of the simulated microgripper is from 1 to 50 μm. If

we consider the microgripper with 100 μm the initial opening then the manipulating size is from 50 to 90 μm. A temperature change with only 5°C is observed at the microgripper tips.

4. Fabrication and characterization

The fabrication of the microgrippers is based on a three mask process. The OmniCoat stripper (MicroChem) is used in order to completely release the final structures [21–24].

4.1. First fabrication process

A silicon wafer of any orientation was used after a typical chemical cleaning. A thin layer of 40 nm thickness of Omnicoat was deposited on the silicon wafer by spin-coating and baked at 200°C on a hotplate for 1 minute. Then the SU-8 2015 (MicroChem) polymer was deposited on the wafer using a spinner at 4000 rpm in order to obtain a thickness of 9 μm. The wafer was soft-baked at 65°C and at 95°C for 1 minute and 3 minutes, respectively. The SU-8 layer was then patterned using the first mask in order to obtain the microgripper configuration. After the exposure, the wafer was post-baked at 65°C and at 95°C for 1 minute and 2 minutes, respectively and then developed using mr-Dev 600 developer. The polymer structure was hard-baked at 185°C for 15 minutes in order to complete cross-linking of the SU-8 polymer. The metal layer consists of a sandwich of Cr/Au/Cr films of 10 nm/300 nm/10 nm thicknesses. The metals were evaporated and the heater and pads were obtained using a lift-off process based on AZ4562 photoresist. The second SU-8 2015 layer was obtained using the same settings as for the first layer. In this step the access to the metallic pads was created using the third mask for SU-8. The final thermal process of the polymer in this step was the hard-baking at 195°C for 30 minutes for cross-linking of the SU-8 polymer. To release the microgripper structures the Omnicoat layer was developed (**Figure 6**). The SU-8 and the metallic layers are well patterned (**Figure 7**). **Figure 8** (a) shows an optical picture of the fabricated microgripper before releasing.

4.2. Second fabrication process

A thin layer of Omnicoat was deposited on a silicon wafer by spin-coating as in the first fabrication process. The SU-8 polymer was deposited on the wafer using a spinner in order to

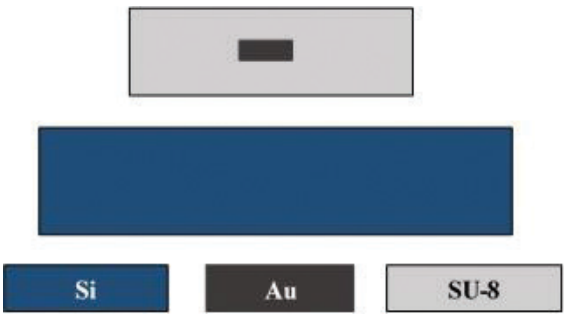

Figure 6. Schematic cross section of the actuator arm after fabrication and release.

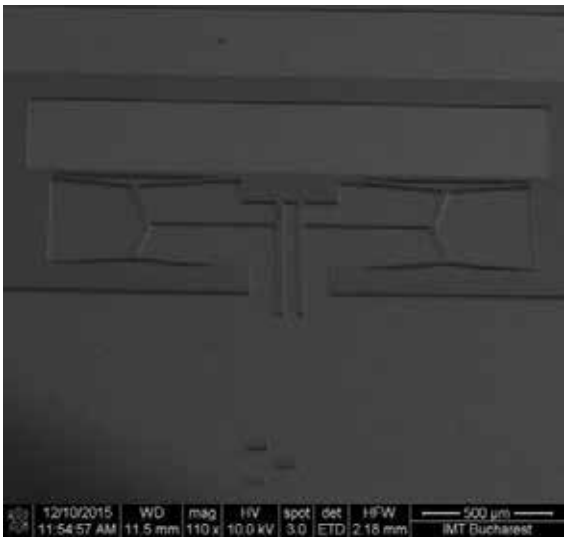

Figure 7. SEM image of the fabricated microgripper using the Cr/au/Cr films for the heater.

obtain a thickness of ~10 μm. The wafer was soft-baked in the same conditions and the SU-8 layer was then exposed using the first mask. After the exposure, the wafer was post-baked and then developed. The polymer structure was hard-baked in order to complete cross-linking of the SU-8 polymer. The heaters and the pads were obtained using a lift-off process based on AZ4562 photoresist. An O_2 plasma treatment was performed for a couple of seconds in order to clean and increase the adhesion of the substrate [24]. Then, a metal layer of a gold thin film with 300 nm thickness was evaporated on the wafer. The second SU-8 layer was obtained using the same conditions as for the first layer. In this step the access to the metallic pads was created using the third mask for SU-8. The final thermal process of the polymer in this step was the hard-baking at 195°C for 30 minutes for cross-linking of the SU-8 polymer. To release the microgripper structures the Omnicoat layer was developed. **Figure 8** (b) shows an optical picture of the released fabricated microgripper. A released chip with 4 structures is presented in **Figure 8** (c).

5. Experimental testing

In order to validate the model, the experiments were performed in air. For the tests we used the microgrippers with 50 μm the initial opening. Each structure was fixed manually on a silicon substrate (**Figure 9**) and the electrical contacts were placed directly on the metallic pads.

The dimensions of the microheaters were measured using a miscroscope. The TCR (temperature coefficient of resistance) measurements were carried out using a small chamber where the microgripper were fixed one a hotplate [21, 25]. A thermocouple based temperature sensor was used. Then, the heater resistance was measured at different temperatures. Based on the

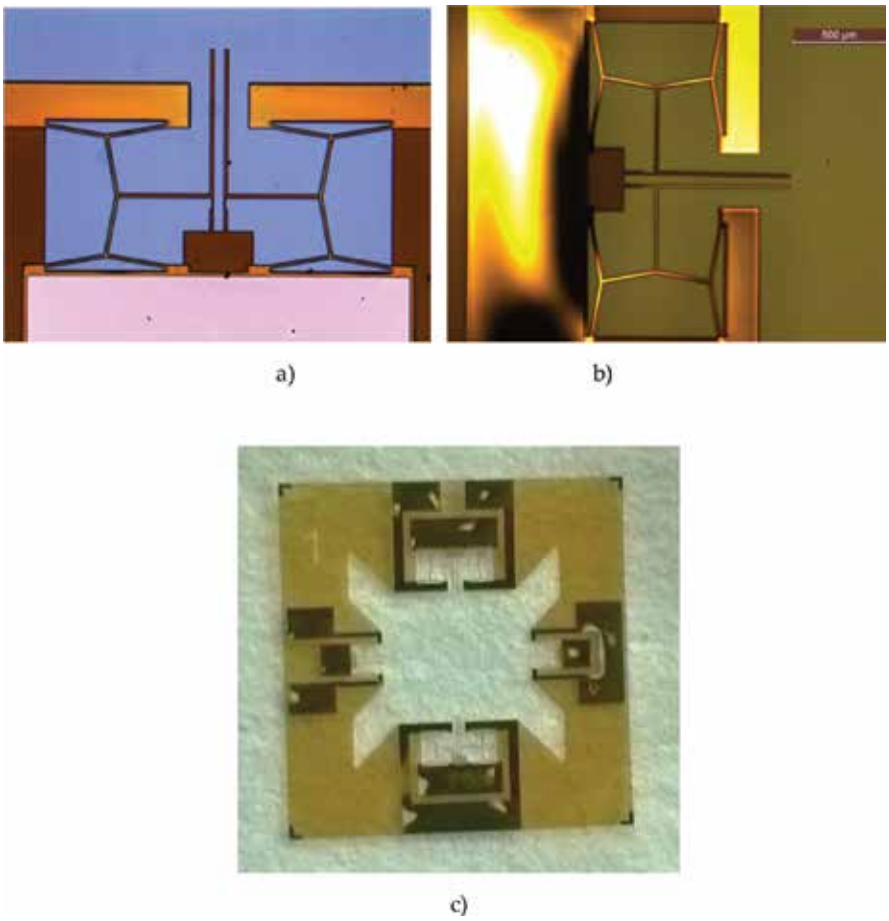

Figure 8. Optical microscope picture of the fabricated electrothermal SU-8 microgripper: (a) the microgripper with Cr/au/Cr films [22]; (b) the fabricated microgripper using the gold film for the heater; (c) a released chip with 4 structures with au film used for the heater.

values of the line equation parameters which fit the resistance graphs, the TCR was determined for each microgripper. For the Cr/Au/Cr thin films microgrippers the measured TCR is 0.001569/°C. For the thin gold film microgripper the TCR was found to be 0.00314/°C using the same microgripper configuration. We notice that for the gold microgripper the measured TCR value is very close to the bulk gold values which are between 0.0034 and 0.0037/°C, while for the Cr/Au/Cr thin films microgrippers the measured TCR is half of the bulk value.

These measured TCR values were used to determine the heater temperatures when the microgripper is actuated.

The in-plane deflection change with drive current was observed with an optical microscope and a camera with the associated viewing software. For each actuation step, the displacements of the gripper tips were measured using the optical images. **Figure 10** shows the first and the last stage of the opening-closing tips of the microgripper, while the **Figure 11** proves a good

agreement between the simulation results and the measured openings and the temperatures of the microgripper arms. The out-of-plane displacement was not observed in the experiments while the simulation results provided an out-of-plane displacement less than 100 nm. Currents larger than 27–28 mA make the SU-8 softer and the device will be damaged due to the increased temperature over 210°C.

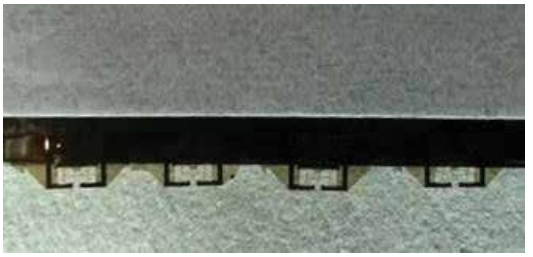

Figure 9. The fixed structures on a silicon substrate for experiments tests.

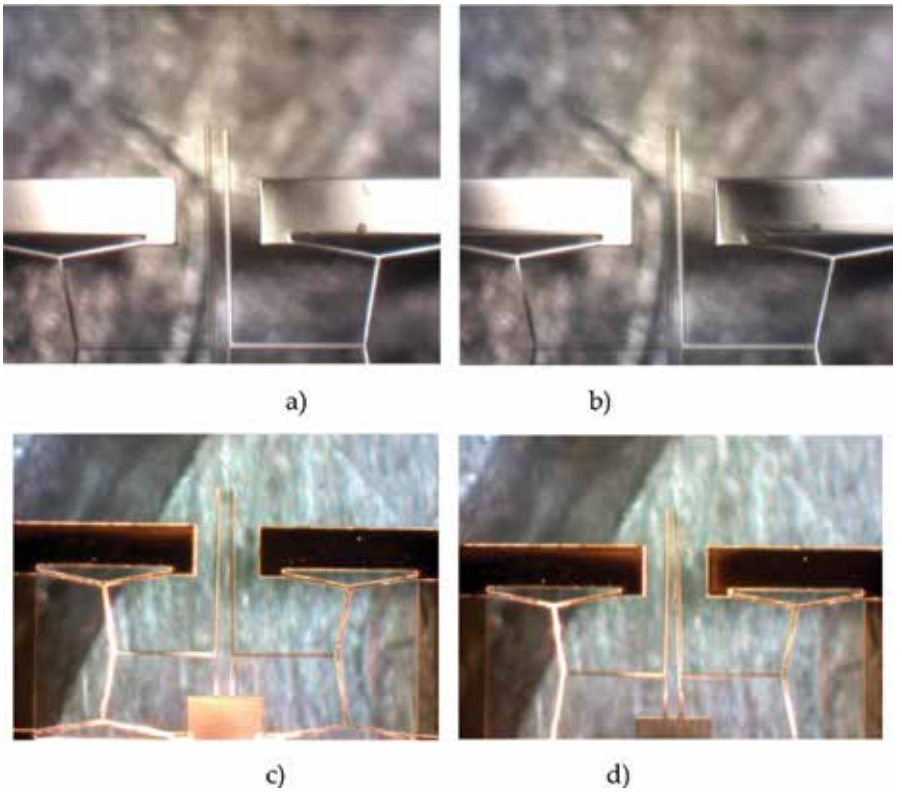

Figure 10. Optical images of the actuated microgrippers with the tips in the open and close stage: (a) the initial stage of the microgripper tips with Cr/au/Cr films used for the heater and with the initial opening of 50 μm [22]; (b) closing tips stage at 24 mA for the microgripper with Cr/au/Cr films used for the heater [22]; (c) the initial stage of the microgripper tips with au film used for the heater and with the initial opening of 50 μm; (b) closing tips stage at 24 mA for the microgripper with au film used for the heater;

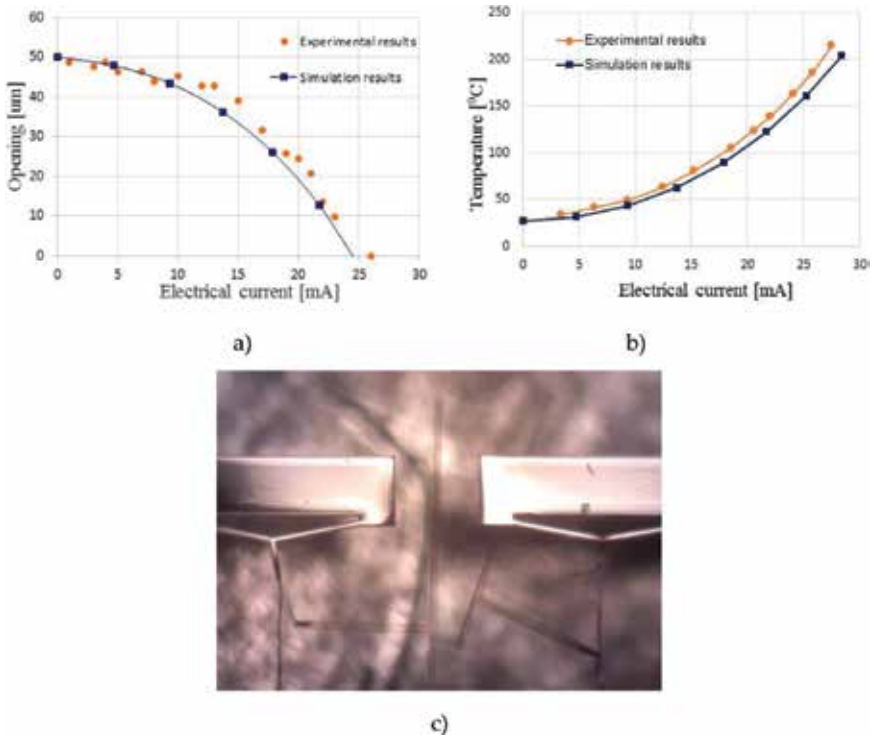

Figure 11. Experimental and simulation results: (a) measurements and simulation results of the jaw displacement versus electrical current; (b) measurements and simulation results of the maximal values of the temperatures in the microgripper versus electrical current; (c) optical image of the damaged SU-8 microgripper at 28 mA [22].

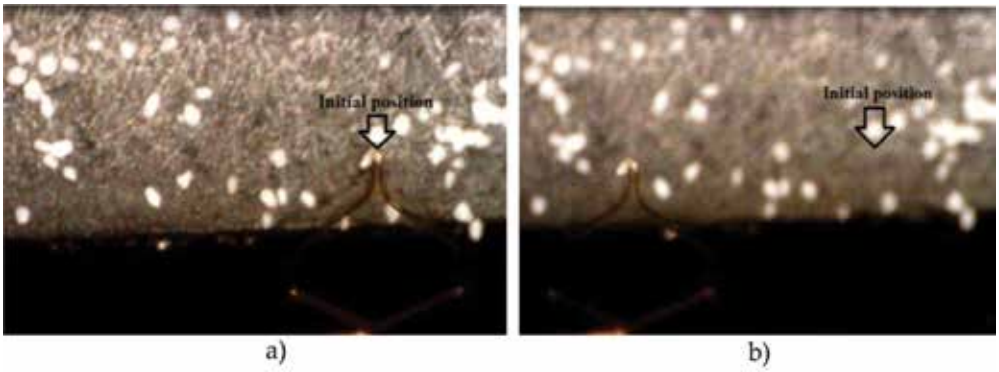

Figure 12. Optical images of an SU-8 microgripper manipulating a polymeric micro-object: (a) gripping the object; (b) placing the object in the final position.

In order to demonstrate the microgripper capability, different micro-elements were used in order to pick and place and manipulate them with the gripper arms of a similar SU-8 fabricated microgripper (**Figure 12**).

6. Conclusions

In this paper, a complete work regarding an SU-8 electro thermally actuated microgripper based one a cascaded V-shaped configuration was presented. The gripper were designed, fabricated and investigated experimentally and numerically. Two kind of fabrication were presented, using only a gold thin layer for the heater avoiding the deposition of an adhesion metal, like chromium and using Cr/Au/Cr films for the heaters. The optimized design consists of three material layers symmetrically disposed. The metallic layer for the heater is implanted between two SU-8 based structure layers with the same thickness. From numerical simulation, the out-of-plane displacement of the tips was found to be always lower than 100 nm during the operation process.

Therefore, the fabrication processes can be used in the fabrication of different SU-8 based MEMS devices actuated electrothermally with the in-plane deflection.

The results show that the microgripper can work in air in his maximal stage for an electrical current up to 25–26 mA and a temperature up to 165°C. A 50 μm jaw gap can be obtained for 24–25 mA. The temperature of the microgripper SU-8 tip remains below 35°C. Our experimental and the simulation results demonstrate that our microgripper fulfills the design requirements having a thickness of less than 20 μm and the out-of-plane displacement almost eliminated.

A comparison between the simulations results and the measurements was presented regarding the displacements/opening of the arms and the maximal temperatures reached in the structure. The simulation results are in good agreement with the measurements.

Over 26–28 mA the device is damaged due to the SU-8 transformations over the glass transition temperature reached in the structure.

Acknowledgements

This work was supported by a grant of the Romanian National Authority for Scientific Research and Innovation, CCCDI – UEFISCDI, project number 22/2016, within PNCDI III, ERA-MANUNET-II-Robogrip project "Microgrippers as end-effectors with integrated sensors for microrobotic applications (ROBOGRIP)" (2016-2017).

Thanks

I thank to Muaiyd H. Al-Zandi and C. Wang (Heriot-Watt University, Edinburgh) for the help with the electrical measurements, to R. Muller for the support, to C. Tibeica for the discussions and electrical measurements, to R. Gavrila for the nanoindentation measurements and to D. Varsescu for the thermal measurements.

Author details

Rodica-Cristina Voicu

Address all correspondence to: rodica.voicu@imt.ro

National Institute for Research and Development in Microtechnologies-IMT Bucharest, Romania

References

[1] Jia Y, Xu Q. MEMS microgripper actuators and sensors: The state-of-the-art survey. Recent Patents on Mechanical Engineering. 2013;**6**(2)

[2] Que L et al. Bent-beam electrothermal actuators. Part I: Single beam and cascaded devices. Journal of Microelectromechanical Systems. 2001;**10**:247-254

[3] Shen X, Chen X. Mechanical performance of a cascaded V-shaped Electrothermal actuator. International Journal of Advanced Robotic Systems. 2013;**10**:379

[4] Colinjivadi KS, Lee J-B, Draper R. Viable cell handling with high aspect ratio polymer chopstick gripper mounted on a precision manipulator. Microsystem Technologies. 2008; **14**:1627-1633

[5] Nguyen N, Ho S, Low C. A polymeric microgripper with integrated thermal actuators. Journal of Micromechanics and Microengineering. 2004;**14**(7):969-974

[6] Kim K et al. Metallic microgripper with SU-8 adaptor as end-effectors for heterogeneous micro/nano assembly applications. Microsystem Technologies. 2004;**10**(10):689-693

[7] Hamedi M et al. Design, analysis and fabrication of silicon microfixture with electrothermal microclamp cell. Microelectronic Engineering. 2013;**111**:160-165

[8] Wang Z, Shen X, Chen X. Design, modeling, and characterization of a MEMS electrothermal microgripper. Microsystem Technologies. 2015;**21**(11):2307-2314

[9] Voskerician G et al. Biocompatibility and biofouling of MEMS drug delivery devices. Biomaterials. 2003;**24**:1959-1967

[10] Somà A et al. Design and building up of an electro thermally actuated cell microgripper Proc. Recent Advances in Mechanical Engineering and Mechanics. 2014:125-130

[11] Chu Duc T et al. Electrothermal microgripper with large jaw displacement and integrated force sensors. Journal of Microelectromechanical Systems. 2008;**17**(6):1546-1555

[12] Solano B, Wood D. Design and testing of a polymeric microgripper for cell manipulation. Microelectronic Engineering. 2007;**84**(5–8):1219-1222

[13] Zhang W et al. A polymer V-shaped elctrothermal actuator array for biological applications. Journal of Micromechanics and Microengineering. 2008;**18**:075020

[14] Zhang R et al. A multipurpose electrothermal microgripper for biological micromanipulation. Microsystem Technologies. 2012;**19**(1):89-97

[15] MicroChem, SU-8 2000 Permanent Epoxy Negative Photoresist [Online] http://www.microchem.com/ [Accessed: 12-12-2017]

[16] Lorenz H et al. SU-8: A low-cost negative resist for MEMS. Journal of Micromechanics and Microengineering. 1997;**7**(3):121-124

[17] Chu J, Zhang R, Chen Z. A novel SU-8 electrothermal microgripper based on the type synthesis of the kinematic chain method and the stiffness matrix method. Journal of Micromechanics and Microengineering. 2011;**21**:054030 (15pp)

[18] Voicu R et al. Method for overcoming the unwanted displacements of an electrothermally actuated microgripper. In: Proc. Conf. 4M October; 2007. pp. 39-42

[19] Voicu R, Műller R. New electro-thermally actuated micromanipulator with optimized design and FEM simulations analyses In: Proc. Conf. Design, Test, Integration & Packaging of MEMS/MOEMS (DTIP); 2013. pp. 1-6

[20] Voicu R, Műller R. Design and FEM analysis of a new micromachined electro-thermally actuated micromanipulator. Analog Integrated Circuits and Signal Processing. 2013;**78**(2): 313-321

[21] Al-Zandi MH, Voicu R-C, Muller R, Wang C. Testing and characterisation of Electrothermal Microgrippers with embedded Microheaters. In: Proc. Conf. Design, Test, Integration & Packaging of MEMS/MOEMS. Budapest: DTIP; 2016. pp. 256-260

[22] Voicu R-C. Design, numerical simulation and experimental investigation of an SU-8 microgripper based on the cascaded V-shaped electrothermal actuators. Journal of Physics: Conference Series (JPCS). 2016;**757**(1):012015. DOI: 10.1088/1742-6596/757/1/012015

[23] Solano B. A microgripper for single cell manipulation [thesis], Durham University; 2008

[24] Voicu R-C, Tibeica C, Müller R, Dinescu A. An SU-8 micro-tweezer based on the chevron electro-thermal actuators with a large in-plane displacement. In: Proc. of IEEE International Semiconductor Conference CAS 2017, 11–14 October, Sinaia. 2017. pp. 105-108

[25] Al-Zandi MH, Wang C, Voicu R-C, Müller R. Measurement and characterisation of displacement and temperature of polymer based Electrothermal Microgrippers. Microsystem Technologies. 2017. DOI: 10.1007/s00542-017-3298-8

Chapter 3

Ionic Polymer Actuators: Principle, Fabrication and Applications

Yanjie Wang and Takushi Sugino

Additional information is available at the end of the chapter

http://dx.doi.org/10.5772/intechopen.75085

Abstract

Ionic-polymer based actuators have the advantages of low voltage and power requirements, being easily processable, flexibility, soft action and bio-mimetic activation, which are of considerable interests for applications in biomedical micro-devices and soft robotics. In this chapter, we firstly review the development of ionic polymer actuator and reveal the universal architecture and mechanism of ionic polymer actuators. We then introduce two kinds of typical polymer actuators: ionic polymer-metal composites (IPMC) and bucky gel actuator (BGA), including their basic principle, fabrication process and typical applications. The aim of this chapter is to give some perspectives on IPMC and BGA and provide a way and case in using this actuator for real applications.

Keywords: electroactive polymer, ionic polymer, actuator, carbon nanotube, ionic liquid

1. Introduction

Recently, as one typical electroactive polymers (EAP), ionic polymer actuators have gradually grown into an important smart material, which is mainly composed of the interlayer for mass transfer and conductive layers on both sides similar to the sandwich structure. When applied an electric field, local stress occurs due to the migration of ions bonded solvent molecules toward the electrode layers, which causes one side to swell and another side to shrink, resulting in bending deformation as shown in **Figure 1**. Due to large bending deformation by low driven voltage, much attention has been focused on ionic polymer actuators [1–3].

The origin of ionic polymer actuators can be traced back to the 1990s of last century. Adolf et al. [4] and Oguro et al. [5] introduced the initial prototype patent of ionic polymer actuators

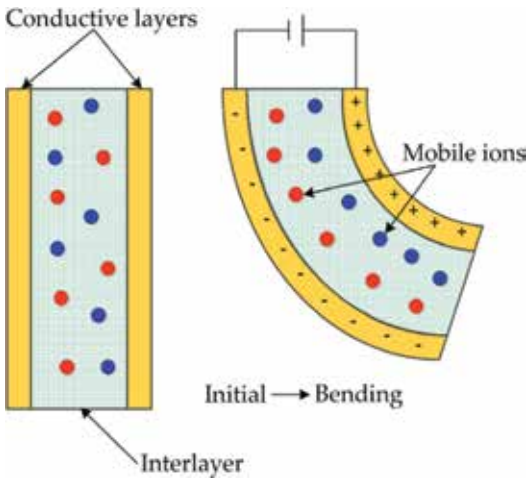

Figure 1. Universal architecture and mechanism of ionic polymer actuators.

in early stage. They both claimed that an actuator comprises an ion exchange membrane and a pair of electrodes attached to opposite surfaces of the ionic polymer, which refers to the cation or anion exchange membrane. Adolf et al. even named the actuator electrically controlled polymeric gel actuators, which maybe is the first normal name of ionic polymer actuator. After that, many researchers were attributed themselves to explore the essential properties of this actuator. They give different names to this special actuator based on different understandings, such as ionic polymeric gel actuator [6], electrically controllable artificial muscle [7], ion-exchange membrane metal composites [8], Nafion-Pt composite actuators (ICPF) [9] and ionic polymer-metal composites (IPMC) [10], which is the most common names so far. At this stage, it is dominant to clarify the actuating mechanism of this kind of actuator. So several electromechanical and physical models were gradually developed by de Gennes et al. [11], Newbury and Leo [12, 13], Nemat-Nasser et al. [14], Tadokoro et al. [9], Zicai Zhu et al. [15, 16] and so on. Meanwhile, for this ionic polymer actuator, the ionomer layer and conductive layer are critical components. The substitutes of components are an important way to improve the electromechanical performance of the actuator. Generally, perfluorinated polymers, such as Nafion (sulfonated) or Flemion (carboxylated), are employed as ionomer layer. The actuation ability of the ionic polymer actuator seriously is dependent on fixed anions, mobile cations and nanochannels inside Nafion or Flemion. Based on this property, a lot of novel hydrocarbon ion-exchangeable membranes are introduced to replace the ionomer layer [2]. These membranes include commercial products, blending and synthetics, some of which overcome the back-reversal problem and show much larger bending deformation compared to the Nafion- or Flemion-IPMC, such as poly(styrene-alt-maleimide) (PSMI)-incorporated poly(vinylidene fluoride) (PVDF) and chitosan/polyaniline interpenetrating polymer network. Likewise, the electrode layer plays an important role in IPMC actuation. It is considered to be easier to modify the electrode layer to optimize the IPMC property than the ionomer layer. Of all metals, gold and platinum with excellent conductivity and chemical stability are the most widely used electrode materials. Because of high cost, inexpensive electrode materials are still in need to replace gold and platinum. Palladium [17], silver [18] or their complex [19] has been considered as substitute.

With the development of new conductive materials, non-metallic materials, such as polyaniline (PANI), carbon nanotube (CNT) and grapheme etc., are also introduced as electrode materials of the actuator. On this basis, Fukushima et al. [20] proposed a novel kind of fully plastic actuator fabricated by layer-by-layer casting with ionic liquid based bucky gel, which also named bucky-gel actuator (BGA). The bucky-gel actuators composed of the conductive layers of the CNT blending ionic liquid and PVdF(HFP) and the interlayer made of the ionic liquid and PVdF(HFP). In contrast with IPMC, the fabrication process includes neither deposition of metallic layers nor actuating ion exchange. And the bucky-gel actuator can operates stably and quickly in air without back-reversal deformation under DC voltage.

In this chapter, we try to give an overview of two kinds of typical polymer actuators: ionic polymer- metal composites (IPMC) and bucky gel actuator (BGA), including their basic principle, fabrication process and typical applications. We put some results of previous works into more general perspective as well and provide insights of how these results have to be considered for the implementation of future applications. The study and development of polymer actuators are unfolding. This is no doubt that ionic actuators will show great potentials as alternatives for use in the application of precision micro-actuating technology in the future.

2. Principle

As we all know that charged particles will have a directional migration effect when put in the electric field. Generally, parallel plate capacitors would create a uniform electric field between the plates. Special dielectric is added into capacitor, which has unique property with solid–liquid two-phase microstructure. Charged particles (such as cations) do not exist alone in solution environment, and they tend to bind to a certain amount of solvent molecules forming solvated cations. Charged particles together with solvent molecules travel through the liquid-phase microstructure of dielectric from one side to another side when voltage is applied to the plates. This will result in mass plentiful on one side and exhausted on the other side. At this point, mechanical local strain will occur on both sides. These constitute the basic principle of ion polymer actuators.

2.1. Composition

As mentioned in Section 1, normally, an IPMC consists of an ionomer membrane plated on both sides with metal electrodes and neutralized with the necessary amount of mobile ions and fixed counterions. Metal electrodes form the outermost layers, followed by the intermediate layer. The intermediate layer comprises of metal particles dispersed inside the polymer matrix, which contains the ionomer, the counter ions and solvent molecules inside the membrane as shown in **Figure 2**. Nafion by DuPont or Flemion by Asahi Glass are most used as ionomer. The differences between them are in the functional groups (sulfonate and carboxylate groups respective) and ion-exchange capacities. The chemical structure of Nafion and Flemion are shown in **Figure 2(a)**. The commonly used cations inside the membrane include the alkali metal cations, such as Li, Na, K, Rb and Cs while the solvent mainly refer to water and ionic liquid [21, 22]. For electrode layer, due to their corrosion resistance and high conductivity, platinum and gold are

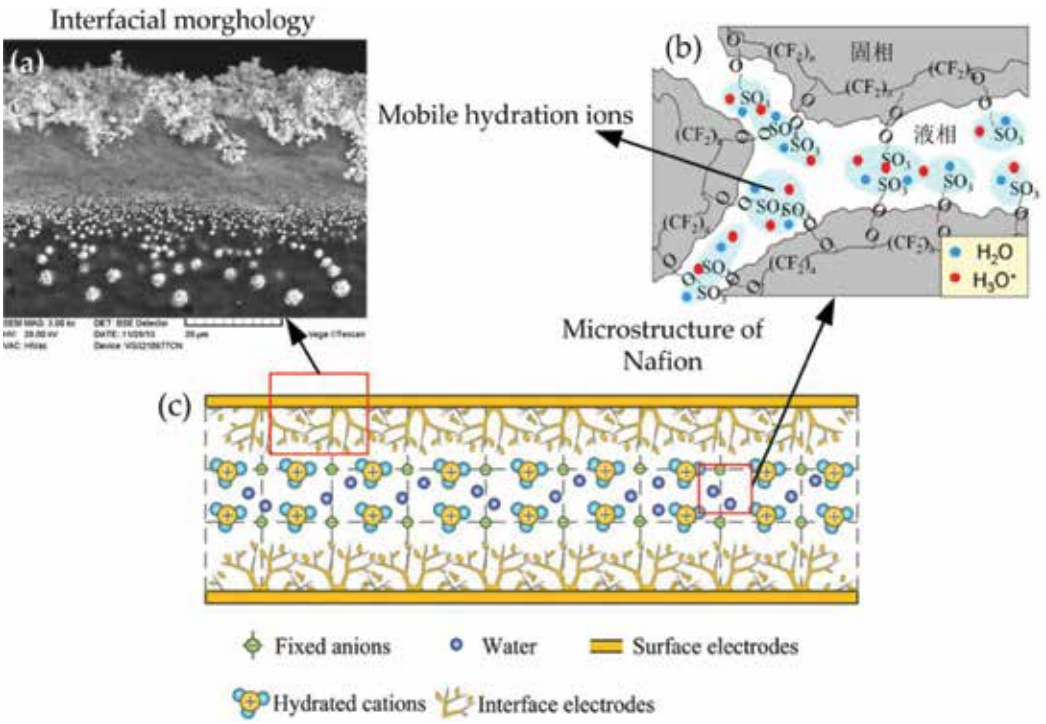

Figure 2. Pd typed IPMC: (a) electrode interfacial morphology; (b) microstructure of Nafion; (c) schematic diagram of composition.

commonly used [1, 23]. In our lab, we developed palladium typed IPMC because of its relative low price and optimized its preparation process [17, 24].

Bucky gel actuators (BGAs) are composed by carbon nanotubes (CNTs), ionic liquid (IL), and base polymer (BP). Single-walled CNT (SWCNT) is one of good nanocarbons as conductive electrode material. Not only imidazolium-type ILs but also ammonium-type ILs can be used as electrolyte source. Polyvinylidene fluoride-co-hexafluoropropylene (PVDF-HFP) is used as a BP. BGAs have a three-layered structure as shown in **Figure 3**, that is, one electrolyte layer is laminated by two electrode layers. A gel like self-standing electrolyte film is made with IL and BP. Generally, the electrode films are made from CNTs, IL, and BP. Some additives such as conductive or non-conductive nanoparticles can be added in the electrode layers in order to tune the electrochemical and mechanical properties of electrode [25, 26].

In contrast to IPMC and BGA, we can see that they both have very similar structures, with the exception of the ingredient of the electrode layer and interlayer, separately. This, of course, will finally result in the difference in preparation process and electromechanical performance.

2.2. Bending mechanism

The working mechanism of IPMC can be explained through electromechanical transduction. When applying an electric field, the cations inside the base membrane move toward

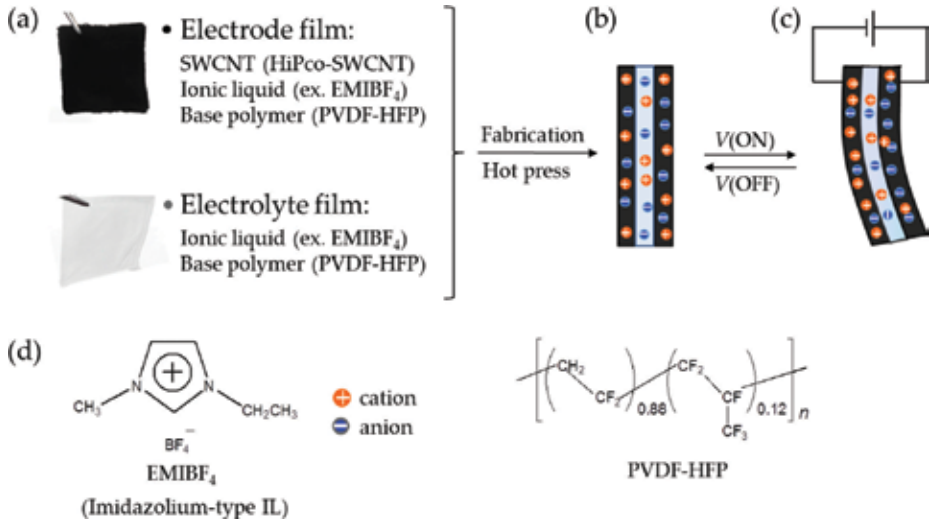

Figure 3. Components of electrode film and electrolyte film of bucky gel actuator (BGA) (a) Schematic representation of three-layered BGA (b) and the bending motion to the anode side (c) Chemical structure of imidazolium-type IL (EMIBF4) and base polymer (PVDF-HFP) (d).

the cathode with water molecules. The asymmetric distributions of the concentration of cations and water cause the IPMCs to swell near the cathode and generates extensional stress in the polymer, which causes the IPMC to swell near the cathode and shrink beside the anode. Finally, a bending motion is generated toward the anode [11]. Likewise, when an external stimuli was applied to the IPMC, the distributions of ions and water molecules inside IPMCs changes. Potential difference appears on both sides of the IPMC, which could be viewed as sensing signal. The properties of sensing and actuating of IPMC depend on the types of cation and solvent, surface resistant, interface morphology and temperature and humidity, etc.

In general, the current is generated by ion transport in BGAs and the three-layered BGAs show a bending motion to the anode side when voltages are applied. The electric charge is stored capacitively in BGAs during applying voltages [25]. This implies that our BGA is a capacitor. Baughman et al. reported SWCNT sheets (bucky papers) show the expansion and contraction (actuation) in aqueous electrolyte solution against a counter electrode [27]. They proposed the actuation mechanism in which C-C bond distance in SWCNT changes by charge injection originated from quantum and double-layer electrostatic effects. On the other hands, we consider the actuation mechanism of BGAs is due to C-C bond distance changing in CNTs [27, 28], volume change of the electrodes by sorption/desorption of ions [29], and electrostatic effect in the electrical double-layer [30]. Kiyohara and Asaka theoretically investigated the actuation mechanism of BGAs by a method of Monte Carlo simulation [31, 32]. We also studied the actuation mechanism of BGAs by a combination of symmetrical analysis, elasticity theory, and experimental results in the bulk scale [33]. As a result, it was found that the cathode expands and the anode contracts resulting in the bending motion of BGAs to the anode side.

3. Fabrication methods

3.1. IPMC

The current IPMC preparation technique involves two distinct steps: initial pretreatment, impregnation–reduction (IR) and chemical deposition. In our lab, we improve the technique by combining impregnation electroplating (IEP) [19]. The detailed process is as follows:

1) Nafion 117 was used as the interlayer roughened by sandblasting process. The diameter size of powders 200# is 0.0750 mm and the sandblasting time is 30 s. 2) Immerse the pre-treated Nafion in a 160 mL ammonia solution of [Pd (NH3)4]Cl2 with 140 mg Pd and 20 mL ammonia of 25% for 2 h with low-speed stirring. Then soak the pre-exchanged Nafion with the Pd complex cations in an alkaline solution of $NaBH_4$ (2–5%, PH > 13) under an ultrasonic environment at a continuous raising temperature (i.e. from 30 to 50°C). Repeat the first two steps for 3 times. 3) The pretreated Nafion membrane was soaked in Pd complex solution again for over 2 h and then placed in the apparatus to electroplate for over 30 s for both sides. Repeat the third step for 3 times. Immerse the IPMC in an aqueous solution of NaOH (0.1–0.5 mol/L) for 2 h.

3.2. BGA

A typical preparation method to fabricate BGAs is described below. The electrode film was obtained from SWCNT (HiPco–SWCNT, purified grade), PVDF-HFP (Kynar Flex®2801), and 1-ethyl-3-methylimidazolium tetrafluoroborate (EMIBF4) as an ionic liquid. 20 wt% of SWCNT, 32 wt% of PVDF-HFP, and 48 wt% of EMIBF4 were dissolved into 9 mL of N, N-dimethylacetamide (DMAC) and stirred for more than 1 day at room temperature, then sonicated for 24 hours in an ultrasonic bath. A gelatinous black solution was obtained after sonication. Obtained gelatinous solution was cast into a Teflon mold (25 × 25 mm^2) and dried on a hotplate at 50°C for 12 hours and dried DMAC furthermore at 80°C in vacuo for 3 days. As a result, a black self-standing electrode film was obtained. The electrolyte film was obtained from similar procedure. 50 wt% of PVDF-HFP and 50 wt% of EMIBF4 were mixed into the solvent mixture of 4-methyl-2-pentanone and propylene carbonate anhydrous and cast into the mold. The solvents were dried on a hot-plate then an opaque self-standing gel electrolyte was obtained. One electrolyte film was sandwiched by two electrode films with a hot-pressing technique to obtain the three-layered BGA. Super-growth SWCNT is also good nanocarbon for the electrode of BGAs [34]. The more detail fabrication process is described elsewhere [25, 26].

4. Electromechanical responses

To evaluate the effect of parameters, the responses of IPMC, mainly including current and deformation, are measured in fully hydrated state. The performances of strip sample were tested for comparison. **Figure 4** shows the testing schematic. The strip sample with 40 mm in length and 5 mm in width is clamped by two copper disks. The displacement at the point 25 mm away from the fixed point is measured by a laser displacement sensor (Keyence, LK-G80). The applied voltage and current are simultaneously measured. The tip displacement w of samples can be calculated from the measured displacement δ by the following Eq. (1).

$$w = 2R\sin^2\left(\frac{l}{2R}\right), \tag{1}$$

where l is the length of the free part of IPMC strip. The radius of curvature R is evaluated from the measured displacement by the following Eq. (2).

$$\frac{1}{R} = 2\delta/(d^2 + \delta^2) \tag{2}$$

where d is the distance between the measuring point and the fixed point.

The currents and deformations under DC voltage were measured more than 20 s. The voltage range was set from 0.5 to 1.7 V with an interval of 0.3 V. For the electrochemical system composed of water, palladium, Nafion, and Na + cations, the electrolytic voltage of water is 1.75 V even higher [35]. So the voltages higher than 1.7 V were not employed in order to avoid the electrolysis process of water. To facilitate the analysis, the averages and errors of the peak currents and maximum deformations of the samples, testing three times for each sample, were extracted and recorded as shown in **Figure 5**. It can be observed that the peak currents increase with the applied voltage increasing (**Figure 5(a)**). Under the voltage of 2 V, the current response fluctuates in some degree due to the electrolysis of water. From **Figure 5(b)**, the maximum displacements of sample exhibit significant differences. With the applied voltages in an increase, the maximum displacements are increased.

To further investigate the relationship between the electrode morphologies, physical and electrical parameters and the electromechanical responses, an electrical component is introduced to explain the deformation behavior of IPMC as shown in **Figure 6**.

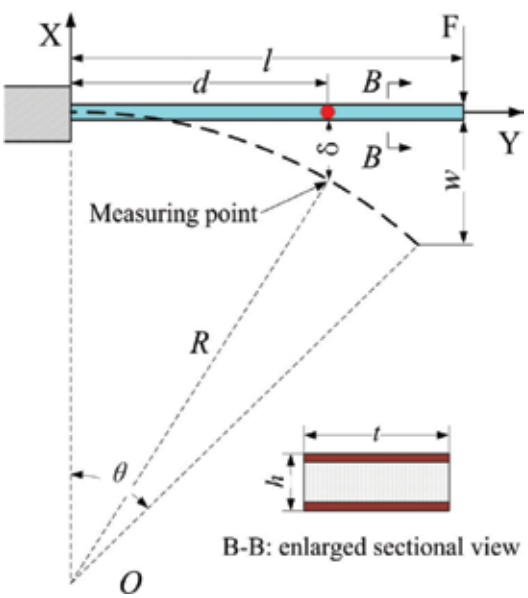

Figure 4. Schematic of the bending deformation.

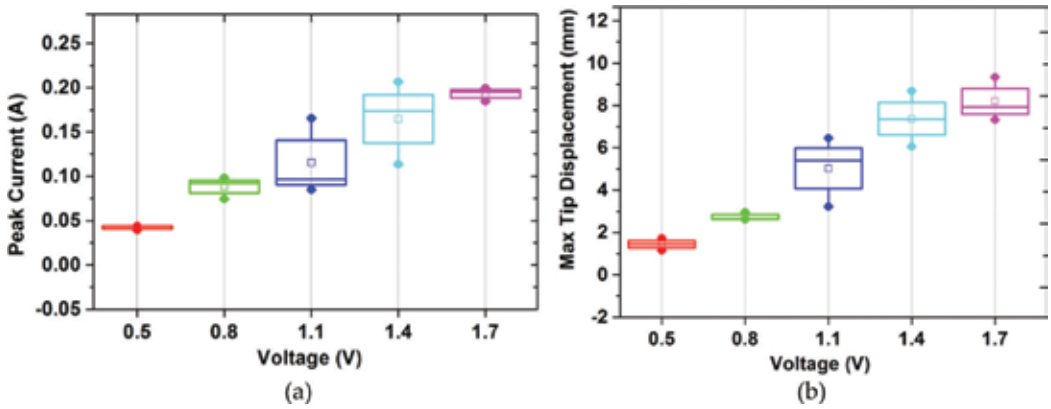

Figure 5. (a). Peak current of IPMC strip under different voltage; (b) Maximum displacements of samples versus voltages.

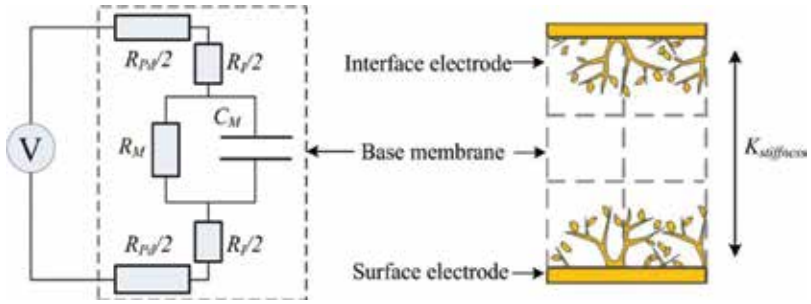

Figure 6. Equivalent circuit of IPMC.

The interlayer of IPMC can be viewed as an ion conductive material and modeled by a capacitor and a resistor in parallel. The electrode can be modeled by two resistors. Then the peak current i_{peak} (total current) can be figured out by Eq. (3). The first item of the Eq. (3) describes the steady-state current from the resistance components, while the second item reflects the transient current from the capacitive element. Eq. (4) shows the qualitative relations between deformation, peak current and bending stiffness based on experimental test.

$$\mathrm{i}_{peak} = \frac{U}{R_{Pd} + R_m} + \frac{\varepsilon S_1}{4kd} \cdot \frac{dU}{dt}, \tag{3}$$

$$\mathrm{D} \sim \frac{i_{peak}}{K_{stiffness}}, \tag{4}$$

where U, R_{Pd}, S_1, D and $K_{stiffness}$ represent applied voltage, surface resistance, area of interface electrode, deformation and bending stiffness, respectively. Other parameters, such as R_m, ε, π, k and d, are considered to be constants.

It shows that the peak current depends on the electrode resistance, surface resistance, membrane resistance and the area of interface electrode closely related to dielectric modulus under

the condition of constant voltage. Eq. (3) and (4) can be employed to interpret the deformation behaviors of IPMC. From the perspective of the fabrication process, different fabrication process will exert an important effect on the surface resistances of the samples. Roughening increases the surface resistance while chemical plating can reduce it. Meanwhile, the decrease of surface resistance largely increases the bending stiffness. Although the bending stiffness does not contribute to peak current directly, it is also a key factor to affect the deformation of IPMC as shown in Eq. (3). So it is necessary to optimize the roughening process and chemical plating process. The impregnation-reduction process mainly forms a penetration electrode to increase the area of interface electrode. But it is difficult to further improve the interface due to the blocking effect of previous plated layer.

As we described before, the capacitive current is generated in BGAs during applying voltages. This means that the electrolyte (ionic liquid (IL)) plays a very important role for the actuation of BGAs. So, we studied the influence of ILs on the actuation mechanism of BGAs. We investigated the electrochemical and electromechanical properties of BGAs by using seven kinds of ILs [36]. The chemical structures of ILs are shown in **Table 1**. Some physicochemical properties, such as melting point (T_{mp}), viscosity (η) at 25° C, and electric conductivity (κ) are also summarized in **Table 1**, especially for imidazolium-type ILs [37]. We measured the displacement of bending by a laser displacement meter at different frequencies of applied voltages in order to investigate actuation properties of BGAs. The three-layered BGA sample (normally, the actuator sample has a size of 1 (width) x 10 mm (length)) was clipped by two gold current collectors to apply voltages. Then, alternative voltages were applied to actuator sample. A Potentio/Galvanostat with a wave generator was used to apply voltages. The voltage, current, and displacement were simultaneously monitored by an oscilloscope. The detail experimental setup is described elsewhere [25, 38].

Ionic liquid		Cation		Anion	T_{mp} (°C)	η (cP) at 25 °C	κ (mS cm^{-1})
Imidazolium type IL	$EMIBF_4$	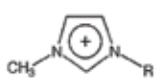	R= C_2H_5	BF_4^-	14.6	31.8	13.6
	$BMIBF_4$		R= C_4H_9		−71	118.3	3.43
	$HMIBF_4$		R= C_6H_{13}		−82	223.8	1.04
	$OMIBF_4$		R= C_8H_{17}		−80	422.0	0.576
	EMITFSI			$(CF_3SO_2)_2N^-$	−16	28.0	8.40
Ammonium type IL	A−3	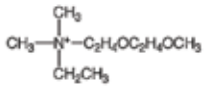		BF_4^-			
	A−4			$(CF_3SO_2)_2N^-$			

Table 1. Chemical structure and physicochemical property of IL [37].

The observed displacement (δ) was converted to the strain difference (ε) between the two electrodes of BGAs in order to normalize the size differences of BGAs by using the following equation on the assumption that there is no distortion of the cross-sections in the actuator during bending.

$$\varepsilon = 2D\delta/(L2 + \delta 2) \tag{5}$$

where D is the thickness of actuator sample and L is the free length of actuator sample from the fixed end of gold current collectors.

The frequency dependence of strain (ε) for BGAs including seven kinds of ILs is shown in **Figure 7**. The BGA with EMIBF4 as an electrolyte shows the best actuation (strain) in all the frequency range. The strain becomes worse with increasing the length of alkyl chain in the imidazolium-cation. This is the reason why the ionic conductivity decreases with increasing the length of alkyl chain related to increasing the viscosity. The frequency dependence of strain can be successfully fit to an electrochemical kinetic model (a double-layer charging kinetic model). In this model, the electrode of BGA is fully charged at low frequencies of applied voltage. However, there is not enough time to be fully charged for the electrode at higher frequencies. In other words, the stored charge (Q) decreases with increasing the frequencies of applied voltage. In this consideration, the strain (ε) is proportional to the stored charge (Q). A simple equivalent circuit model was used to make the electrochemical kinetic model as shown in **Figure 8**. The double-layer capacitance of each electrode ($C1$) is replaced by the capacitance (C); C = C1/2. R is resistance of ionic gel electrolyte. R is calculated from the ionic conductivity κ (=thickness/R × area). The stored charge $Q(f)$ at a frequency (f Hz) is represented by the following equation:

$$Q(f)/Q0 = 1 - 4CRf\left(1 - \exp\left(-1/4CRf\right)\right) \tag{6}$$

where $Q0$ is the stored charge at a limit of low frequency. And the strain ($\varepsilon(f)$) is given by following equation:

$$\varepsilon(f) = \varepsilon 0Q(f)/Q0 \tag{7}$$

where $\varepsilon 0$ is the strain at a limit of low frequency.

The obtained parameters such as the double layer capacitance of the electrode (C), the ionic conductivity of the ionic gel electrolyte (κ), the calculated resistance of the ionic electrolyte (R), the strain at a limit of low frequency ($\varepsilon 0$), and the time constant (CR) are summarized in **Table 2**. Base on the equivalent circuit model analysis, it was found that the frequency dependence of actuation of BGAs is depended on the electrochemical time constant (CR) that is mainly related to the ionic conductivity. Furthermore, the actuation of BGAs is affected by the size difference between cation and anion included as an internal electrolyte because the volume changes of cathode and anode are caused by the sorption/desorption of cations and anions. More detail studies on the impedance analysis for the porous structure in the electrode of BGAs [39] and further studies on electrochemical energy and power density of BGAs [40] were reported by Randriamahazaka and Asaka et al. It was found that BGA behaves as supercapacitors and the electrochemical energy

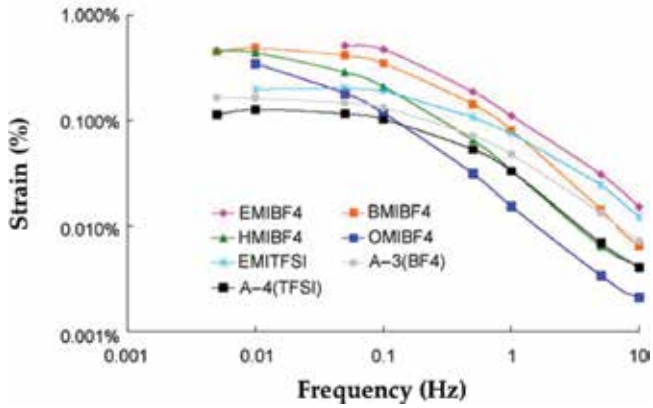

Figure 7. Frequency dependence of strain difference (e) for BGAs with seven kinds of ILs (reproduced with permission [36]).

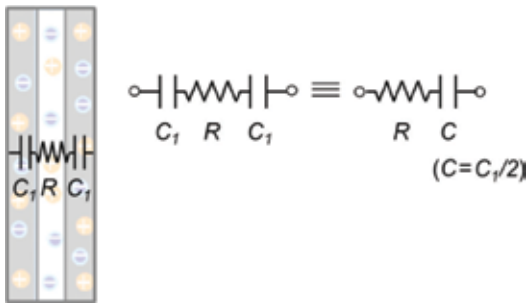

Figure 8. Equivalent circuit model of BGA.

Ionic liquid	C_{SWCNT} (F g^{-1})	C (F cm^{-2})	κ (mS cm^{-1})	R (Ω cm^2)	ε_0 (%)	CR (s)
$EMIBF_4$	45.5	0.0312	1.71	1.17	0.53	0.0365
$BMIBF_4$	45.3	0.0338	0.312	6.41	0.45	0.217
$HMIBF_4$	44.8	0.0286	0.134	14.9	0.48	0.426
$OMIBF_4$	44.6	0.0286	0.014	143	0.60	4.09
EMITFSI	49.2	0.0338	1.33	1.50	0.21	0.0507
A−3	35.4	0.0286	0.393	5.09	0.17	0.146
A−4	41.6	0.0286	0.729	2.74	0.13	0.0784

Table 2. Gravimetric capacitance of SWCNT(*C*SWCNT) and double-layer capacitance per electrode area (*C*) of BGA electrode, ionic conductivity (κ) and ionic resistance (*R*) of ionic gel electrolyte, strain difference at a limit of low frequency (ε0) and time constant (*CR*) (reproduced with permission [36]).

densities of BGAs are of the same order of magnitude as those of natural muscles. Similar ionic polymer actuators with carbonaceous electrodes are introduced in a review paper by Asaka et al. [41].

5. Typical applications

Ionic polymer actuators have been expected to be used for some practical applications such as active microcatheters, micropumps, tactile displays, biomimetic microrobots, and so on [42, 43]. First commercial production with ionic EAP was produced by a Japanese company (Eamex Co.) in 2002 ([42] p. 2). They produced a fish robot which has a caudal fin made with ionic EAP. They can control the movement of the caudal fin by electromagnetic induction (wireless control).

Here, we introduce three examples of our application trials with IPMC and BGAs.

First sample is the prototype of developed micropump using inner petal-shaped IPMC actuator as shown in **Figure 9**. Micropumps capable of providing an appropriate flow rate and a reasonable back pressure are usually inevitable requirements for a self-contained microfluidic system. Since this is a prototype only, the pump was not made to be very small. The overall size is 70 × 40 × 15 mm (length × width × height). The pump chamber is a 15 mm in diameter, 2 mm in depth. It should be noted that, we only tested inner petal-shaped IPMC actuator with a diameter of 15 mm. The actuator used in this prototype is a Nafion 117-based IPMC actuator. A pair of copper plates as electrodes was used to clamp the two sides of the IPMC actuator, providing the stimulus electrical signal. In order to evaluate the performance of micropump, we carry out the experiment of the flow rate and the back pressure measurement in 1 Hz sine voltage input by changing the voltage amplitude from 0.5 to 3 V by the interval of 0.5 V. The experimental results show that the flow rate from 162 to 1611 μL/min can be obtained by changing the voltage amplitude from 0.5 to 3 V, respectively. And the back pressure on the micropump can be as high as 71 mm-H2O under the condition of 1 Hz and 3 V sine voltage input.

Second example is an ultra-thin and ultra-light refreshable Braille display with BGAs [41, 44]. There are more than 100 million visually impaired people in the world. This means there are a huge number of people who cannot access the internet because most information in the internet are shown with words and photos on the liquid crystal displays of mobile phones, laptop computers, and other tablet tools. Currently, the refreshable Braille displays with inorganic piezoelectric actuators are commercially available but they are not suitable for the mobile use

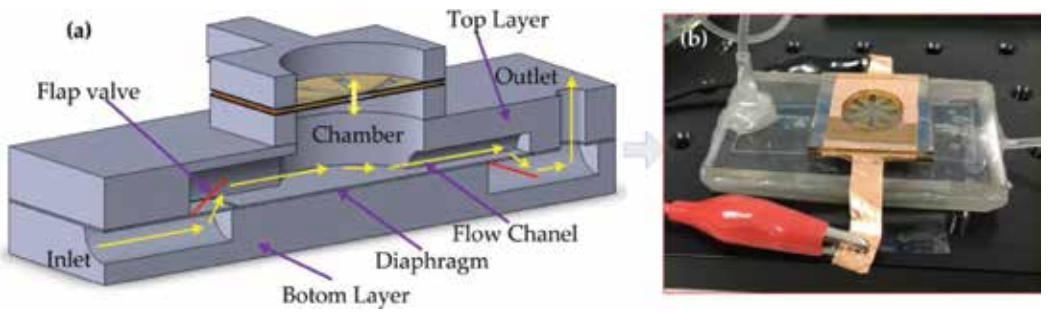

Figure 9. The principle (a) and appearance (b) of the fabricated micropump.

because they are heavy (~kg) and large (266 (length) × 129 (width) × 40 mm (thickness) for a 32 Braille characters display). So, we had a motivation to produce an ultra-light and ultra-thin Braille display by using BGAs. The developed prototype Braille display with BGAs is shown in **Figure 10** which has a size of 65 (length) × 30 (width) × 3 mm (thickness) with 6 refreshable Braille characters and the weight is only 5 g. This prototype Braille display was produce by collaborations with ALPS Electric Co., Ltd. Our Braille display was readable for most of visually impaired people but not readable for some visually impaired people who are not used to use Braille display. This is the reason why the dot force is not enough compared to commercial Braille displays. Improving the force and the durability is now in progress.

Third example is the application for micropipette and micropump. Recently, micropipettes and micropumps have been receiving a lot of attention for the microfluidic point-of-care (POC) diagnostic devices. So, we are willing to test the potential of BGAs as a micropipette. This project has been done by collaborations with Fraunhofer IPA (Stuttgart, Germany) [45]. A BGA (black square film) was set into the printed circuit boards (PCBs) to apply voltages as shown in **Figure 11**. The pipette has a channel tip which has a size of 1 × 1 × 10 mm to suck and release liquid. The BGA showed an up-and-down motion in the PCBs like a diaphragm pump and can dispense *ca*. 10–20 μL liquid. Furthermore, Goya et al. developed a BGA micropipette system equipped with commercially available two- and

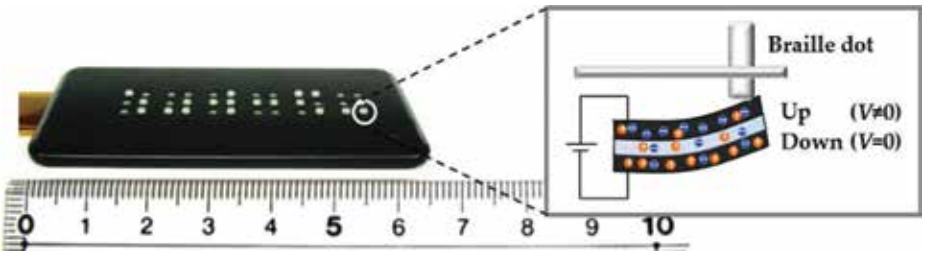

Figure 10. A photo of prototype braille display with BGAs and an illustration of movement of a braille dot by the bending of BGA.

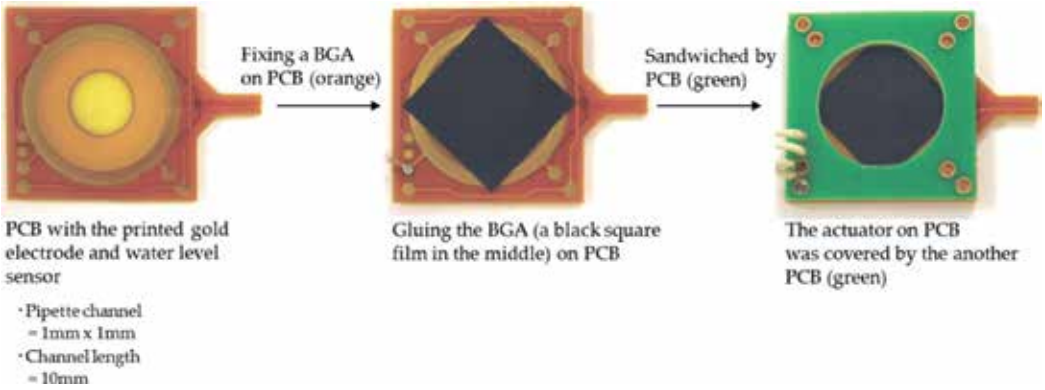

Figure 11. A photo of prototype micropipette with BGAs. A black square BGA are set between two PCBs.

three-way solenoid valves [46]. In this system, the three-way valve and a particular two-way valve are open during the BGA shows upward motion (during sucking water). They were successful to dispense *ca*. 20 μL water droplet within 2% of relative standard deviation. We hope that our BGAs will be practically appreciable for some medical and medical welfare devices in the near future.

6. Conclusions

Ionic polymer actuator is a class of functional polymers that has great potential for application in soft robotics and micro-devices. In this chapter, two representative ionic polymer actuators are introduced: IPMC and BGA. Some fundamental characteristics and properties of the ionic polymer actuator have been clarified, and some recent applications in the micro pump, braille display and micropipette of IPMC and BGA as soft actuators have been presented.

Acknowledgements

This work is supported by the National Natural Science Foundation of China (NO.51505369 and 91748124), Jiangsu Key Laboratory of Special Robot Technology (NO. 2017B21114), and the Fundamental Research Funds for the Central Universities, P.R. China. The authors gratefully acknowledge the supports. The author T. S. thank to Sendai R&D center of Alps Electric Co. Ltd., Keio University (Prof. Nakano) and University of Tokyo (Prof. Someya) for their collaborations in the Braille project (the grant from Ministry of Health, Labor and Welfare of Japan in 2009 FY and 2010 FY).

Note

The authors contributed equally to this work.

Author details

Yanjie Wang[1]* and Takushi Sugino[2]

*Address all correspondence to: yjwang@hhu.edu.cn

1 School of Mechanical and Electrical Engineering, HoHai University, Changzhou, China

2 Inorganic Functional Materials Research Institute, National Institute of Advanced Industrial Science and Technology (AIST), Ikeda, Osaka, Japan

References

[1] Tiwari R, Garcia E. The state of understanding of ionic polymer metal composite architecture: A review. Smart Materials and Structures. 2011;**20**(8):083001

[2] Jo C, Pugal D, Oh IK, et al. Recent advances in ionic polymer–metal composite actuators and their modeling and applications. Progress in Polymer Science. 2013;**38**(7):1037-1066

[3] Wang Y, Chen H, Liu J, et al. Aided manufacturing techniques and applications in optics and manipulation for ionic polymer-metal composites as soft sensors and actuators. Journal of Polymer Engineering. 2015;**35**(7):611-626

[4] Adolf D, Shahinpoor M, Segalman D, Witkowski W. Electrically Controlled Polymeric Gel Actuators, US Patent Number 5250167, October 1993

[5] Oguro K, Takenaka H, Kawami Y. Actuator Element. US Patent Office, US patent no. 5268082, Issued December 7, 1993

[6] Shahinpoor M. Continuum electromechanics of ionic polymeric gels as artificial muscles for robotic applications. Smart Materials and Structures. 1994;**3**(3):367

[7] Shahinpoor M. Micro-electro-mechanics of ionic polymeric gels as electrically controllable artificial muscles. Journal of Intelligent Material Systems and Structures. 1995; **6**(3):307-314

[8] Salehpoor K, Shahinpoor M, Mojarrad M. Linear and platform type robotic actuators made from ion-exchange membrane-metal composites. Proceedings of SPIE Smart Material Structure. 1997;**3040**:192-198

[9] Tadokoro S, Yamagami S, Takamori T, et al. Modeling of Nafion-Pt composite actuators (ICPF) by ionic motion[C]//smart structures and materials 2000: Electroactive polymer actuators and devices (EAPAD). International Society for Optics and Photonics. 2000; **3987**:92-103

[10] Shahinpoor M, Bar-Cohen Y, Simpson JO, et al. Ionic polymer-metal composites (IPMCs) as biomimetic sensors, actuators and artificial muscles-a review. Smart Materials and Structures. 1998;**7**(6):R15

[11] De Gennes PG, Okumura K, Shahinpoor M, et al. Mechanoelectric effects in ionic gels. EPL (Europhysics Letters). 2000;**50**(4):513

[12] Newbury KM, Leo DJ. Linear electromechanical model of ionic polymer transducers-part I: Model development. Journal of Intelligent Material Systems and Structures. 2003; **14**(6):333-342

[13] Newbury KM, Leo DJ. Linear electromechanical model of ionic polymer transducers-part II: Experimental validation. Journal of Intelligent Material Systems and Structures. 2003;**14**(6):343-357

[14] Nemat-Nasser S, Li JY. Electromechanical response of ionic polymer-metal composites. Journal of Applied Physics. 2000;**87**(7):3321-3331

[15] Zhu Z, Asaka K, Chang L, et al. Multiphysics of ionic polymer–metal composite actuator. Journal of Applied Physics. 2013;**114**(8) 084902

[16] Zhu Z, Wang Y, Liu Y, et al. Application-oriented simplification of actuation mechanism and physical model for ionic polymer-metal composites. Journal of Applied Physics. 2016;**120**(3) 034901

[17] Chang L, Chen H, Zhu Z, et al. Manufacturing process and electrode properties of palladium-electroded ionic polymer–metal composite. Smart Materials and Structures. 2012;**21**(6) 065018

[18] Chung CK, Fung PK, Hong YZ, et al. A novel fabrication of ionic polymer-metal composites (IPMC) actuator with silver nano-powders. Sensors and Actuators B: Chemical. 2006;**117**(2):367-375

[19] Wang Y, Liu J, Zhu Y, et al. Formation and characterization of dendritic interfacial electrodes inside an Ionomer. ACS Applied Materials & Interfaces. 2017;**9**(36):30258-30262

[20] Fukushima T, Asaka K, Kosaka A, et al. Fully plastic actuator through layer-by-layer casting with ionic-liquid-based Bucky gel. Angewandte Chemie International Edition. 2005;**44**(16):2410-2413

[21] Nemat-Nasser S, Wu Y. Comparative experimental study of ionic polymer–metal composites with different backbone ionomers and in various cation forms. Journal of Applied Physics. 2003;**93**(9):5255-5267

[22] Zhu Z, Chang L, Takagi K, et al. Water content criterion for relaxation deformation of Nafion based ionic polymer metal composites doped with alkali cations. Applied Physics Letters. 2014;**105**(5) 054103

[23] Wang Y, Chen H, Wang Y, et al. Effect of dehydration on the mechanical and physicochemical properties of gold-and palladium-ionomeric polymer-metal composite (IPMC) actuators. Electrochimica Acta. 2014;**129**:450-458

[24] Wang Y, Zhu Z, Liu J, et al. Effects of surface roughening of Nafion 117 on the mechanical and physicochemical properties of ionic polymer–metal composite (IPMC) actuators. Smart Materials and Structures. 2016;**25**(8) 085012

[25] Sugino T, Kiyohara K, Takeuchi I, Mukai K, Asaka K. Actuator properties of the complexes composed by carbon nanotube and ionic liquid: The effect of additives. Sensors and Actuators B. 2009;**141**:179-186. DOI: 10.1016/j.snb.2009.06.002

[26] Sugino T, Kiyohara K, Takeuchi I, Mukai K, Asaka K. Improving the actuating response of carbon anotube/ionic liquid composites by the addition of conductive nanoparticles. Carbon. 2011;**49**:3560-3570. DOI: 10.1016/j.carbon.2011.04.056

[27] Baughman RH, Cui C, Zakhidov AA, Iqbal Z, Barisci JN, Spinks GM, Wallace GG, Mazzordi A, Rossi DD, Rinzler AG, Jaschinski O, Roth S, Kertesz M. Carbon nanotube actuators. Science. 1999;**284**:1340-1344. DOI: 10.1126/science.284.5418.1340

[28] Chan CT, Kamitakahara WA, Ho KM. Charge-transfer effects in graphite intercalates: Ab initio calculations and neutron-diffraction experiment. Physical Review Letters. 1987; **58**:1528-1531. DOI: 10.1103/PhysRevLett.58.1528

[29] Hahn M, Barbieri O, Campana FP, Kötz R, Gallay R. Carbon based double layer capacitors with aprotic electrolyte solutions: The possible role of intercalation/insertion processes. Applied Physics A: Materials Science & Processing. 2006;**82**:633-638. DOI: 10.1007/s00339-005-3403-1

[30] Oren Y, Glatt I, Livnat A, Kafri O, Soffer A. The electrical double layer charge and associated dimensional changes of high surface area electrodes as detected by moire deflectometry. Journal of Electroanalytical Chemistry. 1985;**187**:59-71. DOI: 10.1016/0368-1874(85)85575-1

[31] Kiyohara K, Asaka K. Monte Carlo simulation of electrolytes in the constant voltage ensemble. The Journal of Chemical Physics. 2007;**126**:214704-214714. DOI: 10.1063/1.2736371

[32] Kiyohara K, Asaka K. Monte Carlo simulation of porous electrodes in the constant voltage ensemble. Journal of Physical Chemistry C. 2007;**111**:15903-15909. DOI: 10.1021/jp0736589

[33] Kiyohara K, Sugino T, Takeuchi I, Mukai K, Asaka K. Expansion and contraction of polymer electrodes under applied voltage. Journal of Applied Physics. 2009;**105**:063506-1-8 [Erratum: J Appl Phys 2009;105:119902-1] DOI: 10.1063/1.3078031 [Erratum: DOI: 10.1063/1.3141728]

[34] Hata K, Futaba DN, Mizuno K, Namai T, Yumura M, Iijima S. Water-assisted highly efficient synthesis of impurity-free single walled carbon nanotubes. Science. 2004;**306**:1362-1364. DOI: 10.1126/science.1104962

[35] Zoulias E, Varkaraki E, Lymberopoulos N, Christodoulou CN, Karagiorgis GN. A review on water electrolysis. TCJST. 2004;**4**(2):41-71

[36] Takeuchi I, Asaka K, Kiyohara K, Sugino T, Terasawa N, Mukai K, Fukushima T, Aida T. Electromechanical behavior of fully plastic actuators based on buckey gel containing various internal inonic liquids. Electrochimica Acta. 2009;**54**:1762-1768. DOI: 10.1016/j.electacta.2008.10.007

[37] Ohno H, editor. Ionic Liquid II: Marvelous Developments and Colorful Near Future. Japan: CMC; 2006. 299 p. ISBN: 4-88231-557-2

[38] Takeuchi I, Asaka K, Kiyohara K, Sugino T, Terasawa N, Mukai K, Shiraishi S. Electromechanical behavior of a fully plastic actuator based on dispersed nano-carbon/ionic-liquid-gel electrodes. Carbon. 2009;**47**:1373-1380. DOI: 10.1016/j.carbon.2009.01.029

[39] Takeuchi I, Asaka K, Kiyohara K, Sugino T, Mukai K, Randriamahazaka H. Electrochemical impedance spectroscopy and electromechanical behavior of bucky-gel actuators containing ionic liquids. Journal of Physical Chemistry C. 2010;**114**:14627-14634. DOI: 10.1021/jp1018185

[40] Randriamahazaka H, Asaka K. Electrochemical analysis by means of complex capacitance of bucky-gel actuators based on single-walled carbon nanotubes and an ionic liquid. Journal of Physical Chemistry C. 2010;**114**:17982-17988. DOI: 10.1021/jp106232s

[41] Asaka K, Mukai K, Sugino T, Kiyohara K. Ionic electroactive polymer actuators based on nano-carbon electrodes. Polymer International. 2013;**62**:1263-1270. DOI: 10.1002/pi.4562

[42] Bar-Cohen Y, editor. Electroactive Polymer (EAP) Actuators as Artificial Muscles: Reality, Potential, and Challenges. 2nd ed. Washington: SPIE; 2004. 765 p. DOI: 10.1117/3.547465

[43] Carpi F, Smela E, editors. Biomedical Applications of Electroactive Polymer Actuators. West Sussex: Wiley; 2009. 476 p. DOI: 10.1002/9780470744697

[44] Takahashi I, Takatsuka T, Abe M. Application of nano-carbon actuator to braille display. In: Asaka K, Okuzaki H, editors. Soft Actuators: Materials, Modeling, Applications, and Future Perspectives. Springer Japan: Springer; 2014. pp. 371-384. DOI: 10.1007/978-4-431-54767-9.ch27

[45] Addinall R. Sugino T, Neuhaus R, Kosidlo U, Tonner F, Glanz C, Kolaric I, Bauerhansl T, Asaka K. Integration of CNT-based actuators for bio-medical applications-example printed circuit board CNT actuator pipette. In: Proceedings of 2014 IEEE/ASME international conference on advanced intelligent mechatronics (AIM); 8-11 July 2014; Besacon. France: IEEE; 2014. p. 1436-1441

[46] Goya K, Fuchiwaki Y, Tanaka M, Addinall R, Ooie T, Sugino T, Asaka K. A micropipette system based on low driving voltage carbon nanotube actuator. Microsystem Technologies. 2017;**23**:2657-2661. DOI: 10.1007/s00542-016-2943-y

Chapter 4

Development of Resonators with Reversible Magnetostrictive Effect for Applications as Actuators and Energy Harvesters

Jerzy Kaleta, Rafał Mech and
Przemysław Wiewiórski

Additional information is available at the end of the chapter

http://dx.doi.org/10.5772/intechopen.78572

Abstract

This chapter presents the methodology of designing and testing wideband actuators and energy harvesters which can be treated as one device called a mechanical resonator. In order to obtain described effects, the magnetostriction phenomenon was used. This effect enables the construction of resonators in selected frequency bands, including the ultrasonic range. Cores made of giant magnetostrictive materials (GMM) were used for the construction. Considerable attention was given to composite cores to reduce the weight of pure Terfenol-D. The influence of the volume fraction of Terfenol-D powder, the size of its grains, and the direction of polarization on the value of magnetostriction in a wide frequency band were investigated. The magnetostriction of composite cores and solid Terfenol-D samples was also compared. The structure and the use of magnetostrictive cores containing a combination of NdFeB magnets and pure Terfenol-D are also presented. An important issue was also the development of our own methodology of magnetostriction testing, including the use of fiber optic sensors (Fiber Bragg Grating sensors, FBGs), Hall's sensors, and the original measuring system for magnetic field visualization (Magscanner). The chapter also discusses several own designs of actuators and energy harvesters, including shock harvester, resonant harvester, and energy transmission system.

Keywords: magnetomechanical cross-effect, smart magnetic materials, magnetostriction, Terfenol-D, magnetostrictive actuators, frequency response, energy harvesting, harvesters

1. Introduction

Materials called/classified as smart materials (SM) have already formed a large group of new construction materials. The phenomenon of smart materials is based on the fact that their main properties, expressed as a physical unit (i.e., mechanical field), depend on some other unit (i.e., magnetic, electric or temperature field). Therefore, in the description and application of these materials, cross effects are the crucial factor. A significant group of SM is materials that present their main application characteristics based on magnetic stimulation (smart magnetic materials, SMM). The following materials should be mentioned as the representatives of the group: magnetorheological, giant magnetostrictive and magnetoresistive, magnetocaloric, shape memory magnetically activated, etc. It means that the diverse properties of SMM—including, for example, viscosity, shape, stiffness, temperature, electric resistance, color—can be modified with use of magnetic stimulation. In this chapter, the possibilities of using one of SMM groups, namely giant magnetostrictive materials (GMM), are presented.

The following subjects are described in this chapter:

- Development of the concept of GMM actuators in terms of applications as a vibration exciter or active vibration damper.
- Application of the inverse magnetostriction effect (called Villari-effect) for energy harvesting devices
- Preparation methods of composite magnetostrictive rods: GMM composite (GMMc): as magnetic active cores
- Application of fiber Bragg gratings (FBG) technique in online measurement of the magnetostriction level in strong magnetic field environment
- Testing method of resonators cores using impact as energy harvesting power sources for the standard microcontroller dedicated to wireless nodes
- Construction of high-power actuator with a real-time PID magnetostrictive regulator to compensate self-thermal effect

2. Magnetostrictive mechanical resonators and their applications

The main goal described in this chapter is to develop a methodology for designing and testing broadband resonators. This methodology should offer a better understanding of both actuators and energy harvesters, including those working alternately as one device. One of the most important issues to solve is obtaining mechanical resonance in a wide frequency band, which would allow the use of resonators in any mechanical construction.

It turned out that one of the materials exhibiting the so-called giant magnetostriction effect is Terfenol-D [1, 2], which might be very useful in solving this particular issue. Thanks to its

unique properties, the material allows the conversion of magnetic field energy into mechanical energy, using a magnetostriction effect. The effect is reversible and allows the conversion of mechanical energy into magnetic energy using the Villari effect. Therefore, Terfenol-D is widely used in a variety of applications such as construction of actuators [3–5], sensors [6], and so-called energy harvesters [7].

Unfortunately, despite their numerous advantages, solid materials also have significant drawbacks, among which the most important ones are as follows: the presence of strong eddy currents as a result of cyclic loading at high frequency of work [8], and low tensile strength. In order to eliminate these drawbacks, researchers are trying to produce new materials, such as polymer composites containing powdered Terfenol-D [9–14].

2.1. Actuators based on Terfenol-D

The Department of Mechanics, Materials Science and Engineering has been associated with the area of magnetic SM since the early 1990s. The first research related to this type of materials was mainly related to liquids, especially magnetorheological fluids. However, in subsequent years, this interest became more and more widespread, and as a result, a few years later, a great deal of attention was also paid to other materials, including the so-called giant magnetostriction. As it was mentioned before, Terfenol-D is a representative of such materials. The first work related to the research on this material allowed the design and manufacturing of the actuator whose core was the solid Terfenol-D. **Figure 1** shows one of the earliest magnetostrictive actuators called "singing table" which was designed by the authors.

Although the actuator presented in **Figure 1** was used mainly as a demonstration object, it allowed to show how the magnetostriction phenomenon works in an accessible way. Based on this first construction, the actuator construction was improved and modified in such a way that it could serve as an executive element in a prototype research stand. A new type of actuator made it possible to damp the vibrations of the construction with the use of counter vibration. Thanks to this, the vibrating wave of the opposite phase was adjusted to the natural

Figure 1. Vibration exciter system (singing table) as the first step taken by the authors' team to magnetostrictive technology [15].

vibrations of the structure, which caused the damping of vibrations and ensured the stability of the entire structure. **Figure 2** presents the second type of a Terfenol-D-based actuator dedicated for dumping mechanical vibrations in a low-frequency band (50–1000 Hz) [15].

2.2. Reversible effect actuators selected for energy harvesting

Energy harvesting (EH), in primary sources known also as power harvesting or energy scavenging, is a set of methods allowing to generate electrical energy using surrounding sources, such as mechanical, thermal, solar and electromagnetic energy, salinity gradients, etc., for example, [7]. Generally, the goal is using sources commonly available in the environment (so called background energy) which are undesirable and usually are suppressed (e.g., noise, impact and mechanical vibration of devices and constructions, electromagnetic smog, frictional and combustion heat as well as heat obtained as a result of electric current flow and engine cooling) or commonly available (solar light, wave energy, salinity differences, biochemical processes in, e.g., plants) and also related to human biology (motion, body heat, etc.). Currently, it is assumed that EH can be an effective source of "cost-free" (apart from installation costs) power supply for low power devices (e.g., electronic devices, sensor systems). It is assumed that in the future vast harvester networks will also be used as large power energy sources.

Magnetostrictive harvesters and actuators are constructed using physical cross effects based on magneto-mechanical phenomena. It is assumed that even in terms of low power and efficiency (albo: in the case of low power and efficiency techniques) they can be a valuable source of power supply. In low-power techniques, it is assumed that harvesters work as typical power supplies that are connected by a wire to a microprocessor subsystem (μC) which after supplying power sends data wirelessly to a unit receiving and processing information according to its operation algorithm (program code).

The principle of EH is to create a new concept of voltage generators which will use cross effects including the magneto-mechanic one. The assumption is that even though EH using the magneto-mechanical effect can provide only small powers or efficiencies, they can become valuable sources of energy. Special attention has been paid to this issue for the last few years in the biggest research institutes all over the world, especially in the USA and quickly developing Asian countries. The energy harvesting concept together with the development of

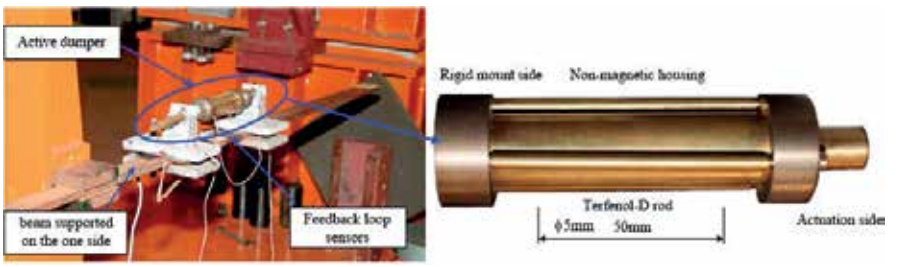

Figure 2. View of actuator as a part of the active dumping vibration system of calibrated mechanical beam [15].

energy recovering devices' (harvesters) development belongs to the field of alternative and renewable energy.

Taking into account the physical phenomena occurring during the energy exchange process, the construction and principles of work, and environmental conditions in a specified working area, harvesters (as sources with different electrical characteristics) can be divided into three groups:

- DC voltage harvesters (e.g., harvesters based on the thermoelectric effect),
- AC voltage harvesters (e.g., harvesters based on the Faraday effect or so called piezoelectric patches),
- Shock harvesters (e.g., harvesters with a magnetostrictive core).

In order to be able to design electrical circuits for harvesters, the knowledge of their working characteristics is mandatory. Only the ones based on the thermoelectric or photovoltaic effect can generate DC voltage. Those which regain energy from vibrations, magnetostrictive, piezoelectric or based on the Faraday effect are the sources of AC voltage. The scope of research related to energy harvesting conducted by the authors of the chapter is shown in **Figure 3**.

Harvesters supplied with energy from impacts [16] are a completely different type of devices. Electric energy generation lasts only for a very short period of time when it comes to the impulse power supply although its current amplitude is extremely high. Harvesters "supplied" with a mechanical shock generate various voltage outputs. However, they are considered devices characterized by strong current impulse and additional frequencies generated in

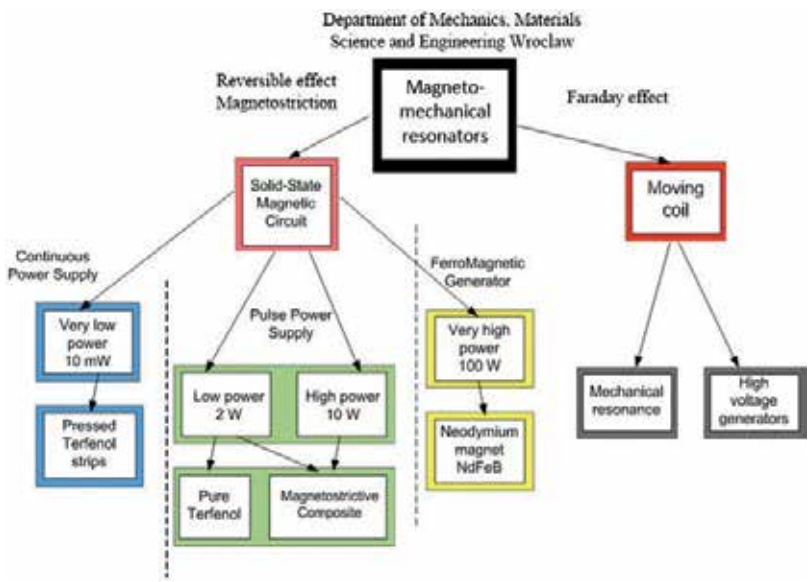

Figure 3. Structure of evaluating energy harvesting methods.

the signal which occur as a result of resonance in the core-coil system. In this chapter, a new method of electrical current generation due to the demagnetization of neodymium magnets in the circuits with magnetostrictive core is also presented.

Currently, a particular type of generators is harvesters from the explosive-driven ferromagnetic generators (EDFMG) group. They generate the electromagnetic wave that occurs due to the instant demagnetization of a magnet caused by a mechanical shock which results from an explosion or another strong force impulse. In this moment, the magnet loses its magnetic properties, generating a strong impulse magnetic field in its surroundings. During the impact, even the total destruction of a magnet is possible; however, the amount of energy that is generated on a coil is huge and it is sufficient to charge high-voltage capacitors with a substantial amount of electric energy.

The new concept of the harvester was developed based on the idea of a ferromagnetic generator (FMG) in which strong magneto-mechanical phenomena occur, including the demagnetization of strong neodymium NdFeB magnets in order to generate electric current due to a mechanical shock. One of the construction priorities was to standardize particular sizes and parts, so every single element of the harvester could be easily exchanged and disassembled. **Figure 4** presents the parts of the harvester.

It has to be remembered that the estimated efficiency value of the transformation between the mechanical shock, which occurs during the demagnetization of the neodymium magnets, and the electric current is about 0.2%. That is why, the main challenge is to improve power transformation. The so-called pulse power supply harvester constructions are shown in **Figure 5**.

2.3. Use of actuator-harvester circuits to power up wireless network system

Harvesters which in their principle of work use cross effects are more frequently based on magneto-mechanical phenomena. It is assumed that even in the case of low power and efficiency; they can be a valuable source of power supply.

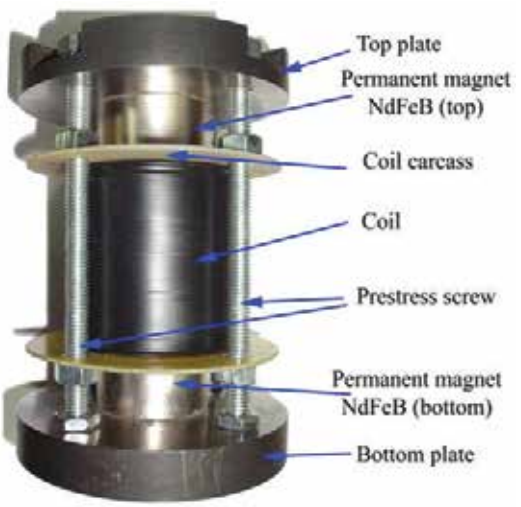

Figure 4. View of a shock harvester with description of its elements [16].

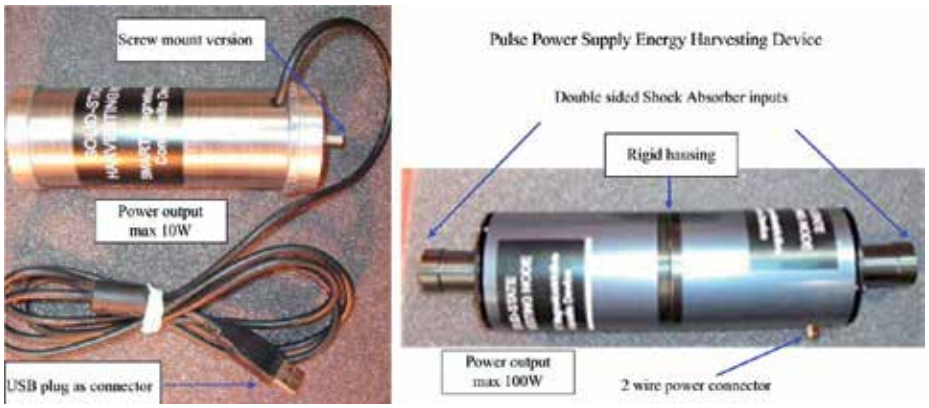

Figure 5. View of solid-state harvesters based on GMMc diameter of ϕ=5 mm (left) and ϕ=10 mm rod (right) for tactical grade versions of 10 W devices.

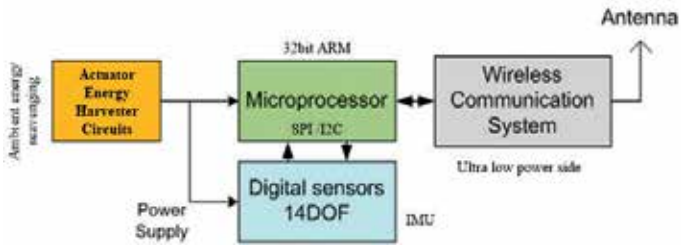

Figure 6. The structure of a wireless harvesting system with a 14 DOF block [17].

A multinode harvesting structure can be used in structural health monitoring (SHM) applications to recover electric power from wasted energy generated mostly from vibrations. Magnetic harvesters might also be used as a power source in SHM systems which monitor large mechanical structures. Our latest system presents this solution. It uses 14 MEMS sensors with designated 14 degrees of freedom (DOF) (3D accelerometer, 3D gyroscope, 3D magnetometer, barometric pressure sensor, microphone, temperature T, humidity R, light intensity). The structure of the system is shown in **Figure 6**. The software designed by the authors allows to monitor the parameters provided by 14 sensors via a webpage or in a service mode. The software is designed to support such systems as an ADIS16488 module and other components of the most precise IMU (Analog Devices iMEMS 2016). In order to process the data received from the 14 DOF sensors, which includes not only measuring the certain physical value but also monitoring the level of recovered energy, proper microprocessors had to be chosen (an important factor here is power consumption).

Figure 7 shows three typical sources of low-frequency energy harvesting: mechanical shock wave (**Figure 7A**), low-frequency mechanical resonance (**Figure 7B**) and energy transmission through ultrasonic resonant vibrations (**Figure 7C**). A properly selected conditioning circuit provides the harvesting system with useful current and voltage capabilities. The creation of a wireless node to measure certain physical quantities and to monitor the level of recovered energy requires the selection of an appropriate hardware platform, such as a microprocessor and a wireless transmission system. The use of SM in wireless power transmission turned out

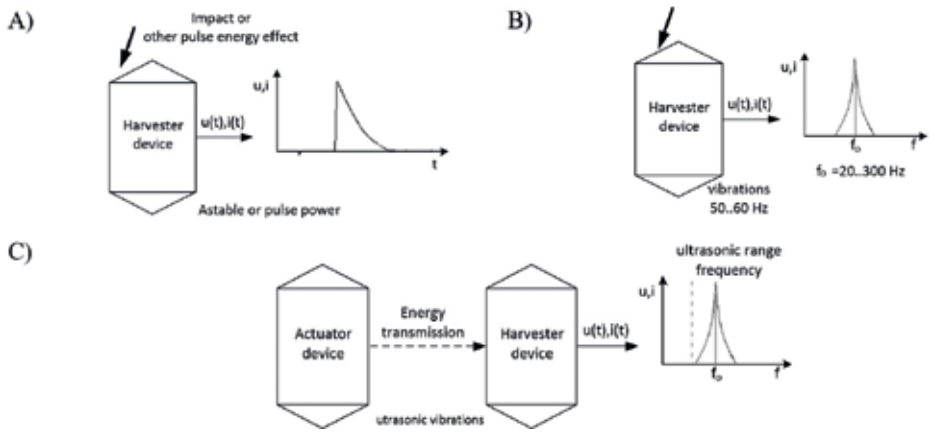

Figure 7. Energy harvesting sources and their power requirements: (A) mechanical impact, (B) low-frequency mechanical resonance and (C) energy transmission by ultrasonic vibration [17].

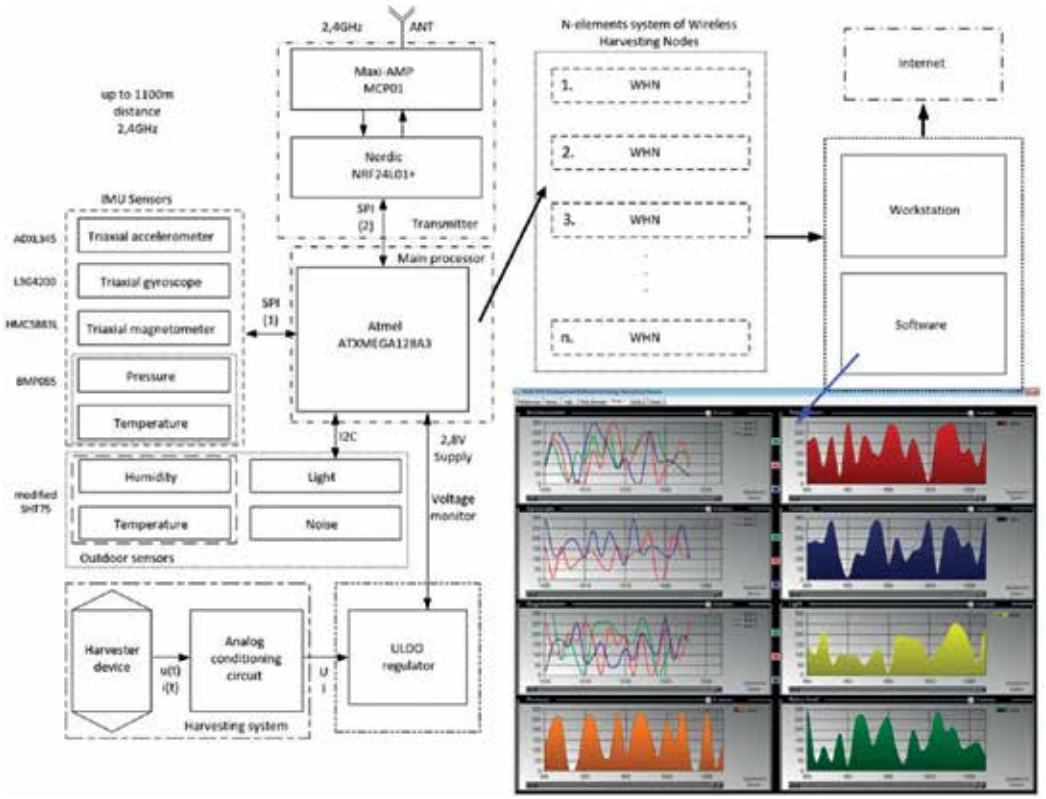

Figure 8. Prototyping of multi-DOF wireless sensors platform: Main communication station and Multi-DOF software [17].

to be effective. For this purpose, Smart Ultrasonic Resonant Power System (SURPS), a system for simultaneous power and data transmission, was developed. It ensured transmission through various media (solid, liquid) and with various transmitter-receiver configurations [17].

After matching the sensor-microprocessor configuration with a suitable energy harvester, the whole packets, together with a wireless communication system, were placed in the nodes. Due to the fact that every node is equipped with the same wireless communication system, different types of sensors can be easily substituted or put together by the user, thanks to the dedicated software shown in **Figure 8**.

A properly selected conditioning circuit provides the harvesting system with a certain current and voltage output. The creation of a wireless node to measure certain physical quantities and to monitor the level of recovered energy requires the selection of an appropriate hardware platform, such as a microprocessor and a wireless transmission system.

3. The idea of the composite rod in the wideband actuator and energy harvester

Bearing in mind the justifiability of limiting the use of solid Terfenol-D in the construction of magnetostrictive resonators, two solutions are presented below, namely the use of a GMM composite core and—in Chapter 4—a core consisting of a neodymium magnet and Terfenol-D.

3.1. The preparation of GMM composite

Referring to price of Terfenol-D which is a relatively expensive material, a device which would not require this material would be adequately cheaper. The brittleness of pure Terfenol-D can be replaced with a composite material [7].

A prospective application area for Terfenol-D, which is a typical representative of the GMM group, is (electric) energy harvesting from, for example, mechanical vibration systems [18, 19]. However, some of the applications of this material are restricted due to eddy current loss at a high frequency. In addition, it has some drawbacks, such as intrinsic brittleness accompanied by maximizing the fraction of the brittle, Laves phase. The magnetostrictive composite materials have been developed as an alternative way to overcome both the eddy current loss and intrinsic brittleness since 1990.

The main advantages of magnetostrictive composites based on a nonmagnetic polymer matrix and containing Terfenol-D powder particles are as follows:

- reduction of solid Terfenol-D's drawbacks (eddy currents at higher operating frequencies and its brittleness limiting its use under, for example, tensile stress [1, 20], whereby its application range is significantly extended,
- new potential applications in, for example, (SHM) composite materials and structures (tagging) [21].

Therefore, the main goal of this research was to investigate the magnetostriction of a field-structural composite with Terfenol-D particles. The composite should replace the solid Terfenol-D rods in an actuator or a damper. It was decided to closely examine the effect of the

(perpendicular, parallel, without polarization) direction of composite polarization and different frequencies of magnetic field stimulation. The results were compared with those obtained for solid Terfenol-D samples with the same geometry.

In the study, a magnetostrictive composite was used (hereafter referred to as GMMc). It was prepared in the Department of Mechanics, Materials Science and Engineering at Wroclaw University of Science and Technology. The composite was made by combining an epoxy resin and Terfenol-D powder (GMM material).

- The first step was introduction of a hardener to the epoxy resin.
- The next step was the addition of a properly measured amount of Terfenol-D powder with a grain size of 0–300 μm (according to the manufacturer, Gansu Tianxing Rare Earth Functional Materials Co., Ltd.).

Specimens presented in this work contain 70% of Terfenol-D particles volume fraction, and they have different polarization directions. For each case, the particles and resin were homogeneously mixed together and deaerated. Moreover, one of the samples was polarized perpendicular, and others were polarized parallel to the main axis of the specimen. This effect was obtained by using permanent magnets and coil during a composite curing process, respectively.

The container with the mixture was placed between two magnets or inside a coil and after that it was placed on an MTS hydraulic pulsator, where samples were pressed with a force of 10 kN for 4 h until the preliminary resin binding started. This process allowed to reduce the excess of epoxy resin from samples and to obtain a high volume fraction of Terfenol-D particles. The schemes of these processes for perpendicular and parallel polarized specimens are shown in **Figure 9A** and **Figure 9B**, respectively. Additionally, one of the specimens was cured without any source of a magnetic field.

After 24 h preliminarily cured specimens were placed in an oven at 70°C for another 24 h to ensure the full cure of the epoxy resin. Samples produced in this way contain a small portion of pores, which confirms the good connection of powders with resin. The polymer material provides a good magnetic insulation of the Terfenol-D powder grains and prevents its oxidation.

3.2. Experimental determination of GMMc parameters

To determine if the polarization applied during the curing process to the manufactured composites made any changes in the magnetization of specimens, the magnetic scans of their surfaces were made (**Figure 10A** and **Figure 10B**). The scans were obtained with the use of the innovative system of Magscanner described in [23]. The results show clearly that there is a difference between the manufactured specimens with different types of polarization. The magnetization layout along its main axis for the parallel polarized specimen (**Figure 10A**) is even as evident, as the one contrasted with the parallel polarized specimen (**Figure 10B**). This confirms that polarized samples preserved the direction of the desired magnetization.

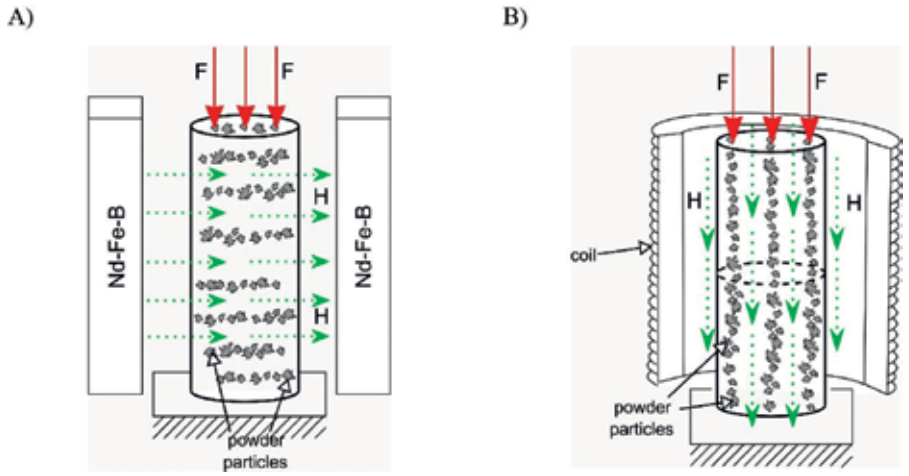

Figure 9. Schema of perpendicular (A) parallel (B) polarization to the main axis of the sample during curing process. F—direction of force during curing process, H—direction of magnetic field during curing process [22].

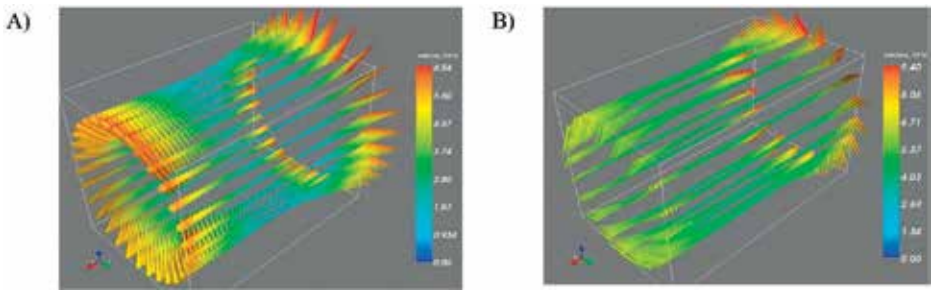

Figure 10. 3D magnetic vector fields around perpendicular (A) and parallel (B) premagnetized Terfenol-D composites [22].

The experiments methodology involving the quasi-static measurements of the magnetostriction of the produced composites and the measurements made for different magnetic field frequencies is shown later.

The magnetic field strength acting on the magnetostrictive composite was dependent on the strength of the current in the coil. The magnetic field was generated by an adjustable power supply unit (0–30 V, 20 A). The magnetic field strength range H was limited by the magnetic circuit and amounted to 0 ÷ 168 kA/m. The measurement was conducted with the use of the Hall's sensor (placed inside the coil), for both positive and negative H values to check the evenness of the phenomenon in the composite samples. Sample displacement $\Delta\lambda$ was measured using the innovative method of fiber Bragg grating (FBG) sensors. In this way, the influence of the electromagnetic field on the results was eliminated. The FBG method is described in more detail in [24]. The strain sensors were placed directly on the specimens, as shown in **Figure 11**. One of the sensors was placed along the main axis of the specimen while the other one was attached to the sample circumference. The aim of such a sensor arrangement was to

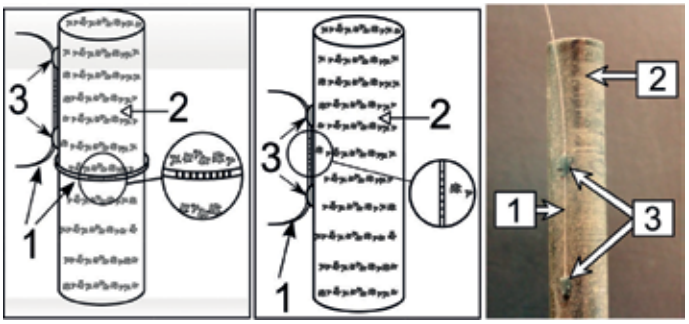

Figure 11. Arrangement of the strain sensors on a sample: 1—Sensors, 2—Specimen, 3—Glue [22].

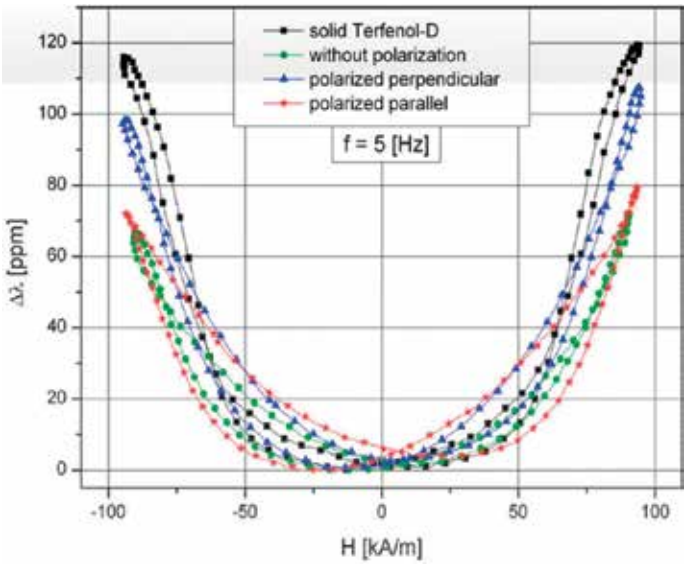

Figure 12. Comparison of magnetostrictive dependence from magnetic field intensity H, at frequency f = 5 Hz, for composite specimens and solid Terfenol-D [22].

check whether the volumetric magnetostriction occurs in the material apart from the linear magnetostriction.

In addition, changes in the value of the magnetic field during the same test were presented in **Figure 12**.

4. Designing of magnetostrictive core for solid-type resonators

In this chapter, the problem of cores built with neodymium magnets and Terfenol-D and impulse power supply for the microcontroller is discussed.

4.1. Coupling of NdFeB magnets and Terfenol-D in the resonator core

The idea of the Top Core Coil Magnet (TCCM) actuators and reversible harvesters appeared in the Department of Mechanics, Materials Science and Engineering laboratories. The basic model of unique TCCM system is shown in **Figure 13**. The model called TCCM is a construction combining four major elements: Top whose role was to transfer shock to the core, Coil, Magnet and Core which determines the processing energy of impact (obtained from the Top part) into electricity. The TCCM harvester is the simplest form of the implementation of the harvester based on the core placed in the coil with a fairly large number of coils in the magnetic field of the NdFeB magnet. Low rigidity and low resonance frequency at the moment of impact describe the system without the prestress.

The range of measurement and devices used to perform the testing of actuator/harvester response is presented below:

- IXFN20N200, MOSFET by IXYS, a fast transistor for linear motor was used to provide the speed of a defined value for moving aluminum frame
- Encoder strip coupled with a reader by Sharp Company, path measurement system of 720 dpi resolution;
- Hi-speed, Hi-power linear motor-dumper up to 20 N hammer used to provide impact energy;
- PZT sensor used to measure force signal in the place of mounting;
- (TMS320C6701 DSP) Hunt Engineering Heron System by Texas Instruments, with GFLOPS performance at a clock rate of 167 MHz, used for high-performance DSP programming. It possesses the operational flexibility of high-speed controllers and the numerical capability of array processors. The processor has 32 general-purpose registers of 32-bit word length and 8 highly independent functional units;
- The Heron HEPC8 Module Carrier Board is a PCI form factor module carrier board supporting up to four Heron modules which can be multiplied. HEPC8 provides 32-bit first-in, first-out (FIFO) buffers between each module slot and the other module slots on the board for data transfer between Heron modules;
- Laser switch by Balluff Company used to trigger the start of acquisition;
- PicoPower Evaluate System v0.8 2010, PicoPower Processor Development Platform by the Institute of Material Science and Applied Mechanics of WrUST, designed in the Institute as the main testing system;
- Capacitors by EPCOS Company of 2.2uF.

The scheme of the test stand for the shock test TCCM harvesting system based on a high-speed linear motor is shown in **Figure 14**.

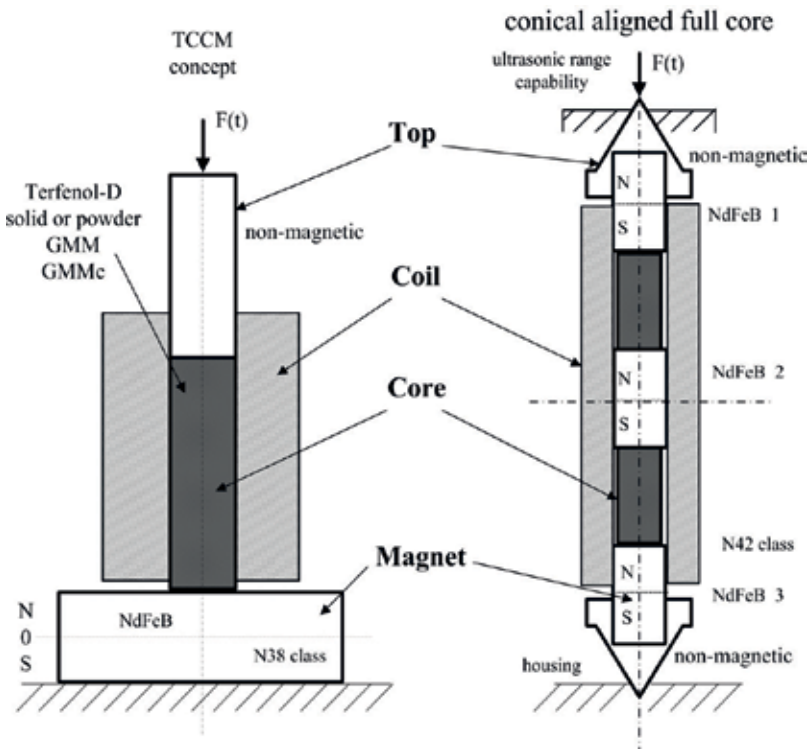

Figure 13. Scheme of the magnetostrictive core used as reversible effect resonator in energy harvesting devices [16].

The TCCM device was fixed with a PZT sensor in the horizontal orientation on a nonmagnetic, hard surface. In the main axis of the device, at the distance of 80mm was the aluminum hammer. Its speed accelerates to a defined value due to the fast linear motor transistor MOSFET. The speed of hammer was measured with an encoder strip coupled with a reader. The energy of impact was controlled by weights attached to a linear motor moving element. The maximum weight that could be used to accumulate energy is 2 kg. Due to the small size of a harvester, a beater load of 0.5 kg was used. The high reproducibility of the hammer speed and run-off place of the transistor MOSFET were obtained for that test stand, which resulted in the stability of impact energy E_k.

The shock force was applied to the TCCM device and, as a result, the impulse response of system was registered, as shown in **Figure 15**. Upon the analysis of this signal, the waveform was divided into phases. The first phase occurs before the strike, where the increase in voltage is present as a result of the motion of ferromagnetic hammer in the neodymium magnet's magnetic field. After the strike moment, wave motion passing through the top and the core to the neodymium magnet occurs and creates a string change of the magnetic field of the system, which causes the induction of the voltage resulting from the mechanical resonance frequency of the TCCM harvester.

Only the top and coil materials have an influence on the resonant frequency. The wave that passes through the material inside the coil either circulates repeatedly in the steam-core-magnet system or comes out of the harvester if the magnet has contact with the other surface,

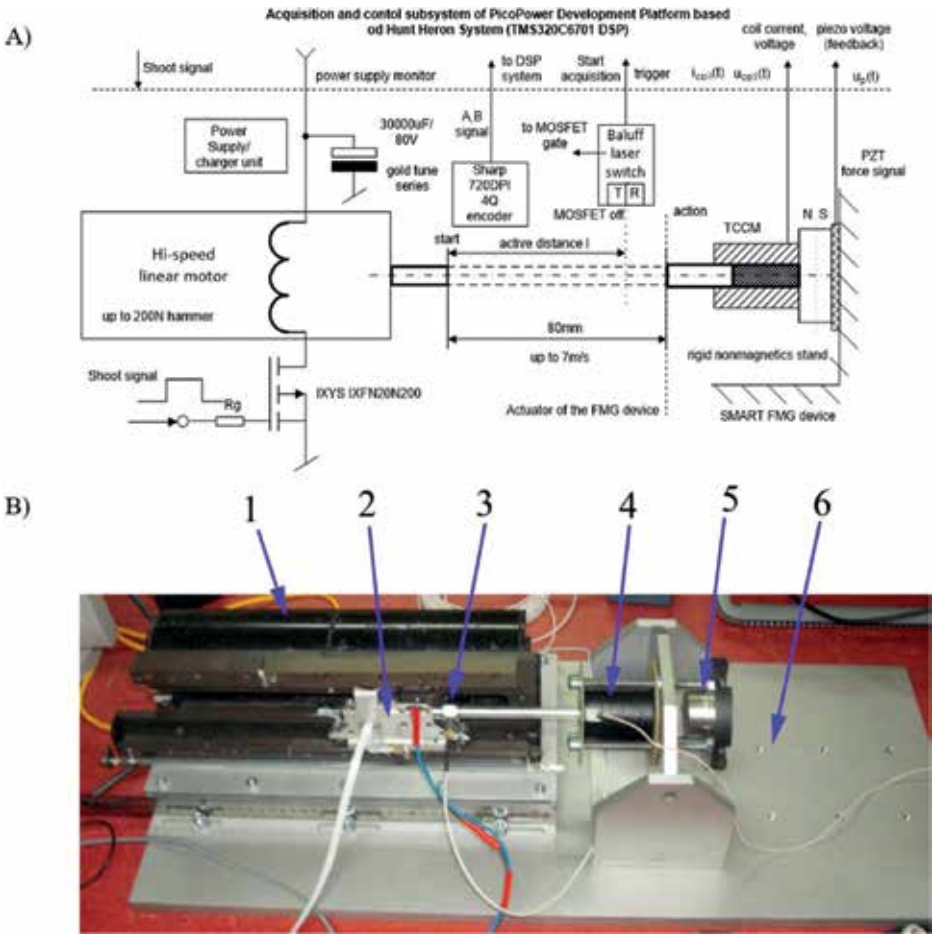

Figure 14. The schema of test stand to determine magnetostrictive core parameters (A): (1) linear motor, (2) movable trolley of a linear motor, (3) piezoelectric force sensor, (4) inductor, (5) NdFeB magnets used for constant magnetic field generation around the inductor, (6) base plate with the inductor position regulation. View of the test stand (B) [16].

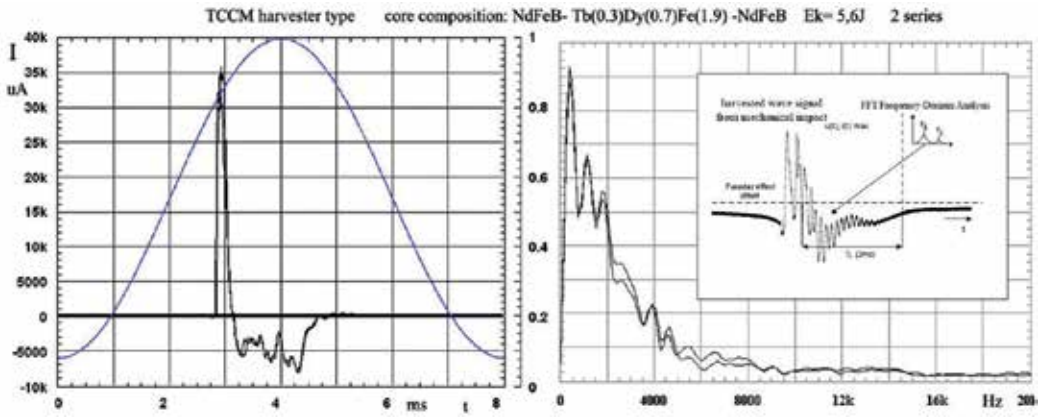

Figure 15. The current coil measurement for bulk Terfenol-D and its FFT plot.

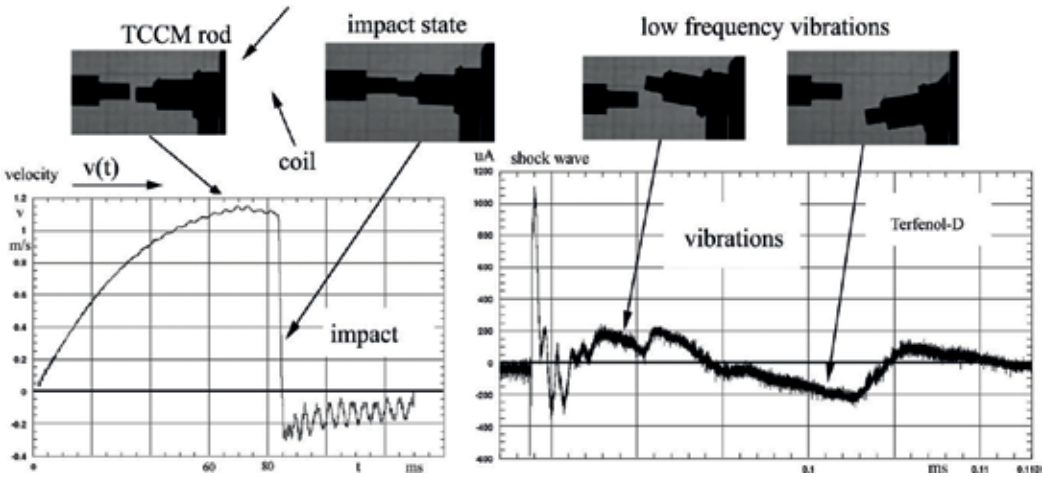

Figure 16. Photo series of mechanical impact correlated with velocity and pulse output voltage graphs.

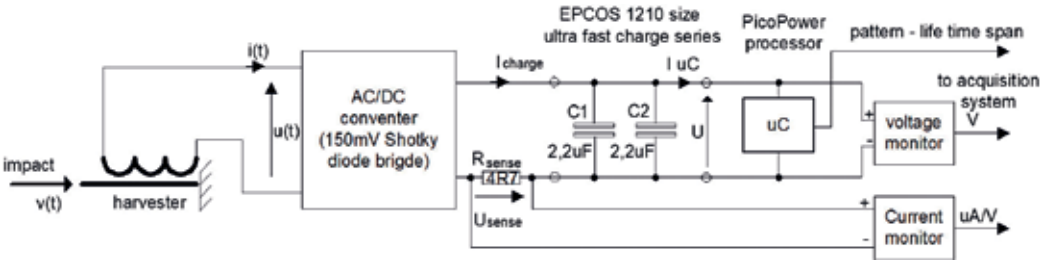

Figure 17. Supply current and voltage measurement scheme for detect life time span of powered μC [16].

but it is not transferred to this coil. The crucial effect in the operation of the top-coil-magnet system is the mechanical resonance effect of that system under impact. In **Figure 16**, the hammer impact chart of the TCCM harvester with correlated photos is shown.

In the TCCM type of Energy Harvester construction the calibration of prestess cores is not as critical as in vibrations exciter device. The prestress is obtained in the first phase of impact where the main maximum useable signal occurs. The significant increase in current and voltage occurs at the moment of the resonance frequency of the system. The value of this voltage depends on the number of turns in the coil when the same impact energy is applied.

4.2. Practical aspect of pulse power supply

The idea of a working harvesting device was not to supply continuous power for the microcontroller, but to provide a strong enough current pulse to quickly charge a high-capacity capacitor, see **Figure 17**. These capacitors were chosen in such a way that the processor voltage did not exceed 5.5 V. The role of the capacitor is very important, and hence, special capacitors which are able to capture the impulse current within a few dozen μF must be used.

As the practical application of the pulse power supply (PPS), the acquisition of lifespan of an ATMEL microcontroller based on the primary node was chosen. The ATMEGA48V system was used as a low-power processor. It is one of the most common microcontrollers in industrial applications. It could be started at a voltage level of only 1.8 V. It was powered by a DC of 1.8– 5.5 V, as an AC/DC system transducer on the rectifier used Schottky diodes. The signal acquisition and the control of the test parameters of the harvesting device, the AC/DC rectifier, a microprocessor and a base station were provided by a dedicated system.

In **Figure 18**, the current consumption by the system capacitors -μC type recorded as a reduction in voltage on measuring resistor R_{sense} = 4.7 Ω is presented. In the first phase, there is a very strong increase in current due to the initial charge on C1 and C2 capacitors (**Figure 17**), which are very heavy load on the signal generated by the harvesting device, followed by a decline in current consumption, given that it has not yet started μC. The "life time" algorithm of the program allows the microprocessor to send more than 50 pulses in a voltage range from U_{max} = 5 V to U_{min} = 1.8 V, which can be described as about 3 ms of μC life. By selecting various sources of the mechanical extortion obtained values of the microprocessor, one can cause pulses to rise up to 200 and the life time to extend to 8 ms. Based on the results, it can be found that an energy harvesting device (EHD) was developed. EHD is able to supply a popular microcontroller which realizes its code throughout the life of 3 ms from small impact energy E_k = 0.25 J. The core of this device was made of Terfenol-D powder.

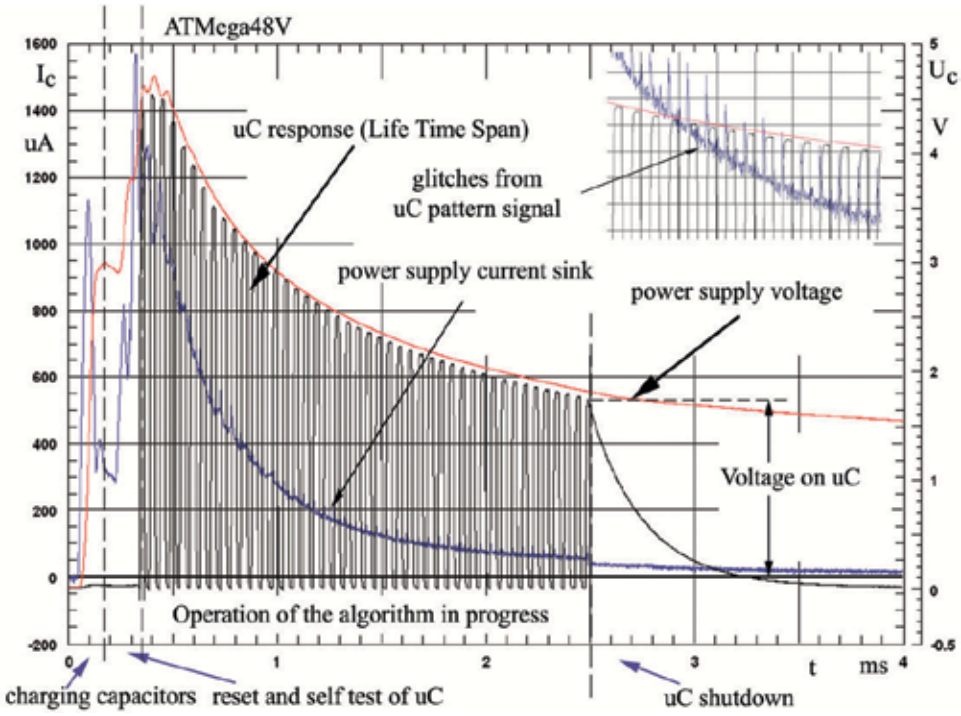

Figure 18. Life time span of microcontroller\circuit powered from energy harvesting device induced at low impact energy E_k = 0.25 J [16].

5. Construction of high-power wideband actuator

5.1. Design of classic magnetostrictive actuator dedicated for mechanical vibrations in selected frequency range

During the process of selecting the geometry of the actuator, the authors decided to use know-how gathered during previously performed computer simulations. To achieve the goal, they did not restrict the maximum value of the displacements obtained during test in any way. The only limitation was the maximum value of the magnetic field used to stimulate the material. It was assumed that the actuator together with the system will operate most of the time at a specific value of DC power, which necessitated the use of open housing design. This solution was chosen due to the fact that when the system is DC powered for a longer time, the electromagnet coil generates a lot of heat. The heat should be dissipated as soon as possible. The main component of the system was the magnetostrictive composite material with Terfenol-D powder which was obtained in the way described in the previous part. The visualization of the parametric model of the actuator is presented in **Figure 19**. It can be observed that its structure is not very complex; however, it allows to obtain high values of the magnetic field

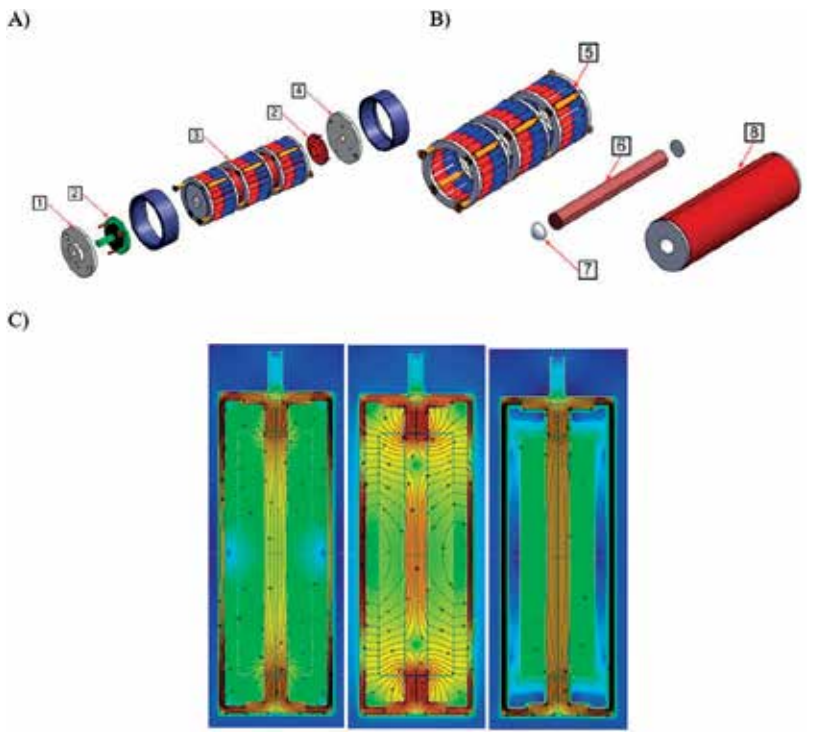

Figure 19. Construction of the basic type of magnetostrictive actuator for acoustical frequency band applications (A), magnetic core structure (B), simulations of magnetic field around magnetostrictive core and actuator body (C). Components define: 1-front cover, 2-rod centering alignment, 3-magnetic core, 4-back cover, 5-outer NdFeB ring, 6-GMM(c) rod, 7-alignment tip, 8-coil [22].

and provides easy access to the core of the device. Two plates, top and bottom, made of ferromagnetic material are the main elements of the actuator housing. They are intended to spread the magnetic field uniformly and to prevent the excessive loss of the magnetic field inside the coil. Thus, the authors decided to use square plates which allowed to preserve symmetry.

In addition, four middle elements with a cylindrical shape made of a ferromagnetic material were used. The shape of these connectors was conditioned by the fact that in the case of parts with sharp edges, the concentration of the magnetic field appears on those edges. Therefore, it impedes the free flow of the magnetic field and may cause disturbances in the propagation of the magnetic field around the coil. The cylindrical shape of the connectors allows a more uniform distribution of the magnetic field and limits losses. Additionally, the number of connecting elements was chosen in such a way that they ensure a secure and stable connection between the two plates of the housing, while preserving as many open spaces as possible. This solution results in a sufficiently large heat radiation area for the cooling of the coil. Due to the fact that the actuator will work in applications where different displacement values will be required, it was necessary to increase the external dimensions of the actuator, including its housing. However, it should be noted that the construction is compact and simple.

During the design process of the actuator system, the authors decided that it should meet the following requirements:

- provide a compact and simple construction,
- ensure the electric and magnetic safety of the user and the whole construction,
- provide easy access and allow for the replacement of the sample,
- allow to control the value of pre-stress on both solid and magnetostrictive composite materials,
- ensure an easy installation procedure on the test rig or in the case of potential applications,
- provide easy control of the entire system.

Among the components of the actuator, one can find a sleeve made of bronze which was located at the top of the housing. The reason for the usage of such an element is to reduce the potential friction that could occur between the upper rod of the actuator and the upper plate during system operation. It should be noted that although the elements which ensure the alignment of magnetostrictive material are used, even a small deviation from the vertical position of the sample could cause friction between the active element and the top of the housing. This might cause a high reduction of the parameters of the actuator and, what is more, it would influence the ability to control the device with the use of a feedback loop. In addition, the interior of the housing is protected by the elastic ring (which is not shown) whose main task is to ensure the prestress, that can be adjusted by lowering the connecting rods. The possibility to adjust prestress is very important due to its influence on the obtained magnetostriction value. A real construction of the actuator is shown in **Figure 20**.

5.2. High power actuators with magnetostriction feedback

Based on results described in the previous part of this chapter, a specific coil was chosen for the new type of actuator (**Figure 21**). This coil allows a relatively long time of work at a constant DC current level, and at the same time ensures the slowest growth of temperature. Due to the characteristics of the GMM material, the system test can be performed for a small value of the magnetic field which should be approximately 200 kA/m. Because of the predicted specification of the working characteristic of the system, it was decided that the system responsible for the preliminary magnetization of the sample will affect only the initial increase in the magnetic moment of the material. Therefore, the control of the system allows to increase the current value, which causes the deformation of the material only in one direction, regardless of the phase of the magnetic field generated in the coil.

In addition, due to the necessity to measure the deformation of the actuator core made of a GMM, it was decided to implement the Fiber Bragg grating sensor. This solution allowed to increase the accuracy thanks to which it was possible to control the actuator and neutralize the effect of the electromagnetic field on the control of the device. It significantly helped during the preparation of the control algorithm. The use of fiber optic sensors forced additional changes in the design of the actuator which allowed to mount fibers directly into its core. At the same time, it was easier to measure the deformation of the sample.

The goal of testing was to obtain the quasi-static and cyclic properties of the actuator and check the possibility of using the feedback loop control of the actuator. The use of cyclic tests means that during the test there is an alternating deformation of the composite core inside the actuator which is caused by stimulating the magnitude of the magnetic field in the frequency range from 1 to 20 Hz. For each test, a change of deformation of the composite core, at the corresponding values of the magnetic field, was recorded. The obtained data allowed to determine the maximum value of magnetostriction, depending on the method of stimulation. The study consisted of determining changes in the magnetic field with the use of a triaxial Hall probe and the deformation of the sample with a Fiber Bragg grating sensors. Additionally, during

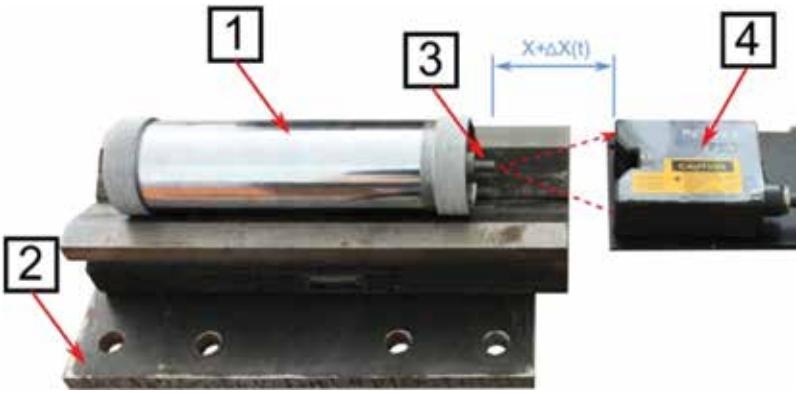

Figure 20. Photo of prototype GMM actuator during laser examinations of true tip displacement under programmed magnetic field stimulations: (1) – assembled actuator, (2) – Rigid stand, (3) – tip and (4) – Keyence LK series – laser sensor.

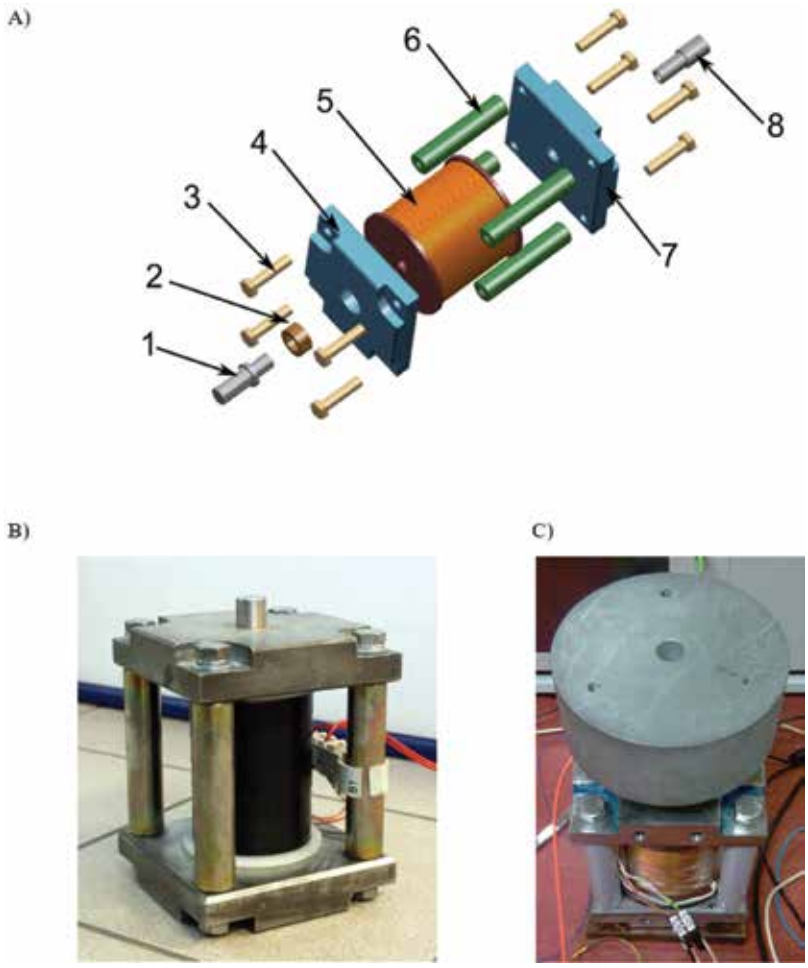

Figure 21. The high power actuator: model components (A): (1) – upper rod (actuator), (2) – Bronze sleeve, (3) – bolts, (4) – upper housing plate, (5) – coil with composite core, (6) – connection elements, (7) – bottom housing plate and (8) – bottom rod , the higher frequency version (low induction coil) (B), version with FBG and magnetic sensors for regulators of vibrations applications (C) [25].

the investigations the value of the prestress applied to the composite core was changed. This solution was proposed to check whether the value of prestress affects the value of obtained magnetostriction. In addition, during the study, it was checked whether the proposed deformation control algorithm of the magnetostrictive core was valid and able to control the system working in the feedback loop. In such a system, the controlled value is the value of magnetostriction. **Figure 22** shows the schema of the experimental system of the actuator feedback loop.

The same values of the pre-stress showed that it does not change the value of the magnetostriction of the composite material regardless of the test method (quasi-static or cyclic). In the following figures, a comparison of the performance of the actuator in the case of the application of the feedback loop system and without such a system is presented. The subsequent numbers in the graphs correspond to the following steps during the test:

1. start of the measurement and application of magnetic field,
2. loading of the actuator (load 200 N) (blue dashed line),
3. unloading of the actuator (red-dashed line).

Figure 23 presents the result of the deformation of the material in the actuator when the feedback loop system was off. The actuator was loaded with the weight of 20 kg. It is clear that under the influence of the applied load the value of the received magnetostriction decreased so did the active rod. Such a rod which can be used, for example, for control in various applications, did not keep its position. Moreover, in the case of the system without the feedback

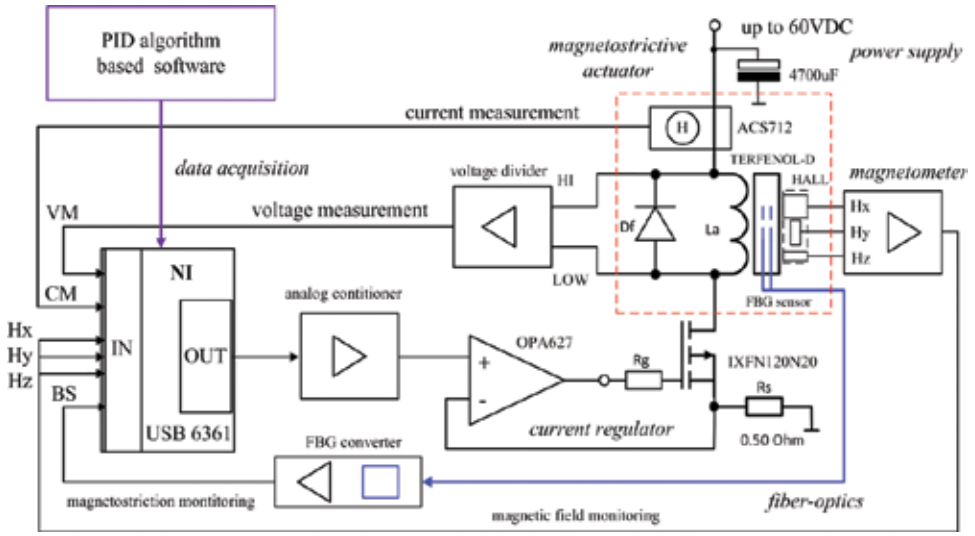

Figure 22. Schema of high power GMMc vibration exciter core that can be controlled using PID controller.

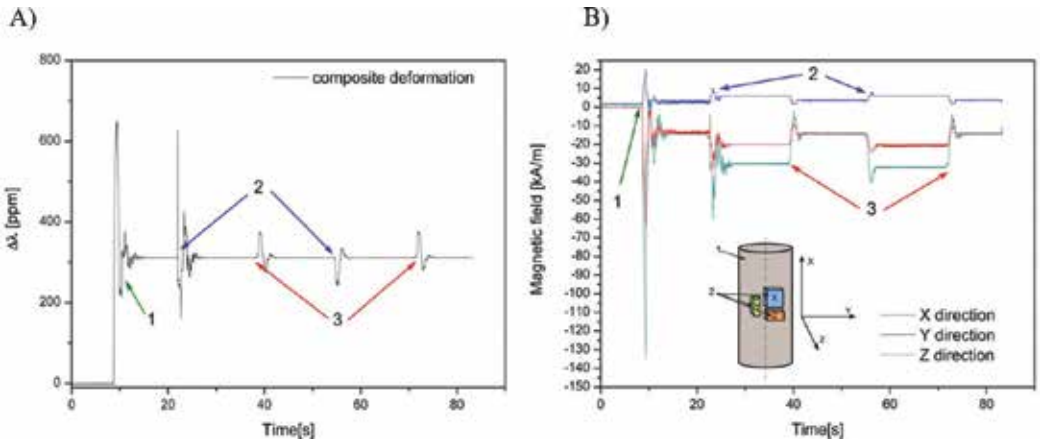

Figure 23. Deformation of the magnetostrictive rod with a feedback loop system (A), tri-axial magnetic field measurement using hall sensors attached to the sample: (1) – Sample, (2) – Sensors (B) [25].

loop, the value of the magnetic field did not change during the experiment, as it is shown in **Figure 23A**. This response of the actuator can be predicted.

The results show changes in the magnetic field recorder shown by each of the three Hall sensors placed inside the actuator coil. The measurement direction of the Hall sensors are as follows: X direction along the main axis of the sample, Z direction toward the sample and Y direction on the outside of the sample (**Figure 23B**).

Table 1 summarizes the most important parameters of the high power actuator.

The frequency response of the high power actuator is shown in the **Figure 24**.

Moreover, it is shown that it is possible to actively control the displacement of an actuator which is based on the magnetostrictive composite core with a feedback loop system. The control of such a system is based on the changes of the intensity value of the magnetic field around the composite core. In addition, through the use of fiber optics strain sensors, the measuring system made it possible to simplify the control of the deformation of the material. Certainly, it is still necessary to further develop this system to improve its parameters; however, at this stage one may say that it can be used in many different applications.

1.	Maximum DC current with forced cooling	10 A continuous, up to 80°C
2.	Maximum real power	400 W, 30% duty cycle
3.	Static displacement of tip as a unit step	More than 50 μm, 1 kN load
4.	Static impedance	3.8 Ω with terminal connections
5.	The range of permissible loading force	5 kN, only compression
6.	Useful frequency range	0–500 Hz

Table 1. The main operational parameters of the actuator (**Figure 21C**).

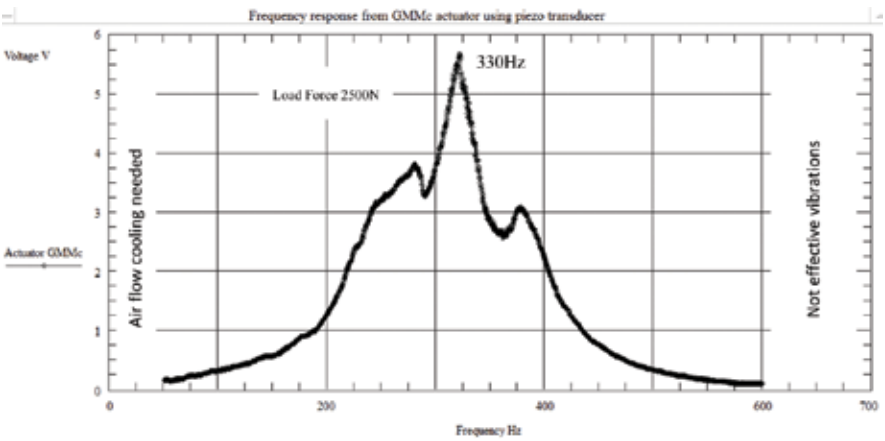

Figure 24. Frequency response of the high power actuator with FBG magnetostriction feedback.

6. Conclusions and final remarks

The chapter presents the design and test methodology of wideband magnetostrictive resonators, that is, actuators and energy harvesting devices. Detailed conclusions are presented below:

- The magnetostriction phenomenon as magnetomechanical cross-effect enables new concepts of the research methods for designing of effective actuators utilizing mechanical vibrations in a selected frequency band, even in an ultrasonic range.
- Similarly to piezo transducers, magnetostrictive cores allow to create sensor-actuator reversible devices. The choice whether the transducer is a sensor or an actuator is dictated by the amount of active material. In the smallest scale, even a sensor can be used as an actuator.
- The concept of a mechanical resonator has been introduced, which can be understood as an actuator or an energy harvester. A wideband actuator and a harvester can be the same device.
- By evaluating the effects of polarization direction, it was found that composites with perpendicular polarization show the highest magnetostriction value in comparison to the others, such as parallel polarized and the ones without polarization in the entire frequency range. What is more, at higher values of frequencies the response of the composite material was comparable with monolithic Terfenol-D, and this is why it can be suggested that the composite material provides the basis for applying it in actuating devices.
- The measurement of the deformation of the actuator core was carried out with implementation of the Fiber Bragg grating sensor. This solution allowed to increase the accuracy of measurements and neutralized the effect of the electromagnetic field on the results.
- The magnetostriction of the GMM composites achieved in this work can be further improved by more accurate fabrication parameters, especially by the investigation of polarization and differences in the volume fraction of particles. Moreover, research on different matrixes as binders could show if the behavior of a matrix-powder connection will have influence on the properties of these materials.
- Magnetostrictive cores based on NdFeB magnets and pure Terfenol-D or its replacement composites were designed and verified on the real constructions of devices. Testing methods and dedicated systems have been developed for applications both as a wideband actuator or as an energy harvesting device.
- The described method of energy transformation allows the usage of mechanical shock to generate the electric current. The current signal frequencies spectrum, generated in a coil due to the wave movement, is determined by the magnetic resonance frequency. This fact allows the selection of a specific harvester depending on the working environment frequency.
- The authors design and prototype various groups of harvesters, mainly with the magnetic core ("Pulse Power Supply"), for use as power supplies which are capable of producing tens of watts in a few milliseconds.

Acknowledgements

The research was funded by the Ministry of Science and Higher Education (Republic of Poland) within grant number 0401/0029/17.

Author details

Jerzy Kaleta*, Rafał Mech and Przemysław Wiewiórski

*Address all correspondence to: jerzy.kaleta@pwr.edu.pl

Department of Mechanics, Materials Science and Engineering, Wrocław University of Science and Technology, Wrocław, Poland

References

[1] Engdahl G. Handbook of Giant Magnetostrictive Material. San Diego, CA, USA: Academic Press; 2000

[2] Brauer JR. Magnetic Actuators and Sensors.1st ed., Hoboken, New Jersey: John Wiley and Sons; 2006

[3] Braghin F, Castelli-Dezza F, Cinquemani S, Resta F. A full-range hybrid device for sound reproduction. Smart Structures and Systems. 2013;**11**(6):605-621

[4] Kim Y, Kim YY. A novel Terfenol-D transducer for guided-wave inspection of a rotating shaft. Sensors and Actuators A. 2007;**133**:447-456

[5] Sathishkumar R, Vimalajuliet A, Prasath JS. Terfenol D: A high power giant magnetostrictive material for submarine mapping. International Journal of Engineering Science and Technology. 2010;**2**(12):7165-7170

[6] Calkins FT, Flatau AB, Dapino MJ. Overwiev of magnetostrictive sensor technology. Journal of Intelligent Material Systems and Structures. 2007;**18**(10):1057-1066

[7] Kaleta J. SMART Magnetic Materials. Construction, Manufacture, Properties Testing, Application (in polish). Wrocław, Poland: Publishing of Wrocław University of Science and Technology; 2013

[8] Kendall D, Piercy AR. Terfenol-based materials with reduced eddy-current loss for high frequency applications. Ferroelectrics. 1996;**187**:153-161

[9] Altin G, Ho KK, Henry CP, Carman GP. Static properties of crystallographically aligned Terfenol-D/polymer composites. Journal of Applied Physics. 2007;**101**(3):033537-033537, 033536

[10] Ching YL, Siu WO, Helen LWC. Large magnetostriction in epoxy-bonded Terfenol-D continuous-fiber composite with [112] crystallographic orientation. IEEE Transactions on Magnetics. 2006;**42**(10):3111-3113

[11] Dong X, Qi M, Guan X, Ou J. Fabrication of $Tb_{0.3}Dy_{0.7}Fe_2$/epoxy composites: Enhanced uniform magnetostrictive and mechanical properties using a dry process. Journal of Magnetism and Magnetic Materials. 2011;**323**:351-355

[12] Jianjun T, Zhijun Z, De'an P, Shengen Z. Bonded Terfenol-D composites with low eddy current loss and high magnetostriction. Rare Metals. 2010;**29**(6):579-582

[13] Kwon OY, Kim JC, Kwon YD, Yang DJ, Lee SH, Lee ZH, Hong SH. Magnetostriction and magnetomechanical properties of grain-oriented $Tb_{0.33}Dy_{0.67}Fe_y$/epoxy composite. Applied Physics A. 2005;**80**:1563-1566

[14] Dai X, Wen Y, Li P, Yang J, Zhang G. Modeling, characterization and fabrication of vibration energy harvester using Terfenol-D/PZT/Terfenol-D composite transducer. Sensors and Actuators: A Physical. 2009;**156**(2):350-358

[15] Bomba J, Kaleta J. Giant magnetostrictive materials (GMM) as a functional material for construction of sensors and actuators. In: 19th Danubia-Adria Symposium on Experimental Methods in Solid Mechanics; 2002. pp. 80-81

[16] Kaleta J, Lewandowski D, Mech R, Wiewiórski P. Energy harvester based on Terfenol-D for low power devices. Interdisciplinary Journal of Engineering Sciences. 2014;**2**(1):8-12

[17] Kaleta J, Kot K, Rikitatt M, Wiewiórski P. Multidof wireless sensor system based on IMU-MEMS technology supported by energy harvesting methods. In: Recent Advances in Integrity-Reliability-Failure: IRF, Edições INEGI; 2013. pp. 359-360

[18] Monaco E, Lecce L, Natale C, Pirozzi S, May C. Active noise control in turbofan aircrafts: Theory and experiments. Acoustics. 2008;**08**:4629-4634

[19] Pouponneau P, Yahia L, Merhi Y, Epure LM, Martel S. Biocompatibility of candidate materials for the realization of medical microdevices, In: Proceedings of the 28th IEEE EMBS Annual International Conference; 2006

[20] Hedrick JB, Rare Earths in Selected U.S. Defense Applications, 40th Forum on the Geology of Industrial Minerals; 2004

[21] Quattrone RF, Berman JB, Trovillion JC, Feickert CA, Kamphaus JM, White SR, Giurgiutiu V, Cohen GL, Tech. Rep., US Army Corps of Engineers and Engineer Research and Development Centre; 2000

[22] Mech R. Magnetomechanical properties of composites based on giant magnetostrictive material powders, (in polish) [PhD thesis]. Wroclaw University of Science and Technology; 2015

[23] Kaleta J, Wiewiórski P. Magnetic field distribution detecting and computing methods for experimental mechanics. Engineering Transactions. 2010;**58**(3/4):97-118

[24] Blazejewski W, Gasior P, Kaleta J. Advances in Composite Materials—Ecodesign and Analysis, Application of Optical Fibre Sensors to Measuring the Mechanical Properties of Composite Materials and Structures. Rijeka, Croatia: InTech; 2011

[25] Mech R, Kaleta J, Kot K, Wiewiórski P. High power actuator based on magnetostrictive composite core with temperature drift compensation. Key Engineering Materials. 2014;**598**:69-74

Section 2

Control Systems

Chapter 5

Modeling, System Identification, and Control of Electromagnetic Actuators

Alexandru Forrai

Additional information is available at the end of the chapter

http://dx.doi.org/10.5772/intechopen.75088

Abstract

This chapter is dedicated to modeling, system identification, and control of electromagnetic actuators with the main focus on the actuators used in magnetic levitation, in fuel injection systems, and in variable valve timing (VVT). These actuators have a simple structure, good reliability, and low manufacturing costs. However, from control viewpoint, they are nonlinear systems and are open-loop unstable. Therefore, mathematical modeling, system identification-based parameter estimation, and control strategies are presented, when the moving armature is controlled around an equilibrium position or is controlled between the two extreme positions of the armature.

Keywords: electromagnetic actuator, modeling, identification, gain scheduled control

1. Introduction

Electromagnetic actuators are widely used in the industry, and they transform the electric energy into linear motion. From the large variety of applications, in this chapter we are going to focus on:

- Magnetic levitation
- Fuel injection systems and variable valve timing actuators used in internal combustion engines

These applications are relevant from control point of view: in the first case, the moving armature is controlled around an equilibrium position; in the second case, the armature might go under control between the two extreme positions—armature open and armature close.

Nevertheless, magnetic levitation—in particular a magnetically levitated train—is a good example, where closed-loop control plays a key role, since the open-loop system is unstable [1]. The system can be linearized around an operating point, and a linear controller can be designed.

Furthermore, magnetic bearings and their control are from a long time the focus of control system design community. Feedback linearization and asymptotically exact linearization of an active magnetic bearing are presented in [2, 3]. Advanced control strategies are discussed in detail in [4, 5].

Therefore, it makes sense to develop high-accuracy mathematical models, to investigate methods for parameter identification, and finally to apply control strategies to improve performance and reliability of the system.

We will discuss these topics in the next sections, but before that let us focus on applications, where electromagnetic actuators are widely used.

1.1. Magnetic levitation

Magnetic bearings in combination with high-speed electric motors are used across many industries, from oil and gas industry to electric power generation industry (i.e., high-speed electric generators) and from the semiconductor industry to nuclear industry, etc.

The main structure of the magnetic bearing is shown in **Figure 1** (reproduced from [6]).

Another well-known application of the magnetic levitation is the magnetically levitated high-speed train (Maglev; see **Figure 1**), having speeds over 500 [km/h] [7, 8].

1.2. Fuel injection and variable valve timing (VVT)

The main purpose of the fuel injection system is to deliver fuel to the cylinders. However, how that fuel is delivered is that it makes the difference in engine performance, emissions, and noise characteristics.

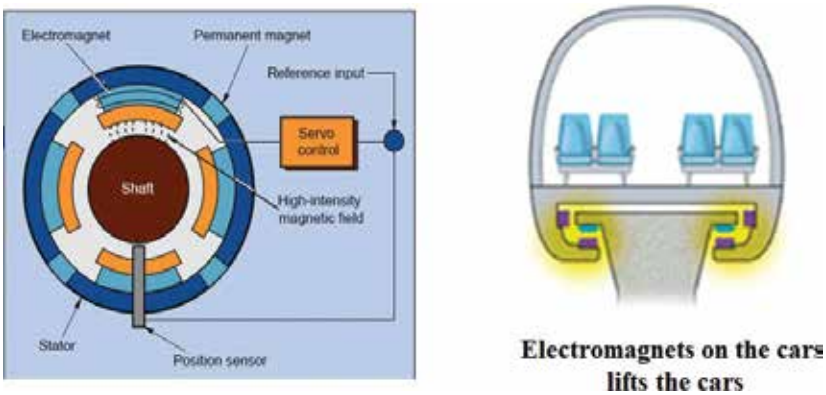

Figure 1. Applications of magnetic levitation.

Most notable advances achieved in diesel engines resulted directly from superior fuel injection system designs [9].

Unlike its spark-ignited engine counterpart, the diesel fuel injection system delivers fuel under extremely high injection pressures (e.g., around 2000 [bar]). This means that the system component designs and materials should be selected to withstand higher stresses [10].

The actuators used in diesel fuel injection systems can be either electromagnetic (our focus) or piezoelectric [11]. A diesel fuel injection system using an electromagnetic actuator, from Bosch [12], is shown in **Figure 2**.

Nowadays, most of the fuel injection systems are electronically controlled. However, it is still not enough to deliver an accurate amount of fuel at the proper time to achieve good combustion. Additional aspects are critical to ensure proper fuel injection system performance, such as [9]:

- Fuel atomization—ensuring that fuel atomizes into very small fuel particles is a primary design objective for diesel fuel injection systems.
- Bulk mixing—while fuel atomization and complete evaporation of fuel are critical, ensuring that the evaporated fuel has sufficient oxygen during combustion is equally important to ensure optimum engine performance.
- Air utilization—effective utilization of the air in the combustion chamber is closely tied to bulk mixing and can be accomplished by dividing the total injected fuel into a number of jets.

While conventional fuel injection systems employ a single injection event for every engine cycle, newer systems can use multiple injection events [12].

Using multiple injections—during every engine cycle—higher engine performance and lower engine noise can be achieved. However, the injector lifetime might be reduced, and therefore advanced control algorithms as well as malfunction detection and fault isolation algorithms can be applied (see next sections).

Figure 2. Diesel fuel injection system from Bosch.

Another relevant application is the electromechanical valve actuators used in automotive engines, to achieve variable valve timing (VVT). With VVT, larger valve overlap, valve lift, duration, and timing adjustments can be achieved depending on engine speed, load, and temperature.

Variable valve timing leads to improved fuel economy and lower emissions by decoupling the valve timing from the piston motion [13]. This is especially valid in case of advanced combustion technologies, as described in [14, 15].

However, the moving components of the valve actuators create unnecessary wear and excessive noise. The armature landing speed shall be kept, e.g., under 0.1 [m/s]; otherwise, they are excessively loud and are damaging to the actuator and engine valve.

Whenever high-performance and high-accuracy control is required, the electromagnetic actuator is driven by a half H-bridge (see **Figure 3**), which might be equipped optionally with a current sensing resistor R_{SENSE}.

Typical voltage and current waveforms as well as the switching order of the commutation elements T_1 and T_2 are shown in **Figure 3**.

After the electromagnetic armature is pulled up, the actuator current is reduced, and the commutation elements are controlled via pulse-width modulation (PWM).

During armature movement, due to the induced electromotive force (e.m.f.), a small current dip as well as a small current peak might be observed (see **Figure 3**).

The duty factor of the actuator—specified on the data sheet—is defined as

$$Duty[\%] = \frac{T_{ON}}{T_{ON} + T_{OFF}} 100[\%] \tag{1}$$

In practice, exceeding this value might shorten significantly the lifetime of the actuator.

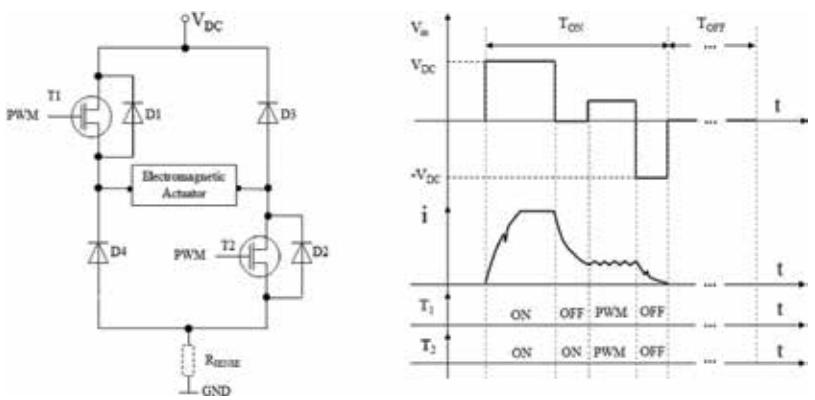

Figure 3. Electromagnetic actuator driven by a half H-bridge.

2. Mathematical modeling

The mathematical model of the electromagnetic actuator is described by the voltage equation and by the motion equation.

The voltage equation is

$$v_{in} = Ri + \frac{\partial \Psi}{\partial i}\frac{di}{dt} + \frac{\partial \Psi}{\partial z}\frac{dz}{dt} \tag{2}$$

where v_{in} is the applied voltage, i is the armature current, Ψ is the armature flux, z is the armature position, and R is the electrical resistance of the coil.

If we note with $v = \dot{z}$, the armature speed and then the equation of the motion can be written as

$$m\ddot{z} = F_S - F_m \tag{3}$$

where m is the moving mass, F_m is the electromagnetic force, and F_S is the spring force. Since the armature displacement often is very short, the spring force can be considered constant. In case of magnetic levitation, the spring force is replaced by the weight of the moving mass.

The electromagnetic force can be expressed based on the electromagnetic co-energy W_{co}:

$$W_{co} = \int_0^i \Psi di \tag{4}$$

$$F_m = -\left.\frac{\partial W_{co}}{\partial z}\right|_{i=ct} \tag{5}$$

Then, we can also write

$$F_m = -\int_0^i \frac{\partial \Psi}{\partial z} di \tag{6}$$

The $\Psi = \Psi(i, z)$ and $F_m = F_m(i, z)$ static characteristics can be measured. The flux-linkage characteristic is derived by integration (very often the current decay test is used). Thus, the flux linkage for one fixed position z is calculated by

$$\Psi(i, z) = \int_0^\infty [v_{in}(t) - R \cdot i(t)]dt \tag{7}$$

where at $t = 0$ and the following conditions hold: $v_{in} = 0$, $i \neq 0$, and $di/dt = 0$.

Although the model does not take into account the effect of eddy currents, the numerical model can be very accurate and might be written formally into a nonlinear form:

$$\dot{x} = f(x) + \sum_{i=1}^{m} g(x)u \tag{8}$$

where $x = [i \ v \ z]^T$ represents the state of the nonlinear system, $u = [v_{in} \ F_S]^T$ is the input vector, and $f(x)$ and $g(x)$ are nonlinear functions of the state x. The output vector y is

$$y = h(x) \tag{9}$$

where $h(x)$ in the most general case is a nonlinear function.

Finally, in the aim to illustrate our investigations, let us consider an electromagnetic actuator with parameters (catalog data) mentioned in **Table 1** [16].

2.1. Nonlinear model and piecewise linearization

The mathematical model described above is too general and is difficult to handle in analytical form. Therefore, we define an analytical model set, which describes the flux-linkage characteristic as

$$\Psi(i, z) = \Psi_{max}\left[1 - \exp\left(-\frac{i}{c_1 + c_2 z}\right)\right] \tag{10}$$

where the parameters of the model set are Ψ_{max}, c_1, and c_2.

Furthermore, the partial derivatives of the flux-linkage are

$$\frac{\partial \Psi}{\partial i} = \frac{\Psi_{max}}{c_1 + c_2 z}\exp\left(-\frac{i}{c_1 + c_2 z}\right) \tag{11}$$

$$\frac{\partial \Psi}{\partial z} = -\frac{\Psi_{max} \cdot c_2 \cdot i}{(c_1 + c_2 z)^2}\exp\left(-\frac{i}{c_1 + c_2 z}\right) \tag{12}$$

The approach presented in this section is reproduced from [17].

Type	**Solenoid valve**
Stroke length	10 [mm]
Operating voltage	24 [V] d.c.
Maximum current	0.6 [A]
Resistance	40 [Ω]
Inductance	0.35–1.1 [H]
Number of turns	2240

Table 1. The solenoid parameters.

If we approximate the exponential term by Taylor series, we have

$$\exp\left(-\frac{i}{c_1 + c_2 z}\right) \approx 1 - \frac{i}{c_1 + c_2 z} + \frac{i^2}{2(c_1 + c_2 z)^2} \tag{13}$$

Thus, the magnetic force—based on the analytical model—can be expressed as

$$F_m \approx \frac{\Psi_{max} \cdot c_2 \cdot i^2}{(c_1 + c_2 z)^2}\left[\frac{1}{2} - \frac{i}{3(c_1 + c_2 z)} + \frac{i^2}{8(c_1 + c_2 z)^2}\right] \tag{14}$$

The model set above is validated against the measured static (flux and force) characteristics. The "dots" in **Figure 4** represent the measured data, and the solid lines represent the calculated model using the above model set, with $\Psi_{max} = 0.45[Wb]$, $c_1 = 0.4[A]$, and $c_2 = 0.375 \cdot 10^3[A/m]$. The above parameters are derived using nonlinear least squares, fitting the measured data (obtained using the current decay test and force measurements) with the analytical model.

Next, let us introduce the following notations, which help us to rewrite the model in a convenient form: $\chi_i = \partial\Psi/\partial i$, $\chi_z = \partial\Psi/\partial z$, and $\chi_f = F_m/i$.

Since the magnetic force F_m depends on the square of the current i^2, when the current is zero $i = 0$ and then $\chi_f = 0$, there is no division by zero in the model.

Thus, the voltage and motion equations are written as

$$\frac{di}{dt} = -\frac{R}{\chi_i} \cdot i - \frac{\chi_z}{\chi_i} \cdot v + \frac{1}{\chi_i} v_{in} \tag{15}$$

$$\frac{dz}{dt} = v \tag{16}$$

$$\frac{dv}{dt} = -\frac{\chi_f}{m} \cdot i - \frac{k}{m} \cdot z + \frac{1}{m} F_S(0) \tag{17}$$

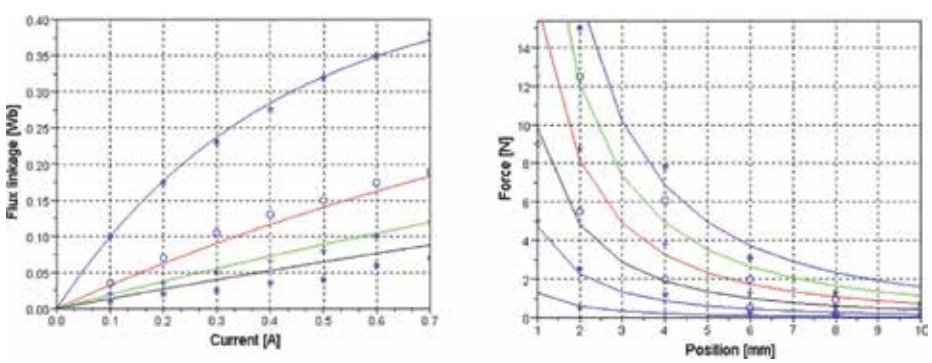

Figure 4. Flux and force characteristics.

Finally, using a piecewise approximation, the system can be written in state-space form as

$$\begin{aligned} \dot{x} &= A(i,z) \cdot x + B(i,z) \cdot u \\ y &= C \cdot x \end{aligned} \tag{18}$$

where $x = [i \;\; z \;\; v]^T$ is the state-space vector, $u = [v_{in} \;\; F_S(0)]^T$ is the input vector, y is the output vector, the $A(i,z)$ and $B(i,z)$ are current and position dependent matrices and $C = [1 \;\; 1 \;\; 0]$ if the armature current and position are sensed. We remark, that in practice sensing the armature speed and/or positions with sensor(s) might be expensive solution. Therefore, often only the armature current can be sensed in a cost-effective manner.

The terms $A(i,z)$ can be written as

$$A(i,z) = \begin{bmatrix} -R/\chi_i & 0 & -\chi_z/\chi_i \\ 0 & 0 & 1 \\ -\chi_f/m & -k/m & 0 \end{bmatrix} \tag{19}$$

where

$$-\frac{\chi_z}{\chi_i} = \frac{c_2 \cdot i}{c_1 + c_2 z} \tag{20}$$

The term $B(i,z)$ can be written as

$$B(i,z) = \begin{bmatrix} 1/\chi_i & 0 \\ 0 & 0 \\ 0 & 1/m \end{bmatrix} \tag{21}$$

where

$$\frac{1}{\chi_i} \approx \frac{2(c_1 + c_2 z)^2 + 2i(c_1 + c_2 z) + i^2}{2 \cdot \Psi_{max} \cdot (c_1 + c_2 z)} \tag{22}$$

or a coarser approximation will be

$$\frac{1}{\chi_i} \approx \frac{c_1 + c_2 z + i}{\Psi_{max}} \tag{23}$$

Last but not least, the armature movement is subject to the following constraints:

$$v(t) = \begin{cases} 0 & if \quad z \geq z_{max} \quad and \quad F_s - F_m \geq 0 \\ 0 & if \quad z \leq 0 \quad and \quad F_s - F_m \leq 0 \end{cases} \tag{24}$$

as well as $z_{min} \leq z(t) \leq z_{max}$, where z_{min} and z_{max} are the minimum and maximum displacements of the armature.

2.2. Linearized mathematical model

From control engineering viewpoint—in case of some applications (e.g., magnetic levitation)—the piecewise linearized model might be too sophisticated. Therefore, in this section a linearized mathematical model around an operating point is derived [1, 18].

Let us approximate the magnetic force as

$$F_m \approx \gamma \frac{i^2}{(c_1 + c_2 z)^2} \tag{25}$$

where γ is a constant.

The equation of motion can be written as

$$M(z, \ddot{z}, i) = m\ddot{z} - F_s + \gamma \frac{i^2}{(c_1 + c_2 z)^2} = 0 \tag{26}$$

The equation above can be linearized around an operating point $p_0 = (z_0, \ddot{z}_0, i_0)$ as follows:

$$M(z, \ddot{z}, i) = M(z_0, \ddot{z}_0, i_0) + \left.\frac{\partial M}{\partial z}\right|_{p_0}(z - z_0) + \left.\frac{\partial M}{\partial \ddot{z}}\right|_{p_0}(\ddot{z} - \ddot{z}_0) + \left.\frac{\partial M}{\partial i}\right|_{p_0}(i - i_0) \tag{27}$$

which can be further written as

$$M(z, \ddot{z}, i) = -\frac{2\gamma i_0^2}{(c_1 + c_2 z_0)^3}(z - z_0) + m(\ddot{z} - \ddot{z}_0) + \frac{2\gamma i_0}{(c_1 + c_2 z_0)^2}(i - i_0) = 0 \tag{28}$$

If we denote with $\Delta z = z - z_0$ and $\Delta i = i - i_0$, we obtain

$$-\frac{2\gamma i_0^2}{(c_1 + c_2 z_0)^3}\Delta z + m\Delta\ddot{z} + \frac{2\gamma i_0}{(c_1 + c_2 z_0)^2}\Delta i = 0 \tag{29}$$

If we divide the equation with the moving mass m and apply the Laplace transform, we obtain

$$\left(s^2 - a^2\right)\Delta z(s) + k\Delta i(s) = 0 \tag{30}$$

$$\frac{\Delta z(s)}{\Delta i(s)} = -\frac{k}{s^2 - a^2} = -\frac{k}{(s - a)(s + a)} \tag{31}$$

where k and a are varying with the equilibrium point (i_0, z_0):

$$k = \frac{2\gamma i_0}{m(c_1 + c_2 z_0)^2} \tag{32}$$

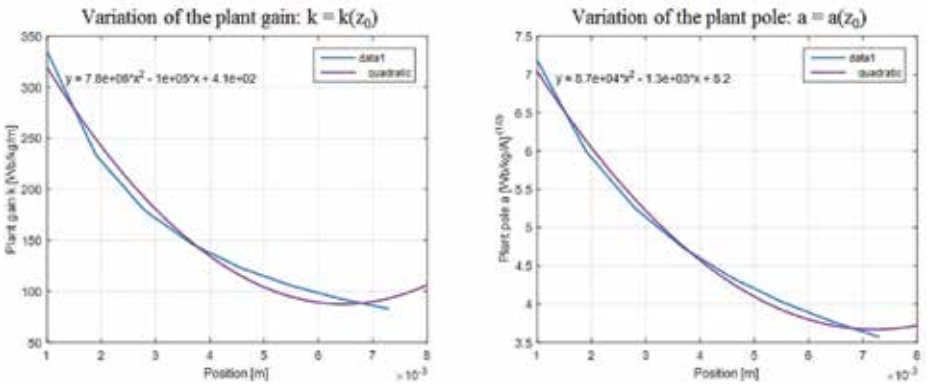

Figure 5. Plant gain and pole variation with the equilibrium position.

$$a^2 = \frac{2\gamma i_0^2}{m(c_1 + c_2 z_0)^3} \tag{33}$$

It means that a family of transfer functions are obtained and the system can be viewed as a linear parameter-varying (LPV) system.

The variation of k and a values with the equilibrium position z_0 is shown in **Figure 5** and can be well approximated by quadratic functions.

3. System identification

3.1. Clustering-based system identification

In the previous section, we have seen that using the current decay test and the nonlinear least squares method, the parameters of the mathematical model can be identified.

However, the current decay test is time-consuming, since measurements shall be performed for each grid point defined by armature current and position (i, z). Thus, the obvious question might arise: is there a faster solution to identify the parameters?

During the system identification process, we will note the system's input and output at time t by $u(t)$ and $y(t)$, respectively [19].

For single-input single-output linear systems, we can write

$$y(t) = \varphi^T(t)\theta \tag{34}$$

where θ is the parameter vector (unknown) and the φ is the recorded (known) input-output data vector:

$$\begin{aligned} \theta &= [a_1 \ldots a_n \qquad\qquad b_0 \ldots b_m]^T \\ \varphi(t) &= [-y(t-1) \ldots -y(t-n) \quad u(t) \ldots u(t-m)]^T \end{aligned} \tag{35}$$

To emphasize that the calculation of the $y(t)$ is from the past data, we will write

$$\widehat{y}(t) = \varphi^T(t)\theta \tag{36}$$

Now, suppose for a given system that we do not know the values of the parameters in θ, but we have recorded inputs and outputs over the time interval. If the input signal is persistently exciting—condition described in details in [19, 20]—then the solution can easily be computed by modern software tools.

In this section a clustering-based identification method, proposed by Ferrari-Trecate et al. (2003) is used (see [21, 22]), where the plant is assumed to be described by piecewise linear models having s sub-models, such as

$$y(t) = \begin{cases} \varphi^T(t)\theta_1 + w(t), & if \quad \varphi^T(t) \in C_1 \\ \qquad \vdots \\ \varphi^T(t)\theta_s + w(t), & if \quad \varphi^T(t) \in C_1 \end{cases} \tag{37}$$

where $w(t)$ is white noise, θ_i $i = 1, \ldots, s$ are the parameter vectors, $\varphi(t)$ is a regression vector, and n is the order of the piecewise ARX (PWARX) model.

It is assumed that the order of each sub-model is the same, and u(t) and y(t) are the input and output, respectively.

Furthermore, it is assumed that $C_{i=1}^s$ are polytopic and they satisfy the well-posed condition: $\cup_{i=1}^s C_i = C$, $C_i \cap \ C_j = \varnothing$, and $\forall i \neq j$.

An important phase of the system identification experiment is input signal design. In case of nonlinear systems, a multilevel random signal is often used [23, 24], and a bi-level pseudorandom binary signal (PRBS) is not suitable for nonlinear systems.

The generation of the multilevel random signal—using shift registers—is done according to [25]. **Figure 6** shows a five-level random signal with maximal length, using four-shift registers with coefficients $a_1 = 1, a_2 = -1, a_3 = 1, a_4 = -2$ [25].

This input signal is applied—when the armature is fixed—in order to identify the dynamic inductance denoted by χ_i and the electrical resistance R. The output signal—armature current —when the multilevel random signal is applied is shown in **Figure 6**.

Next, the voltage equation is written in discrete form at the time moment $t = t(k)$:

$$i(k) = \frac{T_S}{\chi_i + RT_S} v_{in}(k) + \frac{\chi_i}{\chi_i + RT_S} i(k-1) \tag{38}$$

where T_S is the sampling time.

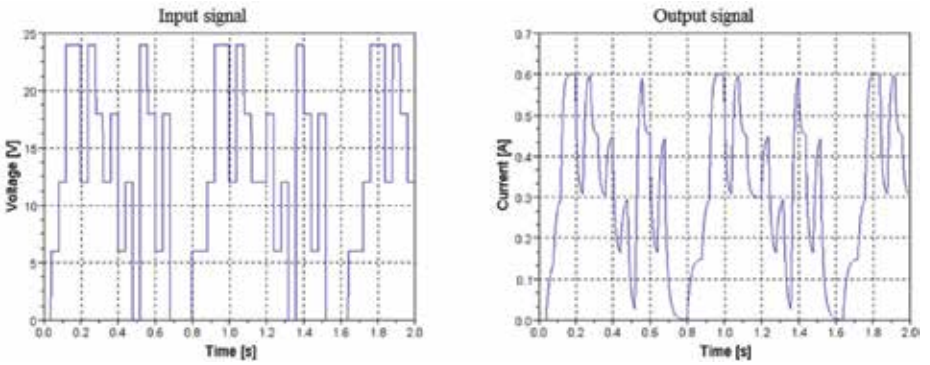

Figure 6. Multilevel random input and corresponding output signal.

The equation above defines the regression space (see also references [21, 22]) having in this case two axis, defined by $i(k-1)$ and $v_{in}(k)$. The data collected during the system identification experiment is shown in the regression space in **Figure 7**.

The regression space is clustered in five different regions for $i = 0.1, \ldots, 0.5[A]$, and the parameters are identified for each case using the least squares method. In each defined cluster, we assume that χ_i is constant, and basically we use a piecewise linear approximation of χ_i.

The system identification experiments are repeated around different positions, when the armature is fixed; thus, the function $\widehat{\chi}_i = \widehat{\chi}_i(i, z)$ can be estimated.

Now, using the nonlinear least squares, we can minimize the J objective function:

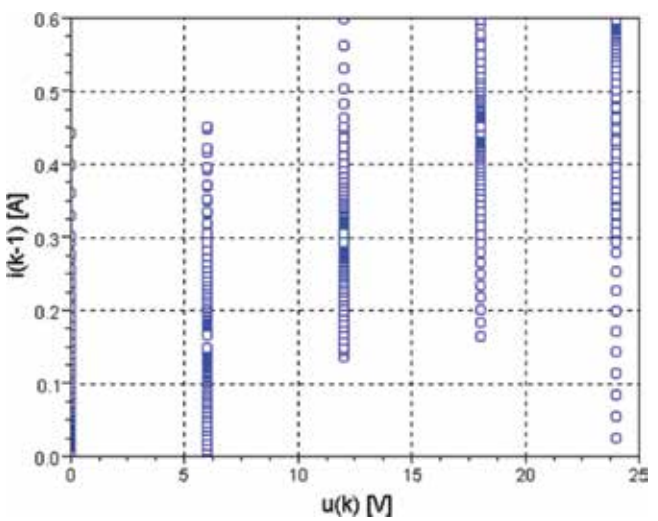

Figure 7. Regression space—Clustering-based identification.

$$J = \min(\chi_i(i,z) - \widehat{\chi}_i(i,z))^2 \tag{39}$$

and we can find out the estimated parameters of the model $\widehat{\Psi}_{max} = 0.437[Wb]$, $\widehat{c_1} = 0.37[A]$, and $\widehat{c_2} = 0.36 \cdot 10^3[A/m]$. Values, which are in good accordance with the values, are found via the current decay test.

Having the $\chi_i = \chi_i(i,z)$ function identified, the parameters of the model set, namely, Ψ_{max}, c_1, and c_2, are found.

This identification is repeated only around different positions z, when the armature is fixed and thus is much faster than identifying $\Psi = \Psi(i,z)$ around different current and position values using the current decay test.

3.2. Identification under closed-loop

In practice, it might be the case that the system is open-loop unstable; thus, system identification experiments have to be performed under closed-loop (for more details see [26, 27]).

Closed-loop identification is a very challenging task. Due to the presence of feedback loop, the input signal might not be persistently exciting. In the aim to achieve a persistent excitation of the system, it is recommended in [19] to switch between different simple controller structures.

First, the system shall be stabilized under feedback around an equilibrium position, as shown in **Figure 8**; details about the controller design $K(s)$ are described in the next section.

Under closed loop, the reference input (armature position) is disturbed by a persistently exciting input signal (i.e., pseudorandom binary signal)—as shown in **Figure 9**, and three linear transfer functions are identified, which are defined as

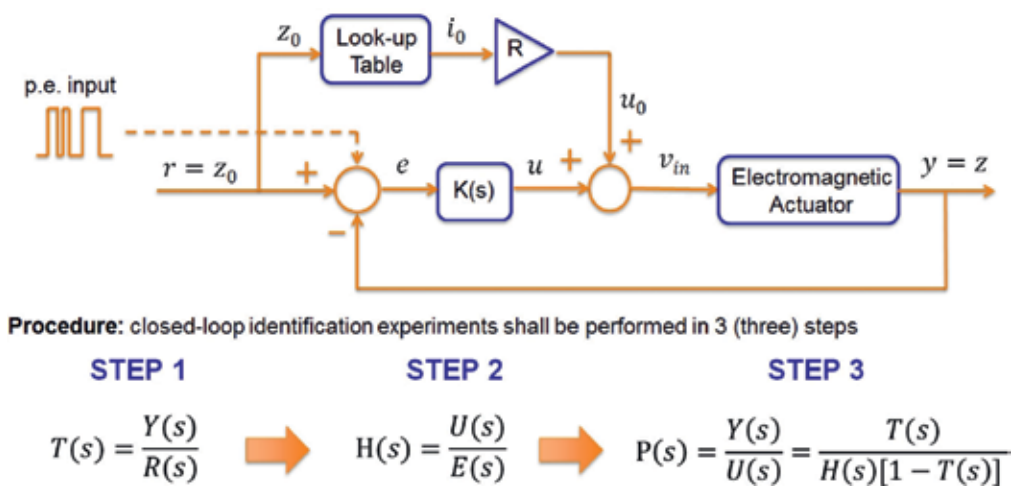

Figure 8. Closed-loop system identification.

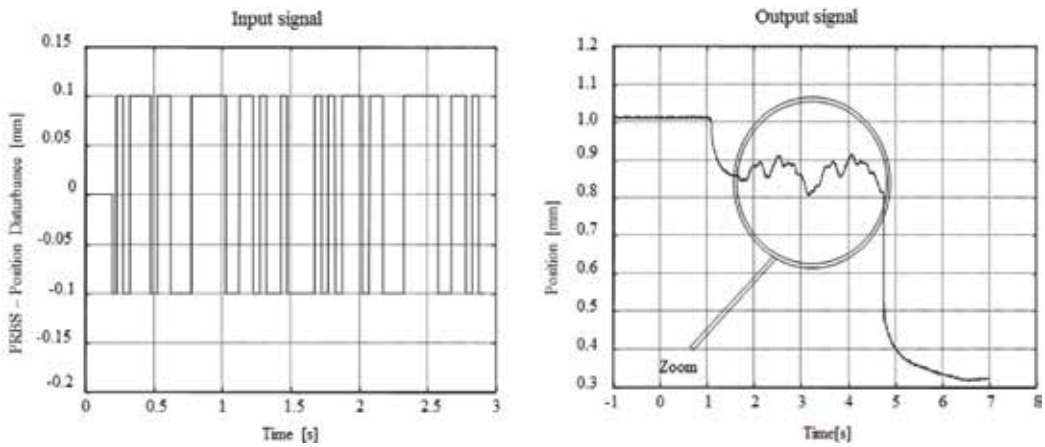

Figure 9. Input and output signal used to identify $T(s)$.

$$T(s) = \frac{Y(s)}{R(s)} = \frac{P(s)K(s)}{1 + P(s)K(s)} \tag{40}$$

$$H(s) = \frac{U(s)}{E(s)} = \frac{K(s)}{1 + P(s)K(s)} \tag{41}$$

$$P(s) = \frac{Y(s)}{U(s)} = \frac{T(s)}{H(s)(1 - T(s))} \tag{42}$$

where we used the well-known identity $S(s) + T(s) = 1$:

$$S(s) = \frac{E(s)}{R(s)} = 1 - T(s) \tag{43}$$

The procedure can be repeated around different equilibrium positions; thus, a family of transfer functions can be obtained.

4. Control of electromagnetic actuators

Let us start with the easier case: the moving armature is controlled around an equilibrium position—magnetic bearings and magnetically levitated high-speed trains are typical applications.

The linearized mathematical model, around an equilibrium position, can be written as

$$P(s) = \frac{\Delta z(s)}{\Delta i(s)} = -\frac{k}{(s - a)(s + a)} \tag{44}$$

where k and a are strictly positive values, varying with the equilibrium point (i_0, z_0).

In this section, we are looking for a linear controller, which can stabilize the plant and can fulfill performance and robustness requirements [18].

4.1. PD controller

A very simple PD controller, which can stabilize the plant, is

$$K(s) = -k_D(s + a) \tag{45}$$

The closed-loop transfer function shows that

$$T(s) = \frac{kk_D}{s + kk_D - a} \tag{46}$$

The system is stable if $kk_D > a$; however, the steady-state error might be significant, since the controller gain k_D cannot be made arbitrarily large.

4.2. PI controller

The next option is to consider a PI controller such as

$$K(s) = -k_{PI}\frac{s + a}{s} \tag{47}$$

In this case, the closed-loop transfer function becomes

$$T(s) = \frac{kk_{PI}}{s^2 - as + kk_{PI}} \tag{48}$$

Since a is a positive value, we observe that the PI controller cannot stabilize the plant $P(s)$.

4.3. PID controller

Let us consider a PID controller—having a single tuning parameter K_{PID}—in the form

$$K(s) = -k_{PID}\frac{(s + a)^2}{s} \tag{49}$$

The block diagram of the control system is shown in **Figure 10**.

The closed-loop transfer function is

$$T(s) = \frac{kk_{PID}(s + a)}{s^2 + (kk_{PID} - a)s + kk_{PID}a} \tag{50}$$

The closed-loop transfer function has a zero at $s = -a$, which might affect the system response (large overshoot), which can be canceled with a prefilter $K_{PRE}(s) = a/(s + a)$.

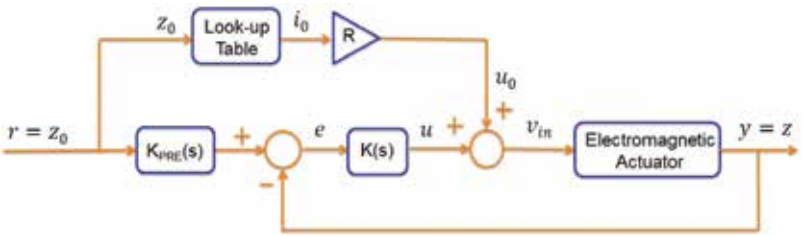

Figure 10. The block diagram of the control system.

Then, the closed-loop transfer function becomes

$$T(s) = \frac{kk_{PID}a}{s^2 + (kk_{PID} - a)s + kk_{PID}a} \tag{51}$$

Next, based on performance and robustness specifications, we would like to find a suitable value for the controller gain K_{PID}. Usually, performance specifications are given in terms of settling time T_{set} and percent of overshoot $P.O.$

For a second-order system

$$T(s) = \frac{\omega_n^2}{s^2 + 2\tau\omega_n s + \omega_n^2} \tag{52}$$

where ω_n is the natural frequency and the τ is the damping factor; we have $T_{set} \approx 4/(\tau\omega_n)$ and $P.O. = 100 \cdot e^{-\tau\pi/\sqrt{1-\tau}}$.

Since we have only one tuning parameter K_{PID}, the performance specifications are given only in terms of settling time $T_{set} = 1.25[s]$. Therefore, the PID controller gain can be calculated as

$$kk_{PID} - a = 2\tau\omega_n \approx \frac{8}{T_{set}} \tag{53}$$

Thus, we obtain

$$k_{PID} = \frac{8 + aT_{set}}{kT_{set}} \tag{54}$$

Next, the stability and robustness in a classical framework can be assessed. We calculate the gain and phase margins, obtaining $G_m = 0.47[m/A]$ and $P_m = 37[\text{deg}]$ for the equilibrium position $z_0 = 3 \cdot 10^{-3}[m]$.

4.4. Gain-scheduled controller

We have seen that the actuator can be stabilized around, and equilibrium point and performance and robustness can be guaranteed.

However, we observed that the plant parameters k and a are varying with the operating point (i_0, z_0); thus, for good performance and robustness, the controller should take into account that the plant parameters are varying.

A survey of linear parameter-varying control applications can be found in [28], and control applications validated by experiments are presented in [27, 29] for actuators and for medical X-ray systems in [30]. High-accuracy mathematical modeling and a linear parameter-varying observer for fault detection and fault isolation are presented in [17].

We can design a linear parameter-varying controller having the form

$$K(s, z_0) = k_{PID}(z_0)\frac{(s + a(z_0))^2}{s} \tag{55}$$

where both the controller gain and controller zero are dependent on the equilibrium position.

Finally, stability and robustness (quadratic stability) of such a control system can be analyzed using modern software tools, and details are described in [27].

If a simpler approach is preferred, a gain-scheduled controller might be a good choice, which is easier to implement in real time, and its stability and robustness are easier to analyze.

Since perfect cancelation of the varying plant pole at $s = -a$ with a fixed controller zero is not possible, we choose to place the controller fixed zero left to the varying poles, such as $z = -a_{max}$. Then, the gain-scheduled controller can be written as

$$K(s, z_0) = k_{PID}(z_0)\frac{(s + a_{max})^2}{s} \tag{56}$$

where the only one tuning parameter is controller gain $K_{PID}(z_0)$, defined as

$$k_{PID}(z_0) = \frac{8 + a(z_0)T_{set}}{k(z_0)T_{set}} \tag{57}$$

where the variation of the values $k = k(z_0)$ and $a = a(z_0)$ were shown already in **Figure 5**.

Next, the gain and phase margins are calculated for different equilibrium positions z_0 and shown in **Figure 11**. We can observe that—due to the gain-scheduled controller—the gain and phase margins do not change significantly with the equilibrium position, and such a robustness is difficult to achieve with a single controller, having fixed parameters.

The system response using the gain-scheduled controller is investigated, considering the following two cases:

- The moving armature is controlled around an equilibrium position, and the set point (reference position) is changed $\Delta z_0 = 1[mm]$ (see **Figure 12**, left plot). The control system —including the prefilter—exhibits approximately $P.O. \approx 25\%$ overshoot and settling time $T_{set} = 1.5[s]$.

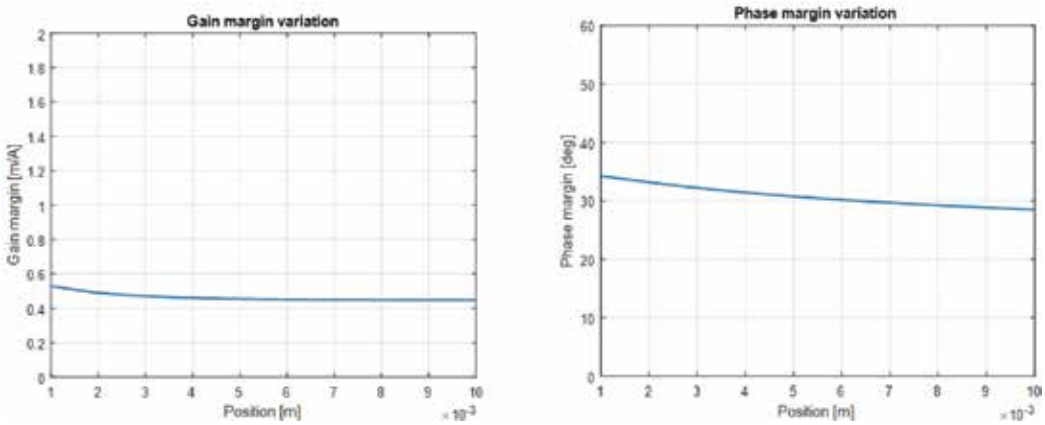

Figure 11. Gain and phase margin variation with z_0.

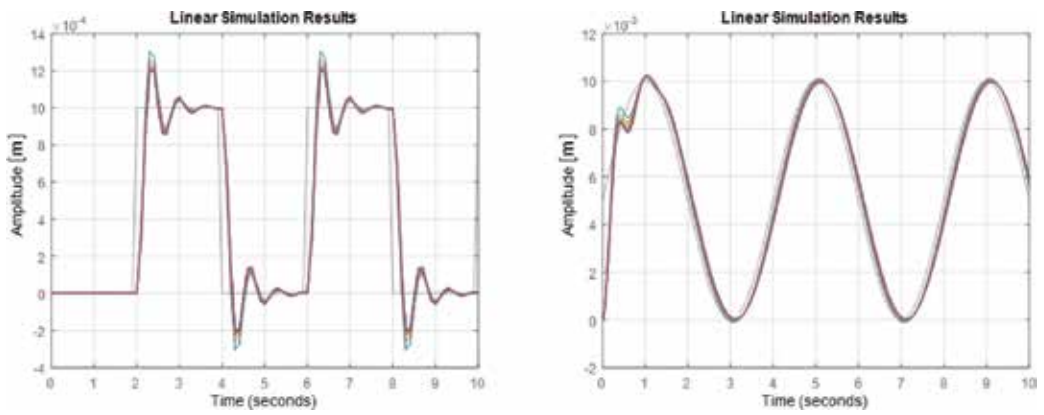

Figure 12. System response with the gain-scheduled controller.

- The moving armature is controlled between the two extreme positions, armature open and armature close, $\Delta z_0 = 10[mm]$ (see **Figure 12**, right plot). In this case the main goal is to achieve so-called soft landing of the moving armature to reduce wear and noise.

It is important to highlight that controller design is made based on the linearized plant, but validation of the controller in simulations or during hardware-in-the-loop (HIL) experiments shall be done using the nonlinear plant model.

During our control design investigations, we considered that the armature position can be measured. In practice, there are applications, where the armature position cannot be measured in a cost-effective way.

Therefore, we remark that controlling the moving armature without measuring the armature position (e.g., measuring only the current) remains a challenging research topic, which exceeds the goals and the limits of this chapter.

5. Conclusions

This chapter dealt with mathematical modeling, system identification, and control of electromagnetic actuators. Actuators are often used in industrial applications such as magnetic levitation, electromagnetic bearings, as well as in fuel injectors in the automotive industry.

After a detailed mathematical model was presented, two different parameter identification techniques were described. The first one is based on the classical current decay test, and the second one is a clustering-based system identification approach. Since the actuator is open-loop unstable, the main steps of system identification of the actuators under closed-loop control were presented.

Finally, very simple and easy-to-apply control strategies were discussed, when the armature is controlled around a fixed equilibrium position (PID controller) as well as when the armature is controlled between two extreme positions, armature open and armature closed (gain-scheduled PID controller).

Author details

Alexandru Forrai

Address all correspondence to: alexandru.forrai@tno.nl

TNO, Helmond, The Netherlands

References

[1] Bittar A, Sales RM. H_2 and H_∞ control for MagLev vehicles. IEEE Control Systems. 1998; **18**(4):18-25

[2] Lindlau JD, Knospe CR. Feedback linearization of an active magnetic bearing with voltage control. IEEE Transaction on Control Systems Technology. 2002;**10**(1):21-31

[3] Li L, Shinshi T, Shimokohbe A. Asymptotically exact linearizations for active magnetic bearing actuators in voltage control configuration. IEEE Transaction on Control Systems Technology. 2003;**11**(2):185-195

[4] Fittro RL, Knospe CR. Rotor compliance minimization via μ-control of active magnetic bearings. IEEE Transaction on Control Systems Technology. 2002;**10**(2):238-250

[5] Duan G-R, Howe D. Robust magnetic bearing control via eigenstructure assignment dynamical compensation. IEEE Transaction on Control Systems Technology. 2003;**11**(2): 204-215

[6] http://mechanicstips.blogspot.nl/2015/06/

[7] http://www.personal.psu.edu/cjm5/

[8] Yaghoubi H, Barazi N, Aoliaei MR: Maglev. In: Infrastructure design, signalling and security in railway. InTechOpen, pp. 123-176

[9] https://www.dieselnet.com/tech/diesel-fi.php

[10] Robert Bosch GmbH. Diesel-Engine Management. Plochingen: Bosch; 2004

[11] Breitbach H. Fuel Injection Systems Overview. Delphi Corporation; 2002

[12] http://www.bosch-mobility-solutions.com/en

[13] Hoffmann W, Peterson K, Stefanopoulou A. Iterative learning control for soft landing of electromechanical valve actuator in camless engines. IEEE Transaction on Control Systems Technology. 2003;**11**(2):174-184

[14] Doosje E, Willems F, Baert R. Experimental demonstration of RCCI in heavy-duty engines using diesel and natural gas. SAE Technical Paper 2014-01-1318; 2014. DOI: 10.4271/2014-01-1318

[15] Mikulski M, Balakrishnan PR, Doosje E, Bekdemir C. Variable valve actuation strategies for better efficiency, load range, and thermal management in an RCCI engine. SAE Technical Paper 2018-01-0254; 2018 (to be published)

[16] Rahman MF, Cheung NC, Lim KW. Modelling of a nonlinear solenoid towards the development of a proportional actuator. Vol 1. In: Proceedings of the 5th International Conference on Modelling and Simulation of Electrical Machines, Convertors, and Systems, ELECTRIMACS'96; Saint Nazaire. September 17–19, 1996; pp. 121-128

[17] Forrai A. System identification and fault diagnosis of an electromagnetic actuator. IEEE Transaction on Control Systems Technology. 2016;**25**(3):1028-1035

[18] Folea S, Muresan CI, De Keyser R, Ionescu CM. Theoretical analysis and experimental validation of a simplified fractional order controller for a magnetic levitation system. IEEE Transaction on Control Systems Technology. 2016;**24**(2):756-763

[19] Ljung L. System Identification – Theory for the User. New York: Prentice-Hall; 1987

[20] Forrai A. Embedded Control System Design – A Model Based Approach. Berlin/Heidelberg: Springer; 2012

[21] Ferrari-Trecate G, Muselli M, Liberati D, Morari M. A clustering techniques for the identification of piecewise affine systems. Automatica. 2003;**39**(2):205-217

[22] Hirata M, Noguchi S, Adachi S. A hybrid modeling method for precise positioning systems. In: Proceeding of the 17th World Congress. Seoul: The International Federation of Automatic Control; 2008. pp. 1797-1802

[23] Barker HA, Rivera DE, Tan AH, Godfrey KR. Perturbation signal design. In: 14th IFAC Symposium on System Identification; 2006. pp. 1121-1126

[24] Ljung L. Approaches to identification of nonlinear systems. In: Proceedings of 29th Chinese Control Conference, Beijing; 2010

[25] Haber R, Keviczky L. Nonlinear System Identification. Berlin: Springer; 1999

[26] Forrai A, Ueda T, Yumura T. Asymptotically exact linearization and robust control of an electromagnetic actuator. Vol. II. In: Proceedings of PCIM'04 Conference, Nuremberg; 2004. pp. 788-793

[27] Forrai A, Ueda T, Yumura T. Electromagnetic actuator control: A linear parameter-varying (LPV) approach. IEEE Transaction on Industrial Electronics. 2007;**54**(3):1430-1441

[28] Hoffmann C, Werner H. A survey of linear parameter-varying control applications validated by experiments or high-fidelity simulations. IEEE Transaction on Control Systems Technology. 2015;**23**(2):416-433

[29] Kahveci NE, Kolmanovsky IV. Control design for electromagnetic actuators based on backstepping and landing reference governor. In: 5th IFAC Symposium on Mechatronic Systems; 2010. pp. 393-398

[30] van der R, van der Maas A, Voorhoeve R, Oomen T. Accurate FRF identification of LPV systems: nD-LPM with application to a medical X-ray system. IEEE Transaction on Control Systems Technology. 2017;**25**(5):1724-1735

Section 3

Medical Applications

Chapter 6

Quantitative Tactile Examination Using Shape Memory Alloy Actuators for the Early Detection of Diabetic Neuropathy

Junichi Danjo, Sonoko Danjo, Hideyuki Sawada,
Keiji Uchida and Yu Nakamura

Additional information is available at the end of the chapter

http://dx.doi.org/10.5772/intechopen.75084

Abstract

Diabetic neuropathy (DPN) is asymptomatic in its early phases but can cause serious complications as it progresses. Most DPN tests are cumbersome and produce only qualitative assessments, and simpler approaches that yield quantitative results are needed. Techniques that allow patients to perform examinations themselves would be especially valuable. In this study, we focused on quantifying the decline in tactile sensation associated with DPN and developed a measurement device that used a thin shape memory alloy (SMA) wire as the actuator. An ON/OFF pulse current caused the wire to shrink and expand. This vibration was amplified by a round-headed pin, allowing even DPN patients with reduced tactile sensitivity to detect the stimuli generated when lightly touching the pin with their fingertips. The tactile stimuli were ranked into 30 levels of intensity. A key advantage of the device is that it can be used by patients themselves, returning quantified results within minutes. Although developed for DPN, the method can be applied to the detection of peripheral neuropathy in general.

Keywords: shape memory alloy actuator, neuropathy, tactile application, quantification, quantitative tactile examination, early detection

1. Introduction

In this chapter, we introduce a quantitative tactile examination device using shape memory actuators and discuss previous work by the authors on the use of such a system for the early

detection of diabetic neuropathy (DPN) [1–3]. We consider the range of potential applications and the future potential of this technology.

We have conducted a number of studies on tactile sense-presentation technology that applies micro-vibrations using thin shape memory alloys (SMA) [1–11]. The SMA allows for a compact device that consumes little power and causes no pain to patients.

Tactile-stimulus diagnostic techniques, such as the technique reported in this study, may be possible with other actuators such as small motors [12, 13], piezoelectric actuators [14], or pneumatic actuators [15]. However, each of these technologies requires large electromagnetic devices that require more power than that provided by a portable battery.

Piezoelectric actuators need a driving voltage of the order of several tens of volts, and their inclusion of mechanical parts makes their application in portable devices difficult [14].

Our tactile-stimulus presentation technology that uses a thin SMA avoids the problems of size and power consumption. The present iteration of the device can be driven with a small battery [2, 3, 5–7].

Quantitative diagnosis of DPN at present requires a machine costing at least several million yen and larger than 1 m on a side, such as nerve-conduction studies. Equipment for these tests, in addition to being cumbersome and expensive, requires skilled technicians for its operation.

Some patients refuse a second examination because nerve conduction studies and electromyography studies can be quite painful. Many asymptomatic diabetes patients are left untreated because of the cost, difficulty, and pain caused by the current methods for quantitative diagnosis of the neurological effects of diabetes.

In previous studies [1–3, 5–7], we have developed a range of simple, quantitative, and painless examination methods that use SMA, and the present study summarizes those studies and discusses future prospects.

A wide range of conditions contribute to hypoesthesia and/or peripheral nervous disorders, including the administration of anticancer drugs, DPN, vitamin deficiency, vasculitis, polyneuropathy, depression, alcohol dependence, infection, and uremia. However, the progress of the condition is generally slow, and most sufferers are initially unaware of its presence [16].

Peripheral neuropathy tests can be divided into two main types. The first is qualitative and includes the Achilles tendon reflex/vibration test. The second is nerve conduction studies (NCS), which involve complex and painful invasive examinations but provide quantified diagnoses. Both types require medical expertise and judgment and must be conducted by a healthcare professional. Patients have no access to their test results, making them less likely to seek treatment.

Approximately, half of all patients with diabetes contract asymptomatic neuropathy [17]. As the causes of neuropathy are not limited to diabetes mellitus, it is assumed that there are many more asymptomatic neuropathy sufferers. Currently, patients are unable to perceive the condition themselves, and no simple quantification scale is available. Even patients whose condition is treatable may be unaware of its presence and therefore fail to seek treatment.

A simple method for quantitative detection of the asymptomatic condition is therefore needed. By combining medicine and engineering, we developed a quantitative tactile examination device based on detecting the decline in tactile sensation.

The initial study targeted diabetes patients whose condition was associated with deterioration in sensation. The tactile sensation of diabetic patients was found to be lower than that of normal subjects [1, 2] and that of diabetic patients who were not conscious of the decline to be still lower [3].

2. Tactile sensation and diabetic neuropathy

The sense of touch relies on four main tactile receptors in the skin: the Meissner's corpuscle, Merkel disc, Ruffini ending, and Pacinian corpuscle. As shown in **Figure 1**, Merkel discs are located in the epidermis and are approximately 10 μm in diameter. They are used to sense pressure and texture. Meissner's corpuscles are primarily located immediately below the epidermis and are between 30 and 140 μm in length and 40–60 μm in diameter. They are used to sense stroking and fluttering. Ruffini endings are also located in the dermis, have a length of approximately 0.5–2 mm, and are used for the sense stretching of the skin. Pacini corpuscles are located in the subcutis and are approximately 0.5–2 mm in length and 0.7 mm in diameter. Based on their response speed and size, the receptors are given four labels: fast adapting I and II (FA I and FA II) and slow adapting I and II (SA I and SA II).

The receptors are present at different densities in different regions of the human body. **Figure 2** [13] shows the innervation density in the hand, which is where most human tactile recognition takes place. Receptors are particularly dense in the fingers and especially in the tips. Human fingers are therefore sensitive to a range of stimuli. The response of the receptors is closely related to nervous system activity, and the tips of the fingers are therefore also densely supplied with capillary vessels. When a diabetic condition restricts the blood flow in the capillary

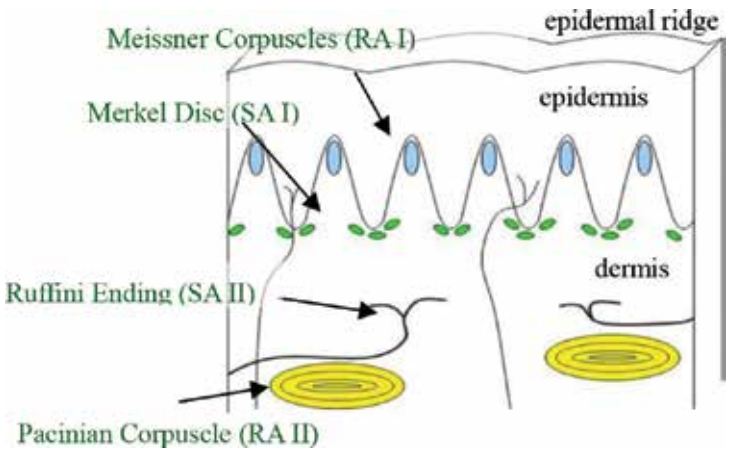

Figure 1. Tactile receptors of the skin [3].

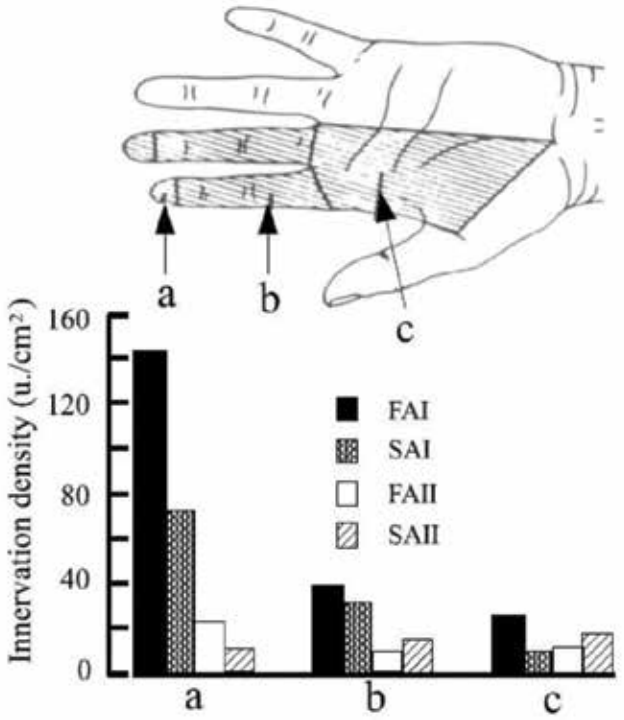

Figure 2. Innervation density of tactile receptors [18].

vessels or destroys them, sensitivity to tactile sensations is restricted. Most diabetes patients, even at an early stage of the disease, have reduced sensitivity to tactile sensations in the fingers and feet. The extent of the decline is a measure of the progress of the condition.

Diabetic neuropathy (DPN) is caused by the degradation of axons in peripheral nerves, which decrease nerve function in slow progression. The rate of degeneration depends on the ability of the patients to control their glycemic index; thus, it varies with each individual. Nerves are distributed throughout the body and vary in function. For that reason, neurological diagnostic methods vary depending on the parts and functions of the nerve distributed, thus making uniform standards difficult to formulate. For example, in the event of dysuria arising from DPN, the patient may consult a urologist. However, a patient who feels discomfort or numbness in the sole of the foot owing to DPN may consult an orthopedist, and both patients may not consult a diabetes specialist until their condition has degraded significantly. DPN presents a variety of symptoms that patients are likely to consult a range of specialists for the same underlying condition. Diagnosis of DPN is so complicated and time-consuming that even many diabetes specialists are not equipped for quantitative studies.

Neuropathy can also be caused by other diseases, but DPN is distinguished by a few symptoms.

DPN presents diffuse neuropathy, with bilateral symmetry. The nerve failure is focused on sensory functions, and DPN tends to progress from peripheral nerves inward.

While examining patients with multiple neuropathy-causing conditions, the underlying cause of any symptom is very difficult to distinguish, with any diagnostic method; thus, this chapter focuses on tactile anomalies and tactile reduction among the neurological abnormalities that could indicate DPN.

To confirm and diagnose the specific form of neuropathy that a patient has developed, an affected nerve must be biopsied from the patient, but this procedure is generally too invasive for the degree of suffering a patient is experiencing. Instead, clinicians administer a series of tests to collate a program similar to quantitative diagnosis and treatment program.

Our tactile test method stimulates the following four main tactile receptors in the skin: the Meissner's corpuscle, the Merkel disc, the Ruffini ending, and the Pacinian corpuscle. Though it may also stimulate other receptors, this device clearly provides a tactile stimulus that at least stimulates the haptic receptors. Precise diagnostic methods require the application of electric current to a patient's nervous system and measuring response. These tests are painful, while our haptic stimulator causes no pain at all. We have not performed biopsy studies to conclusively demonstrate to diagnoses pathologically confirmed with DPN. But we have shown that the device can quickly, inexpensively, and painlessly assess a patient's tactile response with novel technology in some clinical studies [1–3].

In this study, a tactile device was developed that presented present a range of tactile stimuli to the fingers of a subject and then measured the response from the driving parameters of the tactile actuators.

3. Design of the measurement device

3.1. A compact SMA actuator to generate micro-vibrations

To generate the physical stimuli, an SMA wire was employed. Within the typical operating temperature range, SMA has two phases, each with a different crystal structure and therefore different properties. The first is a high-temperature phase, called the Austenite phase, and the second a low-temperature phase, called the Martensite phase. When the temperature exceeds a critical threshold (70°C), the SMA alternates between the two phases, causing the crystal structure, and therefore the shape of the SMA, to change. SMA has been widely used in actuation and sensing applications and in the aerospace, automotive, and biomedical sectors.

When SMA is formed into a thin wire, its length originally 3 mm at a low-temperature phase will change at a known temperature. In the current study, the SMA wire (Toki Corp., BioMetal, BMF75) was used to create a compact actuator, the characteristics of which are shown in **Figure 3**. When the temperature of an SMA wire passes T1 (68°C), the wire begins to shrink up to 5% lengthwise at the temperature T2, reaching a minimum at T2 (73°C). As the temperature is reduced, the wire gradually returns to its initial length.

As the alloy has an electrical resistance of 0.6 ohms per 1 mm, its length can be controlled by supplying a pulse current. This instantaneously increases the temperature, shrinking the wire.

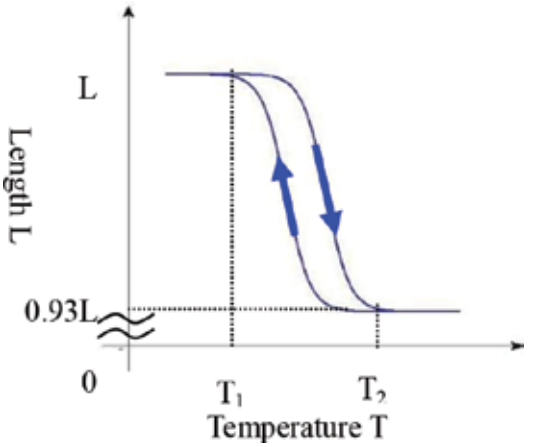

Figure 3. Characteristics of the SMA wire [3].

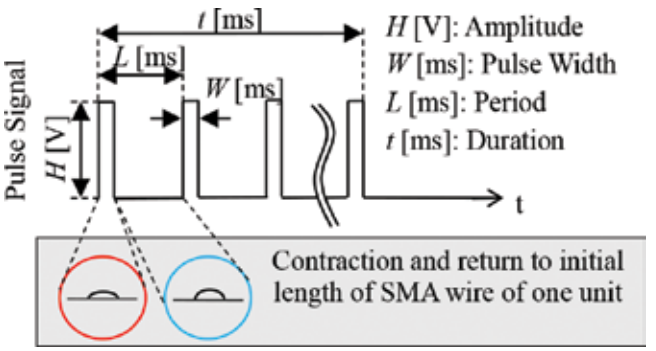

Figure 4. Pulse signal for driving SMA [3].

When the pulse current is halted, the body instantly cools, returning to its initial length. The shrinkage and return are fully synchronized with the ON/OFF pulse current, as shown in **Figure 4**. The magnitude of the vibration created can be precisely controlled by the amplitude of the pulse signal H and the duty ratio W/L. For an efficient operation, the SMA temperature must be maintained within the range T1–T2. In our design, a pulse-width modulated (PWM) rectangular wave signal with an arbitrary frequency, amplitude, and duty ratio is generated by a PC and is then amplified to drive the SMA actuator. The amplifier drives the SMA actuator at frequencies up to 300 Hz. The voltage amplitude is variable and controlled by the current. According to the measurement results of our research so far, the SMA wire shrinks by ~2 μm at the maximum according to the duty ratio of the pulse current. Therefore, according to the duty ratio, the overall length of the SMA wire was observed to be shrinking from 0.1 to 2 μm. The detailed driving pulse signal for each amplitude level of vibration is shown in **Table 1** [3].

While most SMAs have a slow response time, the BMF75 wire with a diameter of 75 μm can respond within less than 1 ms and was used to create the compact vibration actuator.

Amplitude level	W [ms]	L [ms]	H [V]
1	3	200	1.8
2	4	200	1.8
3	6	200	1.8
4	7	200	1.8
5	9	200	1.8
6	10	200	1.8
7	12	200	1.8
8	13	200	1.8
9	15	200	1.8
10	11	75	1.8
11	13	75	1.8
12	15	75	1.8
13	17	75	1.8
14	19	75	1.8
15	22	75	1.8
16	24	75	1.8
17	26	75	1.8
18	28	75	1.8
19	30	75	1.8
20	12	22	1.8
21	15	22	1.8
22	17	22	1.8
23	20	22	1.8
24	22	22	1.8
25	25	22	1.8
26	27	22	1.8
27	29	22	1.8
28	30	22	1.8
29	30	22	1.8
30	30	22	1.8

Table 1. Driving signal for each amplitude level.

The subject only touches the actuator lightly to eliminate the disturbance of the actuator due to the skin reaction force.

The vibration stimulus generated by the SMA wire is transmitted to the subject through the round-head pin (**Figure 5**) described below. The pin actually touched by the subject is shown

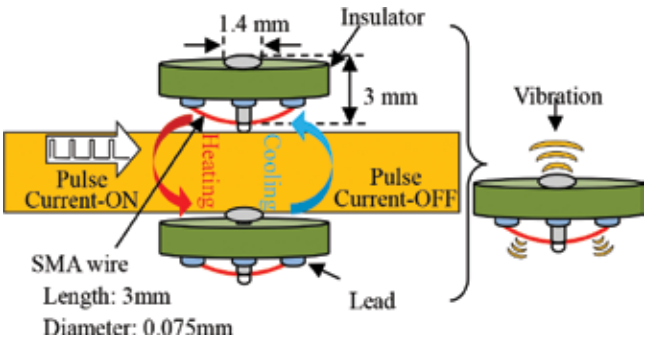

Figure 5. Structure of vibration actuator [3].

in **Figure 6**. As shown in **Figure 6**, the test equipment is shaped in a manner such that the subject can lightly touch the middle and index fingers on the pin array.

Tests were conducted at room temperature, 20–30°C, controlled by air conditioning. We did not use any electromagnetic shielding as the actuator will need to function in unshielded clinical settings.

3.2. Vibration actuator with a round-head pin

To make the actuator usable for tactile screening of diabetes, the micro-vibration generated by the SMA wire required amplification. A round-headed pin was therefore fixed at the center of the SMA wire, transforming the movement of the SMA wire into vibration. As shown in **Figure 5**, the actuator comprised an SMA wire, 75 μm in diameter and 3 mm in length, and a round-headed pin, 1.4 mm in diameter and 3 mm in length.

Shrinking and expansion of the SMA wire was continuously synchronized by the ON/OFF pulse current. This induced vibration in the round-headed pin, allowing even diabetic patients with reduced tactile sensitivity to recognize the tactile stimuli when the vibration pins were brought into light contact with the fingertips.

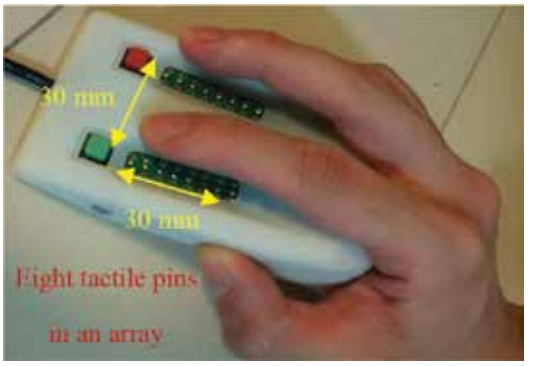

Figure 6. Tactile input for diabetes screening [3].

3.3. Tactile display for the detection of diabetes mellitus

As shown in **Figure 6**, eight actuators were arranged as arrays. Two of these made up the tactile presentation area. The patient placed the index and middle fingers on these in such a way that the tips of two fingers were in contact with the array.

The presentation of vibratory stimuli makes use of higher-level tactile perceptual processes [21]. The pins in each array were driven by the pulse current signals with a time delay, as shown in **Figure 7**. This was expected to create an apparent perception of movement and the subject to experience a vibrating object moving from Ch. 1 (fingertip) to Ch. 8 (the second finger joint). The apparent movement of the stimuli could be controlled by varying the time delay of the pins.

To confirm that perception of apparent movement could be generated, a pilot study was run, using three healthy subjects, in which the frequencies and the amplitudes were varied using different time delays. Based on the results, the amplitude of the vibrations was divided into 30 levels. The lowest amplitude represented a stimulus that was difficult for healthy people with normal tactile sensitivity to perceive, while the strongest could be perceived even by a diabetic subject with severely compromised tactile sensitivity.

As shown in **Figure 4**, the amplitude of vibration was controlled by selecting the parameters W [ms]: pulse width, L [ms]: period, and H [V]: amplitude. These parameter values were carefully selected to allow the vibration to be increased linearly from level 1 to 30 (**Table 1**).

To examine the lowest threshold of tactile sensitivity of the index and middle fingers, a tactile sensation threshold (TST) score or peripheral neuropathy vibration (PNV) score were used. The subject was asked to place the index and middle fingers on the pin arrays. Tactile stimuli were then presented at different frequencies and amplitudes and in randomized directions. Using "yes" or "no" responses, the system measured the threshold of tactile perception and its relationship to the severity of attenuation. We named our proposed method the finger method.

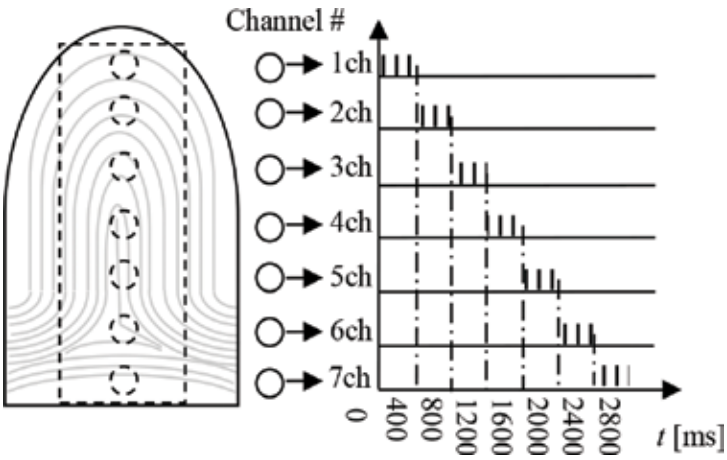

Figure 7. Presentation of tactile vibratory stimuli [3].

3.4. Experimental procedures for detection by diabetes mellitus subjects based on tactile sensation threshold scores

Three different procedures were performed. In the first, tactile stimuli were presented to both fingers simultaneously, in a single direction starting at the fingertips (Pattern 6 in **Figure 8**). Subjects were asked if they had perceived the stimuli. This procedure is known as the tactile sensation threshold 1 direction test (TST-1) or PNV 1 direction test (PNV 1) and was used to investigate the perception of tactile stimuli in two fingers. In the second procedure, a moving stimulus was presented to one of the two fingers in a random direction, and the subject was asked to identify both the finger and the direction of movement. In this procedure, known as the tactile sensation threshold 4 direction test (TST-4) or PNV 4 direction test (PNV 4), the subject was asked to identify the tactile perception as matching one of the four patterns shown in **Figure 8**. In the third procedure, known as the tactile sensation threshold 8 direction test (TST-8) or PNV 8 direction test (PNV 8), stimuli moving in random directions were applied to one or both fingers, and the subject was asked to match the finger(s) and direction of movement with one of the same eight patterns.

In all procedures, the examination began at a stimulus intensity of 15. Based on the accuracy of the answer given, the next round started at an intensity of 22 or 7.

Again, based on the accuracy of the answer given, in the next round, a stimulus intensity of 26, 19, 11, or 4 was presented to the subject. The stimulus intensity was then changed until the subject gave a correct answer 66.7% or more of the time. This TST score or PNV score was defined as the tactile threshold. The value for the tactile threshold was defined as the lowest value among the 30-stage stimulus intensity in which subjects were able to correctly answer more than 66.7%.

To reduce the examination time as much as possible, we applied a protocol to stimuli levels in 30 successive stages.

In our preliminary research on healthy subjects, we gradually increased the stimuli intensity from the weakest stimulus to the strongest. Inspecting patients with obvious neurological

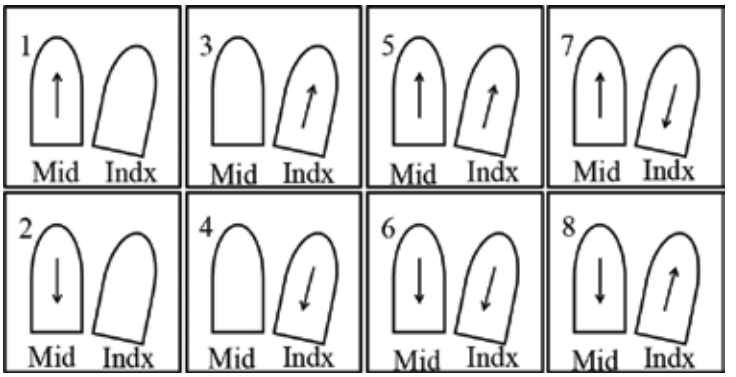

Figure 8. Eight patterns of moving directions of tactile stimuli [3]. Mid = middle finger; Indx = index finger.

disorders in this fashion leads to patient fatigue and boredom, and we cannot expect to see any response for the weakest stimuli. Therefore, we developed a protocol to shorten the inspection time. We began examining all subjects at the middle stimulus intensity of 15. The test stimulus was presented to the subject two or three times. Only subjects who correctly answered 66.7% or more with the test stimulus, that is, examinees who correctly answered at least twice, are next presented with stimulus intensity of 7, which is halfway between the minimum and middle intensities. Subjects who do not detect a stimulus at intensity 15 are presented next with a stimulus intensity of 22. This process significantly reduces the time needed to determine a subject's reaction threshold. Ultimately, the lowest stimulus intensity that was detected more than two-thirds of the presented intensity was defined as the tactile threshold for that subject.

4. Verification of early detection of DPN

4.1. Pilot study to confirm tactile reduction in long-term diabetic patients

The device was first used in a pilot study of 15 diabetic patients with a long history of treatment, and a significant decrease in tactile sensation compared with healthy subjects was confirmed [1].

4.2. Validation of DPN evaluation for diabetic patients

The device was next used to validate the evaluation of DPN in diabetic patients [2]. Based on the criteria [19] for diagnosis of DPN provided by the American Diabetes Association (ADA), tactile sensation was quantified, and a comparison was made of patients with and without DPN. A significant reduction in tactile sensitivity was confirmed in the DPN group.

The goal of this part of the study was to investigate the effectiveness of the proposed method in diagnosing DPN.

A cross-sectional study was conducted of 52 type 2 diabetic outpatients. Patients were evaluated for DPN using the ADA criteria, the Michigan Neuropathy Screening Instrument (MNSI), and our proposed finger method. Patients were assigned to probable DPN or non-DPN groups, based on the ADA criteria. The finger method was used to produce a PNV score from the index and middle fingers, using the three procedures introduced above: PNV 1, PNV 4, and PNV 8. The scores ranged from 1 to 30, and comparisons were made between the two groups.

The PNV scores of the DPN group were significantly higher ($P < 0.01$). The PNV scores for the right fingers of the DPN and non-DPN groups were 10.2 ± 7.4 and 3.4 ± 3.3 in PNV 1, 20 ± 4.9 and 10.7 ± 5.3 in PNV 4, and 23.2 ± 4.9 and 14.6 ± 7.8 in PNV 8, respectively (**Table 2**).

Overall, the tactile threshold of the DPN group was higher than that of the non-DPN group.

The results suggested that the finger method, performed using the proposed device, can be used to evaluate DPN.

	Non-DPN group (N = 21)	DPN group (N = 31)	P-value
Neuropathic symptoms (%)	2 (9.5%)	15 (48.4%)	0.003†
MNSI-Q score	1 ± 0.8	2.1 ± 2	0.017*
MNSI-E score	1 ± 0.5	2.9 ± 1.3	<0.001*
Abnormal MNSI score (%)	0 (0%)	20 (64.5%)	
PNV score			
PNV 1 left	4.1 ± 5	9.7 ± 7.2	<0.001*
PNV 1 right	3.4 ± 3.3	10.2 ± 7.4	0.004*
PNV 4 left	12.6 ± 6.3	20.4 ± 4.8	<0.001*
PNV 4 right	10.7 ± 5.3	20 ± 4.9	<0.001*
PNV 8 left	16 ± 7.3 (n = 19)	25.1 ± 3.9 (n = 30)	<0.001*
PNV 8 right	14.6 ± 7.8 (n = 19)	23.2 ± 4.9 (n = 30)	<0.001*

Data are presented as mean ± standard deviation or as N (%). P-values were calculated using the *Mann-Whitney U and †χ^2 tests. N = number; DPN = diabetic peripheral neuropathy; MNSI-Q = Michigan neuropathy screening instrument questionnaire; MNSI-E = Michigan neuropathy screening instrument examination; PNV = peripheral neuropathy vibration.

Table 2. Results of neuropathy examinations [2].

4.3. Detection of a decrease in asymptomatic tactile sensation in diabetic patients

Next, a comparison was made of the tactile sensitivity of 31 asymptomatic DPN patients and 32 healthy volunteers. The results confirmed that the asymptomatic DPN patients exhibited a significant reduction in sensitivity [3].

This part of the study focused on the asymptomatic development of decreased sensation, associated with diabetes mellitus. The goals were to investigate the use of the quantitative tactile sensation measurement device to examine diabetic patients who were unaware of abnormal or decreased sensation and to determine whether tactile sensation is reduced in asymptomatic patients. A group of healthy controls was recruited, and the finger method was used to measure the TST score of the index and middle fingers in the three procedures TST-1, TST-4, and TST-8. The TST scores ranged from 1 to 30, and a comparison was made between the two groups. The TST scores of the diabetic patients were significantly higher ($P < 0.05$). The TST scores for the left fingers of the diabetic patients and healthy controls were 5.9 ± 6.2 and 2.7 ± 2.9 in TST-1, 15.3 ± 7.0 and 8.7 ± 6.4 in TST-4, and 19.3 ± 7.8 and 12.7 ± 9.1 in TST-8, respectively (**Table 3**).

Overall, the tactile threshold of the fingers of asymptomatic DPN patients was shown to be higher than that of the healthy controls.

The results suggested that the quantitative tactile sensation measurement device was able to detect a decrease in tactile sensation in diabetic patients who were themselves unaware of abnormal or decreased sensitivity.

Test conditions	Healthy controls (N = 32)	Asymptomatic diabetic patients (N = 31)	P-value
TST-1 for left fingers	2.7 ± 2.9	5.9 ± 6.2	0.025
TST-1 for right fingers	2.9 ± 3.5	4.7 ± 5.2	0.160
TST-4 for left fingers	8.7 ± 6.4	15.3 ± 7.0	<0.001
TST-4 for right fingers	8.4 ± 6.7	13.9 ± 7.2	0.002
TST-8 for left fingers	12.7 ± 9.1	19.3 ± 7.8	0.005
TST-8 for right fingers	12.1 ± 8.9	17.3 ± 7.9	0.009

Data are presented as mean ± standard deviation or as N (%). P-values were calculated using *Mann-Whitney U test. N = number; TST = tactile sensation threshold; TST-1 = TST 1 direction test; TST-4 = TST 4 direction test; TST-8 = TST 8 direction test.

Table 3. Scores on the tactile sensation threshold test [3].

4.4. Summary of the three previous studies

In this section, we summarize the results of the three tests performed on the quantitative tactile examination device. The instrument was demonstrated to be capable of quantitative evaluation of the reduction in tactile sensitivity (or increase in tactile threshold) of patients with DPN. The instrument was also able to distinguish between patients with DPN and non-DPN. Finally, the tactile sensitivity of asymptomatic DPN patients was shown to be lower than that of healthy subjects.

This suggests that the device can be used to distinguish the different stages of DPN.

Although the tests involved a relatively small number of subjects, they suggested that a decrease in tactile sensitivity was present in patients with both severe and mild DPN (**Figure 9**).

4.5. Statistical revalidation using propensity score

To examine whether significance could be added to the TST score by adjusting to reflect the patient's background, a propensity score was derived.

In a cross-sectional study, the novel micro-vibration actuator with shape memory alloy wires was used to measure the tactile sensations of 68 type-2 diabetic outpatients and 89 healthy controls. Patients were again evaluated using the ADA criteria [16], the Michigan Neuropathy Screening Instrument (MNSI) [20], and the TST scores for the index and middle fingers. Patients were classified as probable DPN (n = 31) or non-DPN (n = 37) using the ADA criteria and as symptomatic (n = 26) or asymptomatic (n = 42) using the MNSI. Propensity score weighting was applied to compare the scores of each patient group with that of the control group.

The mean time for determining the TST score was approximately 3 min/patient for all groups. The TST score of every patient group was significantly higher than that of the control group ($P < 0.01$). The right finger scores of the DPN, non-DPN, symptomatic, asymptomatic, and

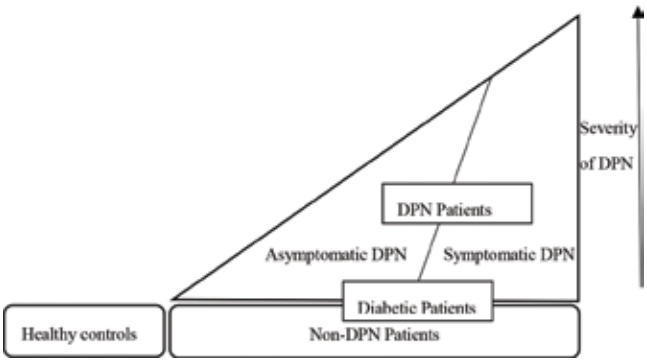

Figure 9. Severity and classification of DPN. DPN = diabetic neuropathy.

control groups were 20.1 ± 4.9, 11.7 ± 5.1, 19.4 ± 4.5, 15.7 ± 6.9, and 6.5 ± 5.7, respectively. This gave P values of 0.00 for DPN, 0.198 for non-DPN, 0.002 for symptomatic, and 0.025 for asymptomatic.

The results confirmed that our novel device provides simple quantitative evaluation of tactile sensation in diabetic patients, facilitating the early detection of asymptomatic DPN.

5. Comparison with other DPN evaluation techniques

In this section, we first describe the diagnostic criteria for DPN and give an outline of representative evaluation methods. Next, we roughly classify these nerve conduction studies as qualitative or quantitative and compare them. Finally, we discuss the difference between these quantitative tests and our proposed method.

5.1. Diagnostic criteria and representative examination methods for diabetic neuropathy

No specific tests for DPN currently exist and nor are diagnostic criteria reflecting an internationally established consensus available. It is therefore necessary to base comprehensive diagnoses of neuropathy on neurological symptoms and the results of examinations. The diagnostic criteria (**Table 4**) [16] of the A DA are used in daily clinical practice.

The tests used include the pain sensation test, vibration sensation test, 10-g monofilament test, and Achilles tendon reflex assessment. By regular application of these tests, it is possible to evaluate the onset and development of neuropathy. They are also effective in the early diagnosis of asymptomatic DPN. Being relatively easy to implement, the tests are useful when applied by a proficient practitioner. However, the results are qualitative.

To confirm the diagnosis, quantitative nerve conduction tests are necessary. These are not widely available, however, as they are time-consuming and require the use of expensive equipment.

Diagnosis	Diagnosis items	Purpose
Possible DSPN	The symptoms or signs of DSPN may include the following. Symptoms: decreased sensation, positive neuropathic sensory symptoms (e.g., "asleep numbness," prickling or stabbing, burning, or aching pain) mainly in the toes, feet, or legs. Signs: symmetric decrease in distal sensation or unequivocally decreased or absent ankle reflexes	Clinical use
Probable DSPN	The combination of any or two or more of the following symptoms and signs: neuropathic symptoms, decreased distal sensation, or unequivocally decreased, or absent ankle reflexes	Clinical use
Confirmed DSPN	The presence of a nerve conduction abnormality and one or more symptoms or one or more signs of neuropathy	Clinical use Clinical research

DSPN: distal symmetric polyneuropathy (used synonymously with DPN in this chapter).

Table 4. Definitions of minimal criteria for DSPN [16].

5.2. Comparison of qualitative methods and the quantitative method

The pain sensation test, made with a sharp object such as a pin, is used to test for hyperalgesia and weakness.

In the vibration sensation test, sensitivity to vibration is investigated by applying a 128 Hz tuning fork to the ankle or the toe of the foot. The ability to sense vibration is compared with that of a healthy person.

In patients with DPN, the Achilles tendon reflex is often attenuated or absent, providing an excellent test that can be performed in a short time if the examiner is proficient.

In the 10-g monofilament test, a thin thread of monofilament nylon is placed on the foot. It is used to investigate the function of the nerve that senses tactile and pressure. In DPN patients, the sensations are dulled.

These tests are representative qualitative examination techniques that can be performed in a short time.

In NCS, the stimulation conductivity of the peripheral nerve is measured. In patients who have developed neuropathy, the speed with which the stimulus is transmitted becomes slower. NCS is able to produce a quantitative measurement of the speed of the peripheral nerves of the human body [21, 22]. However, it requires the patient to be subjected to painful electric shocks. NCS also requires the use of expensive equipment. The examination time is lengthy, and if multiple peripheral nerves on both the left and right side are examined, the procedure may take several hours. NCS is therefore only available at large specialized hospitals.

5.3. Comparison of NCS and quantitative tactile examination methods

The proposed finger method is superior to NCS in some respects. First, the inspection time is short, taking a maximum of approximately 3 min. Second, the patient experiences no

pain, as no electric current is applied to the nerve of the patient. The sensation is experienced only in the nerve being investigated. Third, while medical examination is normally performed by an expert, it is possible for the subject himself/herself to perform the test. This allows the test to be run at a place and time chosen by the patient. If tactile sensation reduces over time, poor glycemic control may be indicated. The test can detect such haptic loss. By making patients aware that their sense of touch is declining, the test may encourage them to seek treatment.

6. Discussion

6.1. Strengths and significance of this device

A key strength of this device is that it can be used by patients themselves, producing quantitative results within minutes. It may be applied not only to DPN but to all forms of peripheral neuropathy. We are currently developing a device for assessing the lower limbs. Applications to diseases other than DPN are also being investigated.

6.2. Limitations

The cross-sectional studies reported here involved outpatients, and the sample sizes were limited. To confirm the effectiveness of the technology, future studies should use larger samples and a wider range of patients.

7. Future work

The tactile test quantification technology introduced in this chapter has a wide range of potential applications. In future studies, we will apply it to other types of peripheral neuropathy.

One such current study is applying the tactile test equipment to the feet. The equipment has already developed to a point where practical application is possible. We plan to conduct further clinical studies of patients with DPN, quantitatively measuring the tactile sensations in the feet as well as the fingers. This will be useful in identifying DPN in different areas of the body.

In further developments, we will use the technology to visualize the severity of peripheral neuropathy in a manner that will be easily understandable by both healthcare professionals and patients. This may prove useful for monitoring the severity of peripheral neuropathy induced by anticancer drugs such as paclitaxel. It may also encourage patients with peripheral neuropathy to seek early treatment.

No currently available examination method can distinguish clearly between nociceptive pain and neuropathic pain, which are treated with standard pain medications and expensive analgesics, respectively. Patients who are misdiagnosed may be prescribed inappropriate analgesics and experience pain over a long period. The prescription of inappropriate pain

medication may also add unnecessarily to medical expenses. Our tactile test technique may provide a useful tool for distinguishing between nociceptive and neuropathic pain.

By promoting early detection and treatment of asymptomatic peripheral neuropathy, this novel technology may reduce the medical and social resources needed when complications arise or the severity of the condition is unknown. By promoting the use of this technology, the authors hope to make a social contribution.

8. Conclusions

A quantitative tactile examination technique using shape memory alloy actuators was developed. The painless, simple, and quantitative tactile examination technology that can be performed in a short time is an ideal examination technology. A notable feature of this technology is that it succeeded in miniaturization and power saving. This was demonstrated to allow early detection of DPN. Large-scale clinical trials should be conducted, to confirm the effectiveness of this novel technology, which may have applications in the identification of a wider range of neuropathies.

Acknowledgements

This work was partly supported by the Grants-in-Aid for Scientific Research, the Japan Society for the Promotion of Science (no. 24500548 and 17 K17925), and by endowments from MSD and Takeda Pharmaceutical Company.

Conflict of interest

Keiji Uchida holds a patent on the quantitative tactile examination device. The other authors declare that they have no competing interests.

Author details

Junichi Danjo[1]*, Sonoko Danjo[1], Hideyuki Sawada[2], Keiji Uchida[3] and Yu Nakamura[1]

*Address all correspondence to: jdanjo@med.kagawa-u.ac.jp

1 Department of Neuropsychiatry, Kagawa University, Japan

2 Department of Applied Physics, Waseda University, Japan

3 SCA Corporation, Japan

References

[1] Sawada H, Nakamura Y, Takeda Y, Uchida K. Micro-vibration array using SMA actuators for the screening of diabetes. In: International Conference on Human System Interaction; Poland. 2013

[2] Danjo J, Sawada H, Uchida K, Danjo S, Nakamura Y. Efficacy of a new micro-vibration sensation measurement device at detecting diabetic peripheral neuropathy using a newly devised finger method. Journal of General and Family Medicine. 2017;**18**(4):155-161

[3] Danjo J, Danjo S, Nakamura Y, Uchida K, Sawada H. Micro-vibration patterns generated from shape memory alloy actuators and the detection of an asymptomatic tactile sensation decrease in diabetic patients. IEICE Transactions on Information and Systems. 2016;**E99-D**(11):2759-2766

[4] Zhao F, Jiang C, Sawada H. A novel braille display using the vibration of SMA wires and the evaluation of braille presentations. Journal of Biomechanical Science and Engineering. 2012;**7**(4):416-432

[5] Sawada H, Uchida K, Danjo J, Nakamura Y. A Screening device of diabetic peripheral neuropathy based on the perception of micro-vibration patterns. In: 2015 RISP International Workshop on Nonlinear Circuits, Communications and Signal Processing. 2015. pp. 162-165

[6] Sawada H, Uchida K, Danjo J, Nakamura Y. Development of a non-invasive screening device of diabetic peripheral neuropathy based on the perception of micro-vibration. In: International Conference on Computational Intelligence in Bioinformatics and Computational Biology; Thailand. 2016

[7] Danjo J, Danjo S, Sawada H, Uchida K, Nakamura Y. Diabetic neuropathy: A focus on the testing method. International Journal of Family & Community Medicine. 2018;**2**(1):00027

[8] Takeda Y, Sawada H. Tactile actuators using SMA micro-wires and the generation of texture sensation from images. In: International Conference on Intelligent Robots and Systems; Japan. 2013

[9] Sawada H, Takeda Y. Tactile pen for presenting texture sensation from touch screen. In: International Conference on Human System Interactions; Poland. 2015

[10] Sawada H, Kitano S, Yokota, S. A hapto-tactile display for presenting virtual objects in human-scale tactual search. In: International Conference on Human System Interactions; UK. 2016

[11] Sawada H. Tactile display using the micro-vibration of shape-memory alloy wires and its application to tactile interaction systems. Pervasive Haptics. 2016;**21**:55-77

[12] Nagano K, Ashihara N. Communication aid for deaf-blind due to the vibration motor. In: IEICE Technical Report, HCS96-09. 1996

[13] Kanno T, Nagano H, Asihara O, Nagahashi H. A communication aid for deaf-blind people using vibration motors. The Transactions of the Institute of Electronics, Information and Communication Engineers. 1997;**J80-A**(9):1509-1516

[14] Uchida M, Tanaka H, Ide H, Yokoyama S. Vibration tactile display using 16 different modulation wave of a single PZT transducer. IEEJ C. 2000;**120-C**(6):825-830

[15] Harrison C, Hudson SE. Providing dynamically changeable physical buttons on a visual display. In: Proc. of 27th Annual CHI Conf. on Human Factors in Computing Systems. 2009. pp. 299-308

[16] American Diabetes Association. Diagnosis and classification of diabetes mellitus. Diabetes Care. 2014;**37**(1):81-90. DOI: 10.2337/dc14-S081

[17] Pop-Busui R, Boulton AJ, Feldman EL, Bril V, Freeman R, Malik RA, Sosenko JM, Ziegler D. Diabetic neuropathy: A position statement by the American Diabetes Association. Diabetes Care. 2017;**40**(1):136-154

[18] Vallbo AB, Johansson RS. Properties of cutaneous mechanoreceptors in the human hand related to touch sensation. Human Neurobiology. 1984;**3**(1):3-14

[19] Tesfaye S, Boulton AJ, Dyck PJ, et al. Diabetic neuropathies: Update on definitions, diagnostic criteria, estimation of severity, and treatments. Diabetes Care. 2010;**33**:2285-2293

[20] Feldman EL, Stevens MJ, Thomas PK, Brown MB, Canal N, Greene DA. A practical two-step quantitative clinical and electrophysiological assessment for the diagnosis and staging of diabetic neuropathy. Diabetes Care. 1994;**17**:1281-1289

[21] Dyck PJ, Litchy WJ, Lehman KA, Hokanson JL, Low PA, O'Brien PC. Variables influencing neuropathic endpoints: The Rochester diabetic neuropathy study of healthy subjects. Neurology. 1995;**45**(6):1115-1121

[22] Dyck PJ. Detection, characterization, and staging of polyneuropathy: Assessed in diabetics. Muscle & Nerve. 1988;**11**(1):21-32

Section 4

Fault Detection

Chapter 7

Root Cause Analysis of Actuator Fault

Mei Zhang, Ze-tao Li, Boutaib Dahhou and Michel Cabassud

Additional information is available at the end of the chapter

http://dx.doi.org/10.5772/intechopen.76211

Abstract

This chapter develops a two-level fault diagnosis (FD) and root cause analysis (RCA) scheme for a class of interconnected invertible dynamic systems and aims at detecting and identifying actuator fault and the causes. By considering actuator as an individual dynamic subsystem connected with process dynamic subsystem in cascade, an interconnected system is then constituted. Invertibility of the interconnected system in faulty model is studied. An interconnected observer is introduced and aims at monitoring the performance of the interconnected system and providing information of actuator fault occurrence. A local fault filter algorithm is then triggered to identify the root causes of the detected actuator faults. According to real plant, outputs of the actuator subsystem are assumed inaccessible and are reconstructed by measurements of the global system, thus providing a means for monitoring and diagnosing the plant at both local and global level.

Keywords: actuator fault, invertibility, interconnected system, input estimation

1. Introduction

Actuators are fundamental components in process industry. However, as they are installed in outdoor environment, continuous exposure to harsh environmental conditions (sun beam, rainfall, etc.) may reduce the optimal performance of system. Among all classes of possible faults, actuator fault has been considered to be one of the most critical challenges to be solved, since an actuator fault may cause significant disturbances on the final product. In addition, with the development of technological advances, actuators are increasingly integrated, intelligent and complex; therefore, each actuator itself is a dynamic system and exhibits complicated dynamics of system. For example, a valve actuator is an assembly of positioner, pneumatic servo-motor and control valve, as given in [1]; mathematical models presented in, like [2, 3],

have shown that control valve can be seen as a nonlinear dynamic system. Therefore, modern control system can be viewed as composed of dynamic subsystems connected in series. In all situations, the global plant and/or each subsystem can be analyzed at different levels down to the component level in estimating the reliability of the whole plant. A typical control system, for example, has at least three cascade subsystems: sensor, process and actuator subsystems.

As a result of the increasingly complexities, the probability of occurrence of an actuator fault is also increased. In real industrial system, the actuator faults may related to, for example, pressure drop out in hydraulic components, short circuiting or overheating of electrical components, breakage in bearings due to mechanical stresses, leakages in pipes, sticking of valves, cracks in tanks, and so on. Actuator fault may cause a malfunction of the installation; resulting in a serious impact in equipment, such as production quality, security, economy, levels of contamination, in the worst of cases a fault may even cause severe accidents. According to Zhang [4], about 42% of the potential waste in annual energy consumption is estimated due to leaks of compressed air in a pneumatic system, leaks can degrade machine performance since actuators produce less force, run slower, and less responsive. Faults may even lead to catastrophic incidents. A lesson is from the well-known TMI-II accident in 1979, and it has been proved that this accident was initiated by the valve position failure of feed water pump of the main reactor [5].

Consequently, in order to maintain high-efficiency of the operation and ensure stability of the product quality, real-time actuator fault detection, identification and accurate fault location are quite desired.

2. Status and challenges of current actuator FDD methodologies

The last few decades have witnessed significant improvements in actuator FDD techniques, as illustrated in **Figure 1**. One main approach is system level-based diagnosis approach aims at detecting and identifying actuator fault existence and location from view point of global system. Another common kind of methodologies focuses on the field device level and aims at analyzing internal dynamics of a specific actuator.

2.1. System level-based diagnosis

Traditionally, for most engineers, system level-based methods act as basic tools to design and carry out some monitoring activities where intelligence is at the system level of the process plant, rather than at the field device level. In these methods, dynamics of filed devices (actuator) is ignored, instead, they are treated as a component which is viewed as constants in the input or output coefficient matrix (function) of the process system model. The malfunctions can be treated separately, and they enter the process model as actuator where faults are considered as changes of the input or output coefficient matrix elements. An actuator fault is normally considered as additive effects, as internal dynamics of the field device may be lost.

Many different approaches to system level model-based fault detection and diagnosis have been introduced. Works in [6] reviewed process fault detection and diagnosis based on the principle of analytical redundancy. A key approach is based on residuals generation.

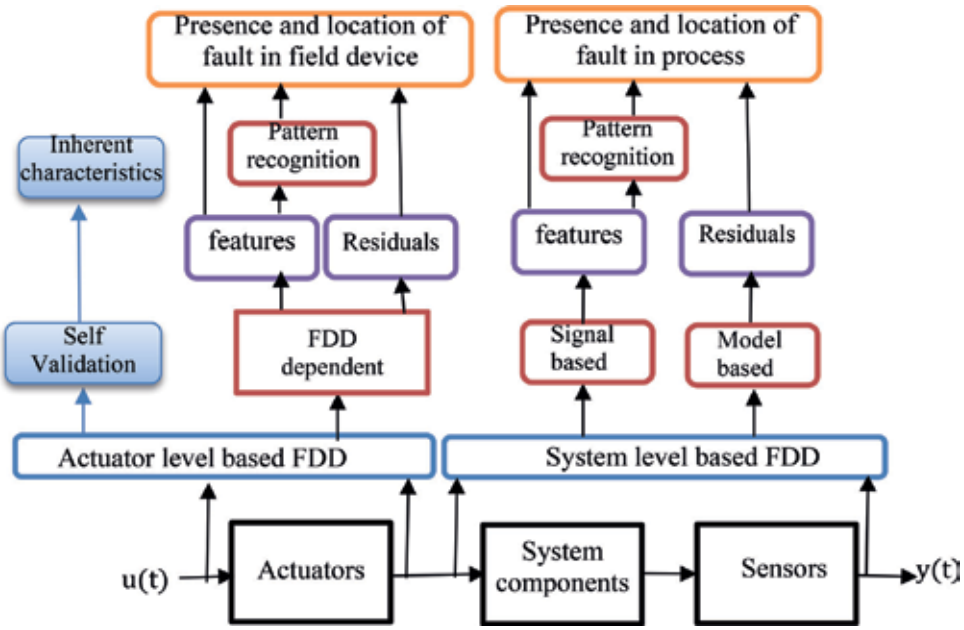

Figure 1. Typical usages of different categories of actuator FDD methods.

In [7], a nonlinear FDI filter is designed to solve a fundamental problem of residual generation using a geometric approach. The objective is to build a dynamic system for the generation of residuals that are affected by a particular actuator fault and not affected by disturbances and the rest of faults. The problem of actuator fault isolation is also studied by exploiting the system structure to generate dedicated residuals (see, e.g. [8]). In addition, adaptive estimation techniques are used to explicitly account for unstructured modeling uncertainties for a class of Lipschitz nonlinear systems (see, e.g. [9]). Another approach different to residual generation is fault estimation or fault reconstruction which can determine the size, location and dynamics behavior of the actuator fault, like in [10, 11]. There are several methods typically used for fault reconstruction: sliding mode observers [12, 13], unknown input observers [14, 15], input reconstruction [16, 17]. For instance, a sliding mode observer is designed to reconstruct or estimate faults by decoupling the input in [18]. Veluvolu et al. [19] develop a high gain observer with multiple sliding modes for simultaneous state and fault estimations for MIMO nonlinear systems.

As a result of incomplete identification of internal variables of the actuator, the applications of system level-based FDD methodologies are mainly limited to the existence and isolation of a fault from view point of the global level, while root causes of this fault cannot be obtained. For example, Di Miceli Raimondi et al. [20] have shown that decrease of output temperature may due to decrease of fluid flowrate, and the causes of this decrease of fluid flowrate may be caused by valve clogging, stop of utility fluid pump or leakage. Nevertheless, with respect to the abovementioned system level-based FDD methodologies, fault symptoms can be detected and isolated without having the capability to pinpoint the real root cause of the fault.

However, root causes of a fault in a component can cause significant process disturbances and influence the quality of the final product. On the one hand, in each component system, there can be fault types specific for that system; therefore it is not capable of analyzing all the actuator faults at the process level. However, recognizing the root cause of a fault correctly is essential in order to be able to allocate resources effectively to repair the problem and perform maintenance actions. Another major problem related to system level-based FDD approaches is the delay of detection. Since lack of internal dynamics of a component, an abnormal deviation of an internal variable inside the field device may not be observable until some internal variable saturates and field device performance are affected [21]. After field device performance is affected by the internal faults, these faults can then be detected through process variables. But the detection may occur too late to keep process performance at an optimal level and to have time to prepare repair work.

2.2. Actuator level-based diagnosis

For the purpose of bettering understanding potential relationship from cause to effect of an actuator fault, component-level diagnosis can be a solution whereby capability of locating subcomponent faults for root cause analysis is available. The development of actuator FDD can be categorized as intelligent self-validation approaches and FDD-dependent methods.

Intelligent self-validation approaches make use of Instrumentation and Control (I&C) technologies, as so called intelligent devices, or smart sensing [22]. It is an instrument that is designed to compensate for its own undesirable inherent characteristics to correct from fault conditions, for example, smart positioner in [1], self-validating actuator in [23, 24]. However, existed intelligent instrument is restricted to self-diagnosis from a low level, and they lack capability of supervising performance of the overall plant.

The most active research area in actuator diagnostics are FDD involved methods, categorized as: signal-based methods and model-based methods. The signal-based methods consider input and output of the device measurement signals and their key characteristics. For example, Sarosi et al. [25] propose an algorithm to detect valve stiction for diagnosis oscillation of control valve by signal processing. Wavelet analysis is a major aspect of signal processing method for fault detection. As in [26], it developed automatic feature extraction of waveform signals for process diagnostic performance improvement. In [27], wavelet transform is applied to detect abrupt changes in the vibration signals obtained from operating bearings being monitored, whereas the model-based methods use first-principle models or system identification techniques to diagnose fault resource. They rely mainly on model-based identification procedures to estimate related parameters. Like in [28, 29], a set of nonlinear differential equations representing the system dynamics based on physics are derived. In [30], derivations of similar nonlinear models have been presented in many recent publications, in which a detailed mathematical model of dual action pneumatic actuators controlled with proportional spool valves and two nonlinear force controllers based on the sliding mode control theory were developed. Puig et al. [2] develop an interval observers-based passive fault detection method and apply to a control valve in the DAMADICS benchmark problem. The authors in [31] introduce a state space sliding-stem control valve

model in order to utilize an advanced nonlinear model predictive control strategy to compensate for the effects of friction. Other nonlinear modeling approaches involve using neural networks or fuzzy logic, such as in [32, 33].

A major difficulty of actuator level-based diagnosis methodology is lack of dynamics information of global system. Another challenge is getting data from the subsystem since direct access to actuators is often not possible or difficult via physical measurements due to distances or rough environment. Sensors have to be installed to all the primary variables of the field devices to make faults of these field devices observable. However, installing additional sensors into the field devices leads to very complicated and expensive systems. Moreover, even if the output of the field device (e.g., actuator) is available for measurement, considering the noisy output of the sensor of the field device, the numerical differentiation would be too noisy. The noisy control input made from these signals, not only could damage the field device, but also would make less accuracy in tracking and then instability in the control scheme. Furthermore, some parameters are not available for directly measurement, for instance, as a common actuating signal, concentration in chemical process cannot be measured through physical sensors.

Therefore, although many different fault diagnosis methods have been developed from various industries, neither of the aforementioned system level based or actuator level-based FDD methods are however sufficient alone to achieve effective diagnosis to handle all the requirements for an engineering problem. In summary, there is a need for a FDD algorithm which is capable of root cause diagnosing at local actuator level as well as system supervising at global plant level.

3. Problem formulations

Motivated by the above considerations, this chapter is concerned with the challenges of applying system inverse and model-based FDD techniques theory to handle the joint problem of actuator fault diagnosis both locally and globally. We try to develop a hybrid approach that combines different methods, thus, the weaknesses of individual methods can be compensated and more accurate diagnosis results are obtained. For that, the overall system is decomposed into several subsystems and develops the FDD algorithm from the view point of both local and global system, as shown in **Figure 2**.

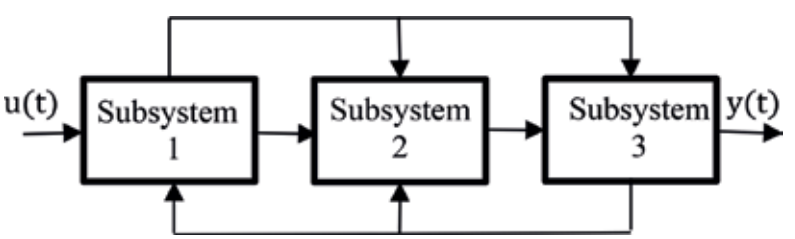

Figure 2. System decomposition and interconnections.

As shown in **Figure 2**, according to real engineering plant, the information that can be obtained from the developed system will include only the performance of critical parameter, such as temperature of continuous chemical reactor, and manipulated variables of the component such as the input of the reactor main control valve. The attempt is to explain how the behavior of overall output can be interpreted to identify subcomponent faults in component subsystem, so as to carry out advanced FDD algorithm for recognizing root causes of detected faults. Like this, this will enable individual actuator to monitor internal dynamics locally to improve plant efficiency and diagnose potential fault resources to locate malfunction when operation performance of global system degrades or has measurement faults. This reduces the complexity of the centralized or distributed monitoring system because the dimensionality problem, the number of sensors, wires, and diagnosis loops connected to the monitoring system is reduced. On the other hand, the obtained information is assumed to be only global output, this can be more realistic and technical availability because field devices are normally remote from the control room and additional sensors may cause reliability and economy problem.

In order to achieve the objectives, there are several tasks the new nonlinear FDD schemes need to study. The first intention is to develop a reasonable system structure for the FDD algorithm, by which local faults can be distinguished globally. The second intention is to establish a complete observer-based FDD framework for local nonlinear subsystems.

4. Invertible interconnected system structure

As mentioned above, a modern control system can be analyzed at different levels down to the component level in estimating the reliability of the whole plant. Therefore, the first consideration is to answer the question of how to decompose the given control problem into manageable subproblems, thus forming a dynamic system structure. We develop an interconnected dynamic system by considering that actuator is viewed as subsystem connected with the process subsystem in series. Through the overall system, the only available measurement is the output of the terminal process subsystem. We then consider the problem that arises when the output from the low-level nonlinear subsystem is not available directly, but instead available via a second nonlinear subsystem. That is, the output from the low-level nonlinear subsystem acts as the input to a high-level subsystem, from which output measurement is in turn available. This situation results in a cascade interconnection that is illustrated in **Figure 3**.

As shown in **Figure 3**, it is considering an interconnected system $\sum$which consists of two subsystems: actuator $\sum_a$ and process $\sum_p$ subsystems. The vector u represents the input vector of the actuators subsystem, which is also the input of the series system, v is the fault vector related to parameter variations of actuator subcomponent or external disturbance, u_a is the actuators output vector, also the input of process subsystem and y is the output vector of the process subsystem, also the output of the overall series system. The basic idea is to identify the fault v at the local level, while monitoring dynamics of the overall plant at the global level.

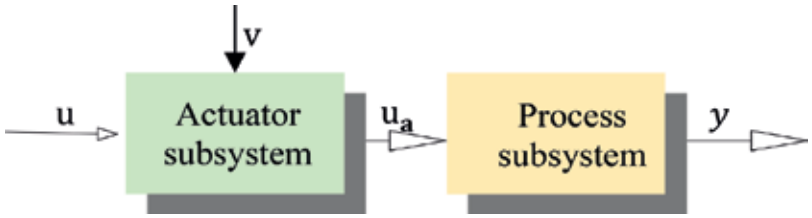

Figure 3. An interconnected system structure.

A key feature, opportunity and technical challenge of the scheme is to obtain the conditions by which the information (useful input u or faults v) issued by actuator subsystem can completely be transmitted to the final terminal and have distinguishable effects on the output of the process system y. In this way, we can realize actuator faults in local subcomponent while utilizing the measurable output y of the process system. With respect to this consideration, if view v as unknown input in the system, this can be seen as problem of input observability. Input or fault observability is equivalent with left invertibility of system. In [35], input can be uniquely recovered from output and the initial state if dynamical system is left invertible.

We then consider a left invertible interconnected nonlinear system structure by which actuator is viewed as a subsystem connected with the process subsystem in cascade manners, thus identifying component faults with advancing FDD algorithm in the subsystem. The left invertibility of the interconnected system is required for ensuring faults occurred in actuator subsystem can be distinguished globally. In this case, the performance of the overall interconnected system and fault occurrence are recognized by a system level-based diagnosis algorithm while several independent local diagnosis subsystems are responsible for potential fault candidates of internal component.

4.1. Process subsystem modeling

Assuming the MIMO process subsystem is input affine nonlinear system which is a common consideration involving system inverse, and is described by Eq. (1):

$$\sum\nolimits_p : \begin{cases} \dot{x} = f(x) + \sum_{i=1}^{m} g_i(x) u_a \\ y = h(x, u_a) \end{cases} \tag{1}$$

where the state of the process subsystem vector $x \in M$, an n-dimensional real connected smooth manifold, e.g. $\Re^n$, f, g_i are smooth vector field on M, $u_a \in \Re^m$ is the input of process subsystem, which is also the output of the actuator and which we assume to be inaccessible and want to estimate on the basis of measures taken on the evolution of the system, $y \in \Re^p$ is overall system output. If initial conditions are specified, the relevant equation $x(t_0) = x_0$ is added to the system.

4.2. Actuator subsystem modeling

Normally, an actuator subsystem can be described by Eq. (2):

$$\sum\nolimits_a : \begin{cases} \dot{x}_a = f_a(x_a, u, \theta_{fa}) \\ u_a = h_a(x_a, u, \theta_{fs}) \end{cases} \tag{2}$$

where $x_a \in \mathcal{R}^n$ is the state, $u \in \mathcal{R}^l$ is the input, $u_a \in R^p$ is the output of the actuator subsystem, which is also the input of the process subsystem, $\theta_{fa} \in \mathcal{R}^q$ represents the actual parameters (i.e., when no faults are present in the system), $\theta_{fa} = \theta_{fa0}$ where θ_{fa0} is the nominal parameter vector (understanding "fault" as an unpermitted parameter deviation in the system), $\theta_{fs} \in \mathcal{R}^q$, represents the parameters in the output equation (if a sensor fault occurs $\theta_{fs} \neq \theta_{fs0}$, where θ_{fs0} represent the nominal parameters in the output equation). If initial conditions are specified, the relevant equation $x_a(t_0) = x_{a0}$ is added to the system.

Thus, an interconnected system $\sum$ is then constructed by these two subsystems $\sum_a$ and $\sum_p$ subsystems whereby the input is vector of u while output vector is y.

Assumption 1: The input vector of both subsystem u_a and u are locally essentially bounded function: $u_a(.) \in [t, \infty) \to \mathfrak{R}^m$, $u(.) \in [t, \infty) \to \mathfrak{R}^l$; if two inputs differ on a set of measure zero, i.e. almost everywhere (a.e), then they are considered to be equal.

If fault v is as integration of either parameters fault θ_{fa}, θ_{fs} or other disturbance signals, a fault mode of Eq. (2) is then obtained:

$$\Gamma_a := \begin{cases} \dot{\hat{x}}_a = f(x_a, u) + \sum_i^m g_{ai}(x_a, u) v_i \\ u_a = h_a(x_a, u) + \sum_i^m l_{ai}(x_a, u) v_i \end{cases} \tag{3}$$

where g, l are analytic functions of the system subject to multiple, possible simultaneously faults. The v (t) is the fault signal $(v_1, \ \ldots, \ v_m)$ whose element $v_i : [0, +\infty) \to \mathcal{R}$ are arbitrary functions of time.

Remark 1: The fault $\sum_i^m g_{ai}(x_a, u) v_i$ represents the parameters fault in θ_{fa} or external disturbance while $\sum_i^m l_{ai}(x_a, u) v_i$ represents the parameters faults in θ_{fs} or external disturbance. Effect of faults on outputs is independent.

The detectability of one fault in nonlinear system Eq. (3) can be defined as:

Definition 1: The fault v_i, $i = 1, \ldots, m$, is said to be non-detectable if for $v_i \neq 0$ the relation

$$u_a(x_{a0}, \ x_a, u, 0) = u_a(x_{a0}, \ x_a, u, 0, \ldots, v_i, \ldots, 0) \tag{4}$$

is satisfied; if not, the fault v_i is detectable.

Definition 2: The fault $v_i, i = 1, \ldots, m,$ is said to be detectable and has independent effect on the system output y if the series system is invertible.

Definition 3: Fix an output set $\mathcal{Y}$ and consider an arbitrary interval $[t_0, T)$, the interconnected system described by Eqs. (1) and (2) is invertible at a point $(x_{a0,}\ x_0) := x(t_0) \in \mathcal{X}$ over $\mathcal{Y}$, $x_a(t_0) \in \mathcal{X}_a(t_0)$ over $\mathcal{U}_a$, if for every $y_{[t_0,T)} \in \mathcal{Y}$, the equality $\left(H_a \circ H_p\right)_{(x_{a0,}\ x_0)}\left(u_{1[t_0,T)}\right) = \left(H_a \circ H_p\right)_{(x_{a0,}\ x_0)}\left(u_{2[t_0,T)}\right) = y_{[t_0,T)}$ implies that $\exists \varepsilon > 0,$ such that $u_{1[t_0,t_0+\varepsilon)} = u_{2[t_0,t_0+\varepsilon)}$. The system is strongly invertible at a point $(x_{a0,}\ x_0)$ if it is invertible for each $x_a \in \mathcal{N}_a(x_{a0}),\ x \in \mathcal{N}(x_0)$, where $(\mathcal{N}_a, \mathcal{N})$ is some open neighborhood of $(x_{a0,}\ x_0)$. The system is strongly invertible if there exists an open and dense sub-manifold $\mathcal{M}_a$of $\mathcal{X}_a$, $\mathcal{M}$of $\mathcal{X}$, such that $\forall (x_{a0}, x_0) \in (\mathcal{M}_a, \mathcal{M})$, the system is strongly invertible at $(x_{a0,}\ x_0)$.

Theorem 1: Consider the interconnected system $\sum$ which consists of two subsystems: actuator $\sum_a$ and process$\sum_p$ subsystems depicted by Eqs. (1) and (2), and an output set $\mathcal{Y}$. The interconnected system is invertible at (x_0, x_{a0}) over $\mathcal{Y}$, if and only if each subsystem actuator $\sum_a$ and process$\sum_p$ is invertible at x_{a0} over $\mathcal{U}_a$, and x_0 over $\mathcal{Y}$, respectively.

Proof: Considered H_a as the input output mapping of actuator $\sum_a$subsystem, while H_p is the input output mapping of process$\sum_p$ subsystem. Then, the input output mapping of the interconnected system is the composition $H_a \circ H_p$.

a. (Sufficiency): invertibility of a dynamic system refers to bijective of the input output mapping. Since both subsystems are invertible, the corresponding mapping H_a and mapping H_p are bijective mapping. Moreover, composition of two bijective mappings is a bijective mapping, so input output mapping $H_a \circ H_p$of the cascade system is bijective. Thus, the cascade interconnected system is invertible.

b. (Necessity): We now show that if any of the subsystems is not invertible at (x_0, x_{a0}), then the interconnected system $\sum$ is not invertible.

On the one hand, supposed that the process subsystem $\sum_p$ is not invertible, while the actuator subsystem $\sum_a$ is invertible. Then for the actuator subsystem, fix an output set $\mathcal{U}_a$ and consider an arbitrary interval $[t_0, T)$, there exist two distinct inputs for $\exists \varepsilon > 0\ u_1 \neq u_2$ on $[t_0, t_0 + \varepsilon)$, that may yield two distinct outputs $H_{a(x_{a0})}\left(u_{1[t_0,T)}\right) = u_{a1[t_0,T)}, H_{a(x_{a0})}\left(u_{2[t_0,T)}\right) = u_{a2[t_0,T)},\ u_{a1[t_0,T)} \neq u_{a2[t_0,T)}$. However, for the process subsystem, fix an output set $\mathcal{Y}$, these two distinct inputs $u_{a1} \neq u_{a2}$ on $[t_0, t_0 + \varepsilon)$ may produce two equal outputs $H_{p(x_0)}\left(u_{a1[t_0,T)}\right) = H_{p(x_0)}\left(u_{a2[t_0,T)}\right) = y_{[t_0,T)}$. Therefore, for the series system, these two distinct inputs $u_1 \neq u_2$ on $[t_0, t_0 + \varepsilon)$ may result in two equal outputs:

$$\left(H_a \circ H_p\right)_{(x_{a0,}\ x_0)}\left(u_{1[t_0,T)}\right) = \left(H_a \circ H_p\right)_{(x_{a0,}\ x_0)}\left(u_{2[t_0,T)}\right) = y_{[t_0,T)} \tag{5}$$

Thus, it implies that the interconnected system $\sum$ is not invertible at (x_0, x_{a0}) over $(\mathcal{U}_a, \mathcal{Y})$.

On the other hand, supposed that the process subsystem $\sum_p$ is invertible, while the actuator subsystem $\sum_a$ is not invertible. Then for the actuator subsystem $\sum_a$ in (4.2), fix an output

set $\mathcal{U}_a$ and consider an arbitrary interval $[t_0, T)$, there exist two distinct inputs for $\exists \varepsilon > 0$ $u_1 \neq u_2$ on $[t_0, t_0 + \varepsilon)$, that may yield two equal outputs $H_{a(x_{a0})}\left(u_{1[t_0,T)}\right) = u_{a1[t_0,T)}$, $H_{a(x_{a0})}\left(u_{2[t_0,T)}\right) = u_{a2[t_0,T)}$, $u_{a1[t_0,T)} = u_{a2[t_0,T)}$. Even if, the process subsystem $\sum_a$ in (4.1) is invertible, these two distinct inputs $u_{a1} = u_{a2}$ on $[t_0, t_0 + \varepsilon)$ can only precede one output $H_{p(x_0)}\left(u_{a1[t_0,T)}\right) = H_{p(x_0)}\left(u_{a2[t_0,T)}\right) = y_{[t_0,T)}$. However, for the series interconnected system, these two distinct inputs $u_1 \neq u_2$ on $[t_0, t_0 + \varepsilon)$ result in two equal outputs:

$$\left(H_a \circ H_p\right)_{(x_{a0},\ \ x_0)}\left(u_{1[t_0,T)}\right) = \left(H_a \circ H_p\right)_{(x_{a0},\ \ x_0)}\left(u_{2[t_0,T)}\right) = y_{[t_0,T)} \tag{6}$$

Thus, it implies that the interconnected system $\sum$ is not invertible at (x_0, x_{a0}) over $(\mathcal{U}_a, \mathcal{Y})$. ∎

5. Multilevel fault diagnosis and root cause analysis

The major objective of the chapter focuses on the problem of model-based FDD and root cause analysis (RCA) for multivariable interconnected dynamic system. The attempt is to explain how the behavior of overall output can be interpreted to identify subcomponent faults in actuator subsystem, so as to carry out advanced FDD algorithm for recognizing root causes analysis of faults. As shown in **Figure 4**, the overall objective is to identify the occurrence of the fault v_i in Eq. (3) independently from each other while monitoring the overall plant at both local and global level, as required for reliable operation of complex and high interconnected process system. Fault v_i refers to the parameter variations which are related with special physical meaning, for example, v_i represents fault caused by leakage or valve clogging of an actuator. To realize these causes of an actuator fault is defined as root cause analysis (RCA) in

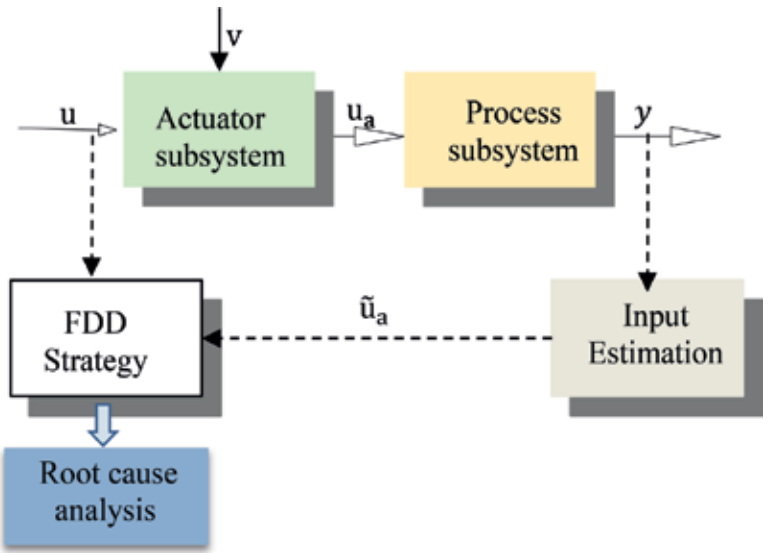

Figure 4. FDD algorithm for component FDD and RCA.

this work. We assume to feed the FDD strategy with input u and output u_a of actuator subsystem at local level, so as to achieve root cause analysis. However, online diagnosis of actuator component is often achieved by a remote supervisory diagnostic system; therefore, to a large extent, it is impractical to measure u_a in realistic industrial condition, so u_a is supposed to be inaccessible in this work. Besides, in order to monitor the plant at a global level, information of global level should be included when FDD function is performed at local subsystem. It became apparent that the FDD algorithm design of an interconnected system with multilevel-based consideration requires that the interconnection be treated as special signals. If u_a can be estimated from the global level measurement y uniquely, then the abovementioned two problems can be solved. In that way, the residual generator of advanced FDD strategy performs some kind of validation of the nominal relationships of the system, using the actual input u, and output $\tilde{u}_a$ reconstructed from measured output y. Hence, a means of monitoring and diagnosis of the overall plant at both local and global level is provided, which result in improved fault localization and provide better predictive maintenance aids.

As mentioned above, invertibility of the interconnected system can be a solution for guaranteeing that the information of actuators subsystem has distinguishable effects on system output. Moreover, an essential requirement of the combination of individual actuator with an advanced diagnostic capability to perform FDD functions is the availability and reliability of the output of the actuator subsystem u_a, which is also the input of the process system. This problem is considered as input reconstruction problem, which can also be viewed as problem of system inversion, as shown in **Figure 4**. Some issues of inversion concepts for input reconstruction were discussed, e.g. [34–36].

In summary, if the overall cascade system is invertible, fault vector v has distinguishable effect on system output vector y. While if process subsystem is invertible, u_a can be uniquely reconstructed by output vector y, in that case, reconstructed $\tilde{u}_a$ and fault vector v also has one-to-one relationship. Then, one can utilize advanced FDD strategy in actuator subsystem while use the output vector y of the interconnected system to identify v, thus achieving FDD at local level while monitoring the whole system at the global level. Above all, the key problem is to provide condition for guaranteeing invertibility of the overall cascade system and individual subsystems.

5.1. Input estimation

According to the input estimation procedure introduced [37], if the process subsystem Eq. (1) is differentially left invertible, the input can be recovered from the output by means of a finite number of ordinary differential equations. Indeed, to derive an expression for $u_a(t)$ as a function of states and output in Eq. (1), following the inversion algorithm given by [37], we have:

$$\begin{bmatrix} y_1^{(r_1)} \\ \vdots \\ y_m^{(r_m)} \end{bmatrix} = \begin{bmatrix} L_f^{r_1} h_1(x) \\ \vdots \\ L_f^{r_m} h_m(x) \end{bmatrix} \begin{bmatrix} L_{g_1} L_f^{r_1-1} h_1(x) & \dots & L_{g_m} L_f^{r_1-1} h_1(x) \\ \dots & \dots & \dots \\ L_{g_1} L_f^{r_m-1} h_m(x) & \dots & L_{g_m} L_f^{r_m-1} h_m(x) \end{bmatrix} u_a \tag{7}$$

the Eq. (7) can be solved for u to obtain:

$$\tilde{u}_a = A(x)^{-1}.\left(\begin{bmatrix} y_1^{(r_1)} \\ \vdots \\ y_m^{(r_m)} \end{bmatrix} - \begin{bmatrix} L_f^{r_1} h_1(x) \\ \vdots \\ L_f^{r_m} h_m(x) \end{bmatrix}\right) \tag{8}$$

5.2. Local fault filter design for RCA

Considering the actuator subsystem model Eq. (3), by utilizing the reconstructed $\tilde{u}_a$, as well as analyzing the fault resources v_i, $i = 1, .., k$, we can recognize the root cause of the detected fault. To achieve this purpose, through adaptive diagnostic techniques proposed in [8], m banks of k observers corresponding for all possible faulty models are constructed and extended as below:

$$1 \le j \le m, 1 \le i \le k, t \ge t_f$$

$$\begin{cases} \dot{\hat{x}}_a^{i_j} = f_a^j\left(\hat{x}_a^{i_j}, u_j\right) + \sum\limits_{l \neq i} g_{al}^j\left(\hat{x}_a^{i_j}, u_j\right)\theta_l^j + g_{ai}^j\left(\hat{x}_a^{i_j}, u_j\right)\hat{v}_i^j + H_{i_j}\left(\tilde{u}_a^j - \hat{u}_a^{i_j}\right) \\ \hat{v}_i^j = 2\gamma_{i_j}\left(\tilde{u}_a^j - \hat{u}_a^{i_j}\right)^T P_{i_j} g_{ai}^j \\ \hat{u}_a^{i_j} = h_a^j\left(\hat{x}_a^{i_j}, u_j\right) \end{cases} \tag{9}$$

where j denotes jth actuator, i is ith observer corresponding to the ith fault resource candidate v_i. $\hat{x}_a^{i_j} \in \mathcal{R}^n$ is the estimated state vector of ith observer for jth actuator, $\hat{v}_i^j$ is the fault estimation of v_i of jth actuator, and $\hat{u}_a^{i_j}$ is the estimated output vector of the ith observer for jth actuator. $\tilde{u}_a^j$ is reconstructed output of jth actuator from y, u_j is the input of jth actuator. θ_l^j is the nominal value of parameters in jth actuator, subscript $l \neq i$. f_a^j, h_a^j, g_a^j are analytic functions of jth actuator. H_{i_j} is a Hurwitz matrix that can be chosen freely with a goal to increase as much as possible the dynamic of the observer, γ_{i_j} is a design constant and P_{i_j} is a positive definite matrix.

6. Application to a heat exchanger-control valve interconnected system

6.1. System modeling

Consider a counter heat exchanger subsystem can be written in a state-space form:

$$\begin{cases} \dot{x}_1 = G_1(x_1)x_2 + g_1(x_1, u) \\ \dot{x}_2 = \varepsilon(u, \dot{u}, x_a) \\ y = x_1 \end{cases} \tag{10}$$

where, $G_1(x_1) = \begin{pmatrix} \frac{(T_{pi} - x_{11})}{V_p} & 0 \\ 0 & \frac{(T_{ui} - x_{12})}{V_u} \end{pmatrix}$, and $f_1(x) = \begin{pmatrix} \frac{h_p A}{\rho_p C_{p_p} V_p}(x_{11} - x_{12}) \\ \frac{h_u A}{\rho_u C_{p_u} V_u}(x_{12} - x_{11}) \end{pmatrix}$.

where the state vector as $x_1{}^T = [x_{11}, x_{12}]^T = [T_p, T_u]^T$, the control input $x_2{}^T = u_a{}^T = [u_{a1}, u_{a2}]^T = [F_p, F_u]^T$, the output vector of measurable variables $y^T = [x_{11}, x_{12}]^T = [T_p, T_u]^T$, ρ_p, ρ_u are density of the process fluid and utility fluid (in $kg.m^{-3}$), V_p, V_u are volume of the process fluid and utility fluid (in m^3), C_{p_p}, C_{p_u} are specific heat of the process fluid and utility fluid (in $J.kg^{-1}.K^{-1}$), U is the overall heat transfer coefficient (in $J.m^{-2}.K^{-1}.s^{-1}$). A is the reaction area (in m^2). F_p, F_u are mass flowrate of process fluid and utility fluid (in $kg.s^{-1}$). T_p is the process fluid temperature of previous, the inlet temperature is T_{pi}. T_u is the utility fluid temperature, the inlet temperature of utility fluid T_{ui}.

Consider actuator subsystem is described by four states, two inputs and two outputs, as:

$$\begin{cases} \dot{x}_a = \begin{bmatrix} 0 & 1 & 0 & 0 \\ -\frac{k_1}{m} & -\frac{\mu_1}{m} & 0 & 0 \\ 0 & 0 & 0 & 1 \\ 0 & 0 & -\frac{k_2}{m} & -\frac{\mu_2}{m} \end{bmatrix} x_a + \begin{bmatrix} \frac{A_a}{m} & 0 \\ 0 & 0 \\ 0 & \frac{A_a}{m} \\ 0 & 0 \end{bmatrix} u \\ u_{a=} \begin{bmatrix} C_v\sqrt{\frac{\Delta P_1}{sg}} & 0 & C_v\sqrt{\frac{\Delta P_2}{sg}} & 0 \end{bmatrix} x_a \end{cases} \tag{11}$$

where $x_a{}^T = [x_{a1} \quad x_{a2} \quad x_{a3} \quad x_{a4}] = \left[X_1 \quad \frac{dX_1}{dt} \quad X_2 \quad \frac{dX_2}{dt}\right]$, $u^T = [u_1 \quad u_2] = [p_{c1} \quad p_{c2}]$, $u_a{}^T = [F_1 \quad F_2] = \left[C_v\sqrt{\frac{\Delta P_1}{sg}}X_1 \quad C_v\sqrt{\frac{\Delta P_2}{sg}}X_2\right]$, $C = [c_1 \quad c_2 \quad c_3 \quad c_4] = \left[C_v\sqrt{\frac{\Delta P_1}{sg}} \quad 0 \quad C_v\sqrt{\frac{\Delta P_2}{sg}} \quad 0\right]$, F is flow rate ($m^3s^{-1}$), ΔP is the fluid pressure drop across the valve (Pa), sg is specific gravity of fluid and equals 1 for pure water, X is the valve opening or valve "lift" (X = 1 for max flow), C_v is valve coefficient (given by manufacturer), f(X) is flow characteristic which is defined as the relationship between valve capacity and fluid travel through the valve. There are three flow characteristics to choose from: linear valve control; quick opening valve control; equal percentage valve control. For linear valve, $f(X) = X$, the valve opening is related to stem displacement, A_a is the diaphragm area on which the pneumatic pressure acts, p_c is the pneumatic pressure, m is the mass of the control valve stem, μ is the friction of the valve stem, k is the spring compliance, and X is the stem displacement or percentage opening of the valve.

Thus, $\varepsilon(u, \dot{u}, x_a)$ can be obtained by a function for the derivatives for u_a :

$$\dot{u}_a = \varepsilon(u, \dot{u}, x_a) = \frac{\partial h_a}{\partial u}(u, x_a)\dot{u} + \frac{\partial h_a}{\partial x_a}(u, x_a) f_a(u, x_a) \tag{12}$$

$$= \begin{pmatrix} C_v\sqrt{\frac{\Delta P_1}{sg}} & 0 & C_v\sqrt{\frac{\Delta P_2}{sg}} & 0 \end{pmatrix} x_a + \begin{pmatrix} \frac{A_a}{m} C_v\sqrt{\frac{\Delta P_1}{sg}} & \frac{A_a}{m} C_v\sqrt{\frac{\Delta P_2}{sg}} \end{pmatrix} u$$

Four kinds of fault influencing dynamics of the valve are considered in this work: (1) fault f1: valve clogging, occurs when the servomotor stem is blocked by an external event of a mechanical nature. It results in limitation of the piston movement in both direction, and therefore the flow cannot drop below a certain value; (2) fault f2: change of pressure drop across valve, results in $\Delta P + \Delta P'$; (3) fault f3: bellow-seal leakage due to leak, resulting in $p_c A_a + P$ changed; valve internal leakage is a common malfunction with industrial control valves. The causes of such leakage are numerous, including damaged plug or seat, insufficient seat load or reduced spring rate; (4) fault f4: control valve diaphragm perforation due to pinhole cracks in the periphery, resulting in k changed.

As above description shown, actuator fault may be caused by parameters μ, k, u, Δp, then there are eight related parameters in two actuators: $\begin{bmatrix} k_1 & \mu_1 & k_2 & \mu_2 & p_{c1} & p_{c2} & \Delta P_1 & \Delta P_2 \end{bmatrix}$. The process of RCA is to identify abnormal variations of these eight parameters. Two banks of RCA observers are generated, aim at generating two banks of four residuals for those abovementioned fault causes. One bank of residuals are $s_{11}, s_{12}, s_{13}, s_{14}$, aim at identifying fault causes f1, f2, f3, and f4 in actuator of process fluid, the other bank are $s_{21}, s_{22}, s_{23}, s_{24}$, aim at identifying fault causes f1, f2, f3, and f4 in actuator of utility fluid respectively. If any of these residuals exceeds its threshold, the fault is caused by the corresponding fault causes.

6.2. Numerical simulation results

The simulation results validate the proposed strategy. We first give the operating conditions of the simulation. The input of the inlet flow rate of the utility fluid F_u is $4.22e^{-5} m^3 s^{-1}$, and inlet flow rate of the process fluid F_p is $4.17e^{-6} m^3 s^{-1}$. Initial condition for observers supposed to be 0. Parameters in actuator subsystem are: $m = 2$ kg, $A_a = 0.029\ m^2$, $\mu = 1500\ Nsm^{-1}$ and $k = 6089\ Nm^{-1}$, P_c for utility fluid is 1 MP_a, 1.2 Mpa for process fluid, pressure drop ΔP in utility fluid is 0.6 MP_a and 60 KP_a in process fluid.

As above mentioned, for most part in practical situation, single fault is observed while multiple faults rarely occur on each actuator. Therefore, we consider each actuator is subject to only one fault, and then two faults may occur simultaneously in the actuator subsystem. Suppose the output measurement y is corrupted by a colored noise. The colored noise is generated with a second-order AR filter excited by a Gaussian white noise with zero mean and unitary variance. The standard deviation of the colored noise is about 3.5.

For actuator of process fluid, it is supposed to suffer leakage fault, and reasons that can lead to the leakage are as follows: valve tightness, leaky bushing, and terminals. Valve clogging fault

is supposed in actuator of utility fluid, it is a commonly encountered fault. If not properly repaired, this kind of fault may cause severe impacts on system performance. Simulation results are demonstrated in **Figures 5–8**.

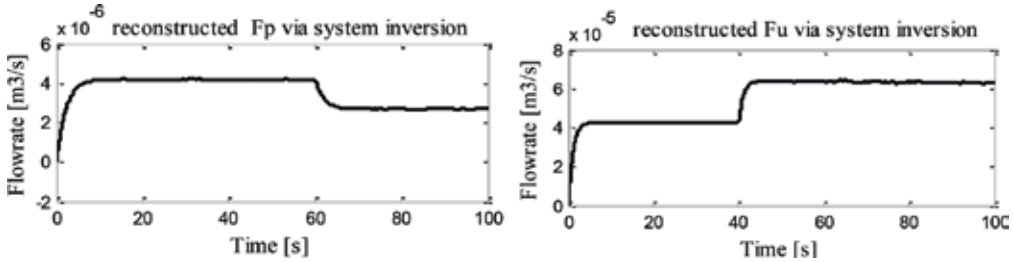

Figure 5. Reconstructed input $\tilde{F}_u$, $\tilde{F}_p$ from output Tp, Tu.

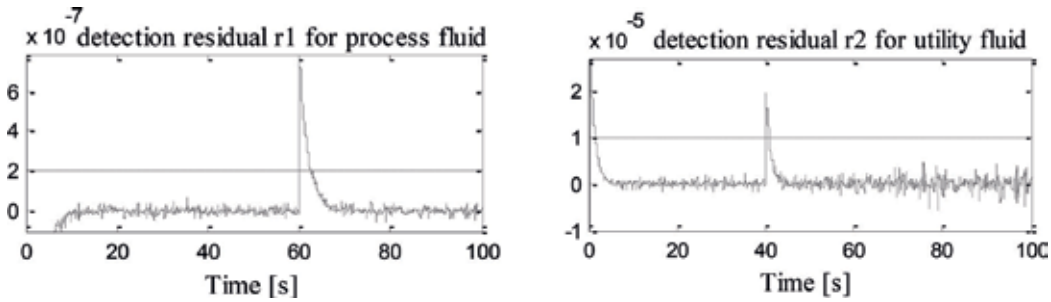

Figure 6. Detection residual.

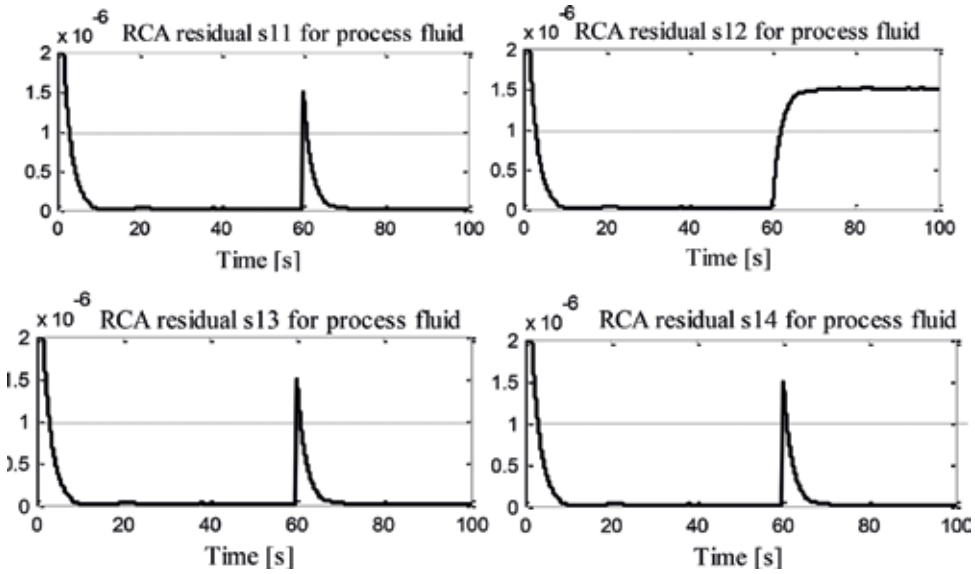

Figure 7. Residuals for identifying fault cause in process fluid.

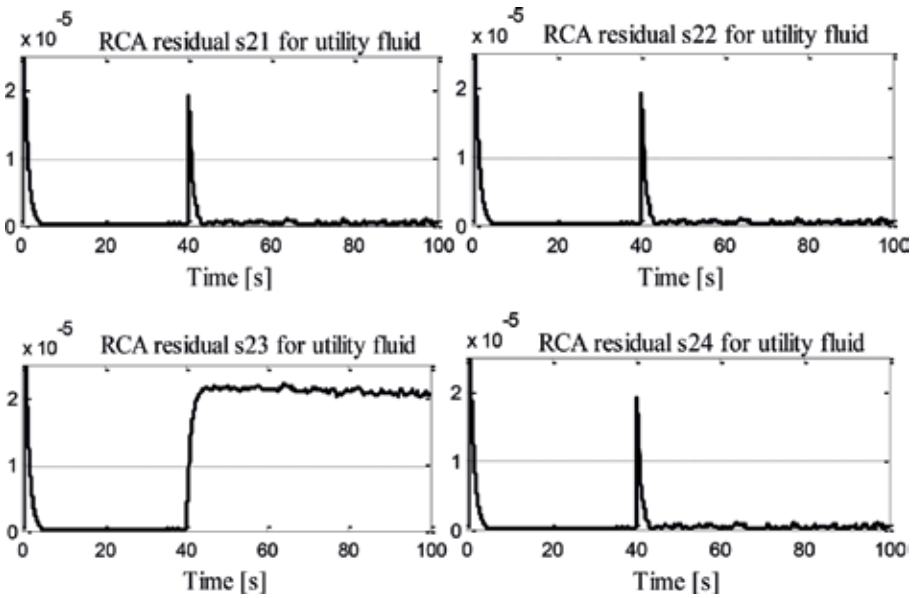

Figure 8. Residuals for identifying fault cause in utility fluid.

It can be seen from **Figure 5** that although noise exists, the developed input reconstruction techniques can provide reconstructed inputs with a good accuracy. At actuator of process fluid, sudden decrease occurs at 60 s which indicates occurrence of a fault, and it takes 4 s to steady at new value. For actuator of utility fluid, the reconstructed value increases from 40 s, and is stable after about 3 s. A fault is detected due to the unexpected increase.

As illustrated in **Figure 6**, detection residual r_1 indicates a fault in actuator of process fluid at 60 s, it takes 1.2 s to determine the occurrence of the fault. Detection residual r_2 refers to a fault in actuator of utility fluid at 40 s, and it takes 1.5 s to detect it. We can shorten the detection time and detect smaller fault by employing larger gain for the detection observers or adopt a smaller threshold. However, larger gain or larger threshold may fail to detect the fault correctly, since observer with larger gain is too sensitive to noise and smaller threshold may lead to be undistinguished from noise. Therefore, a trade between detectability and sensitivity should be made in order to detect the fault correctly. In summary, a small magnitude fault may not be detected within the existence of the noise. Again, after detection of the faults, we have to identify their root causes.

We can see from **Figure 7** that only RCA residual s_{12} breaks through its threshold and remains beyond it; the rest three RCA residuals are below their thresholds, and then the fault resource f2 of actuator of process fluid is identified. When comes to RCA residuals for actuator of utility fluid in **Figure 8**, only s_{23} is beyond its threshold which verifies the occurrence of fault cause f3.

From the above simulation results, we can see that the proposed strategy is available to detect and locate a fault correctly, and root cause analysis for each detected fault is achieved with a good accuracy. Encouraging simulation results are obtained thanks to the robustness.

7. Conclusions

We propose a left invertible interconnected nonlinear system structure with a dynamic inversion-based input estimation laws, forming a novel model-based multilevel-based actuator FDD algorithm. This algorithm provides a systematic solution to performance monitoring and actuator fault diagnosis for nonlinear dynamic system. The new system structure, together with the fault diagnosis algorithm design, is the first to emphasize the importance of root cause analysis of field devices fault, as well as the influences of local internal dynamic on the global dynamics. The developed multilevel model-based fault diagnosis algorithm is then a first effort to combine the strength of the system level and the component level model-based fault diagnosis.

Acknowledgements

This work was supported by Science and Technology Foundation of Guizhou Province, China ([2016]1053).

Conflict of interest

The authors declare that there is no conflict of interest regarding the publication of this paper.

Author details

Mei Zhang[1,2,4]*, Ze-tao Li[1], Boutaib Dahhou[3,4] and Michel Cabassud[2,4]

*Address all correspondence to: gzulzt@163.com

1 Electrical Engineering College, Guizhou University, Guiyang, China

2 CNRS, LGC, Toulouse, France

3 CNRS, LAAS, Toulouse, France

4 Univ de Toulouse, UPS, Toulouse, France

References

[1] Bartyś M, Patton R, Syfert M, de las Heras S, Quevedo J. Introduction to the DAMADICS actuator FDI benchmark study. Control Engineering Practice. 2006;**14**:577-596

[2] Puig V, Stancu a, Escobet T, Nejjari F, Quevedo J, Patton RJ. Passive robust fault detection using interval observers: Application to the DAMADICS benchmark problem. Control Engineering Practice. 2006;**14**:621-633

[3] Roy K, Banavar RN, Thangasamy S. Application of fault detection and identification (FDI) techniquesin power regulating systems of nuclear reactors. IEEE Transactions on Nuclear Science. 1998;**45**(6):3184-3201

[4] Zhang K. Fault Detection and Diagnosis for a Multi-actuator Pneumatic System. Stony Brook University; 2011

[5] Zhao K. An Integrated Approach to Performance Monitoring and Fault Diagnosis of Nuclear Power Systems. Knoxville: University of Tennessee; 2005

[6] Venkatasubramanian V, Rengaswamy R, Yin K. A review of process fault detection and diagnosis Part I: Quantitative Model-Based Methods. Computer and Chemical Engineering. 2003;**27**:293-311

[7] Zhang Q. A new residual generation and evaluation method for detection and isolation of faults in non-linear systems. International Journal of Adaptive Control Signal Processing. 2000;**14**:759-773

[8] Fragkoulis D, Roux G, Dahhou B. Detection, isolation and identification of multiple actuator and sensor faults in nonlinear dynamic systems: Application to a waste water treatment process. Applied Mathematical Modelling. 2011;**35**(1):522-543

[9] Jiang B, Chowdhury FN. Parameter fault detection and estimation of a class of nonlinear systems using observers. Journal of the Franklin Institute. 2005;**342**:725-736

[10] Yan X-G, Edwards C. Nonlinear robust fault reconstruction and estimation using a sliding mode observer. Automatica. 2007;**43**:1605-1614

[11] Vijay P, Tade MO, Ahmed K, Utikar R, Pareek V. Simultaneous estimation of states and inputs in a planar solid oxide fuel cell using nonlinear adaptive observer design. Journal of Power Sources. 2014;**248**:1218-1233

[12] Zhou Y, Liu J, Dexter AL. Estimation of an incipient fault using an adaptive neurofuzzy sliding-mode observer. Energy and Buildings. 2014;**77**:256-269

[13] Mekki H, Benzineb O, Boukhetala D, Tadjine M, Benbouzid M. Sliding mode based fault detection, reconstruction and fault tolerant control scheme for motor systems. ISA Transactions. 2015;**2**:1-12

[14] Bokor J, Szabó Z. Fault detection and isolation in nonlinear systems. Annual Reviews in Control. 2009;**33**:113-123

[15] Blesa J, Rotondo D, Puig V, Nejjari F. FDI and FTC of wind turbines using the interval observer approach and virtual actuators/sensors. Control Engineering Practice. 2014;**24**: 138-155

[16] Schubert U, Kruger U, Wozny G, Arellano-Garcia H. Input reconstruction for statistical-based fault detection and isolation. AICHE Journal. 2012;**58**:1513-1523

[17] Szigeti F, Bokor J, Edelmayer A. Input reconstruction by means of system inversion: Application to fault detection and isolation. In: 15th Triennial World Congress; 2002

[18] Edwards C, Spurgeon SK, Patton RJ. Sliding mode observers for fault detection and isolation. Automatica. 2000;**36**:541-553

[19] Veluvolu KC, Defoort M, Soh YC. High-gain observer with sliding mode for nonlinear state estimation and fault reconstruction. Journal of the Franklin Institute. 2014;**351**(4): 1995-2014

[20] Di Miceli Raimondi N, Olivier-Maget N, Gabas N, Cabassud M, Gourdon C. Safety enhancement by transposition of the nitration of toluene from semi-batch reactor to continuous intensified heat exchanger reactor. Chemical Engineering Research and Design. 2015; **94**:182-193

[21] Manninen T. Fault Simulator and Detection for a Process Control Valve. Aalto University; 2012

[22] Rahmat MF, Sunar NH, Salim SNS, Abidin MSZ, Fauzi a a M, Ismail ZH. Review on Modeling and controller design. International Journal of Smart Sensing and Intelligent Systems. 2011;**4**(4):630-661

[23] Yang JC, Clarke DW. The self-validating actuator. Control Engineering Practice. 1999;**7**: 249-260

[24] Shen Z, Wang Q. A novel health evaluation strategy for multifunctional self-validating sensors. Sensors (Switzerland). 2013;**13**(January 2013):587-610

[25] Sarosi J, Biro I, Nemeth J, Cveticanin L. Dynamic modeling of a pneumatic muscle actuator with two-direction motion. Mechanism and Machine Theory. 2015;**85**:25-34

[26] Jin J, Shi J. Automatic feature extraction of waveform signals for in-process diagnostic performance improvement. Journal of Intelligent Manufacturing. 2001;**12**:257-268

[27] Sun Q. Singularityanalysis using continuous wavelet transform for bearing fault diagnosis. Mechanical Systems and Signal Processing. 2002;**16**:1025-1041

[28] Naseradinmousavi P, Nataraj C. Nonlinear mathematical modeling of butterfly valves driven by solenoid actuators. Applied Mathematical Modelling. 2011;**35**(5):2324-2335

[29] Mehmood A, Laghrouche S, El Bagdouri M. Modeling identification and simulation of pneumatic actuator for VGT system. Sensors and Actuators A: Physical. 2011;**165**(2):367-378

[30] Richer E, Hurmuzulu Y. A high performance pneumatic force actuator system part 1—Nonlinear mathematical model. ASME Journal of Dynamic Systems, Measurement, and Control. 2001;**122**(3):416-425

[31] Kayihan A. Friction compensation for a process control valve. Control Engineering Practice. 2000;**8**:799-812

[32] Hafaifa A, Djeddi AZ. Fault detection and isolation in industrial control valve based on artificial neural networks diagnosis. Control Engineering and Applied Informatics. 2013; **15**(3):61-69

[33] Subbaraj P, Kannapiran B. Fault detection and diagnosis of pneumatic valve using adaptive Neuro-fuzzy inference system approach. Applied Soft Computing Journal. 2014;**19**: 362-371

[34] Maksimov V, Pandolfi L. Dynamical reconstruction of unknown inputs in nonlinear differential equations. Applied Mathematics Letters. 2001;**14**:725-730

[35] Edelmayer A, Bokor J, Szabo Z, Szigeti F. Input reconstruction by means of system inversion: A geometric approach to fault detection and isolation in nonlinear systems. International Journal of Applied Mathematics and Computer Science. 2004;**14**(2):189-199

[36] Tanwani A, Liberzon D. Invertibility of switched nonlinear systems. Automatica. 2010; **46**(12):1962-1973

[37] Isidori A. Nonlinear Control Systems. 3rd ed. Berlin: Springer; 1995

Edited by Constantin Volosencu

The book promotes new research results in the field of modern actuators and their applications. New coverage of dielectric barrier discharge plasma actuators, polymeric microgripper based on the cascaded V-shaped electrothermal actuators, ionic polymer actuators, wideband actuators and energy harvesters, electromagnetic actuators and shape memory alloy actuators are comprehended. The book is structured in four sections: design, fabrication and simulation; control systems; medical applications and fault detection. Seven chapters are published following a rigorous selection process. In the first section, a study carried out to investigate experimentally and by numerical simulations a microscale plasma actuator; the design, fabrication, numerical simulations, and experimental investigations of a polymeric microgripper designed using the cascaded V-shaped electrothermal actuators; a review of the development of ionic polymer actuator with introduction of two kinds of typical polymer actuators—ionic polymer-metal composites and bucky gel actuator—with their basic principle and fabrication process and typical applications and a methodology of designing and testing wideband actuators and energy harvesters, treated as one mechanical resonator, with a discussion on shock harvester, resonant harvester and energy transmission system, are presented. The second section has a chapter dedicated to modeling, system identification and control of electromagnetic actuators with main focus on the actuators used in magnetic levitation, in fuel injection systems and in variable valve timing. The third section presents a study focused on quantifying the decline in tactile sensation associated with diabetic neuropathy and developed a measurement device that used a thin-shaped memory alloy wire as the actuator. The fourth section includes a chapter presenting a two-level fault diagnosis and root-cause analysis scheme for a class of interconnected invertible dynamic systems, which aims at detecting and identifying actuator fault and causes.

Published in London, UK

IntechOpen

ISBN 978-1-83881-583-7
9 781838 815837